Gas-Sensing Properties of V_2O_5-Nanofibers and Carbon Nanotubes

THÈSE No 3104 (2004)
présentée à la Faculté Science de Base
Institut de Physique des Nanostructures
Section de Physique
ÉCOLE POLYTECHNIQUE FÉDÉRALE DE LAUSANNE

pour l'obtention du grade de Docteur ès sciences
par
ULRICH SCHLECHT
Masters of Science in Physics, University of Kentucky, Etats-Unis
et de nationalité allemande

acceptée sur proposition du jury:
Prof. K. Kern, directeur de thèse
Prof. L. Forro, rapporteur
Prof. L. Schlapbach, rapporteur
Prof. F. Netzer, rapporteur

Lausanne, EPFL

2004

Abstract

In this thesis, the synthesis and characterization of V_2O_5-nanostructures, as well as the gas sensing properties of V_2O_5-nanofibers and carbon nanotubes have been investigated. Various modifications of the nanowires have been successfully employed in order to achieve an improved sensitivity and selectivity of the sensors to specific analytes.

The V_2O_5-nanofibers have been synthesized via solution-based chemistry. Two modifications of the standard synthesis route have been attempted in order to reduce the time required to grow fibers of sufficient length. The first modification utilizes silver ions, which allowed for a ten-fold increase in growth speed. In order to determine the role of the silver in the synthesis, energy-dispersive X-ray (EDX) analysis has been performed, which revealed the presence of silver-clusters attached to the V_2O_5-nanofibers, as well as silver incorporated into the fibers. The second modification is based on hydrothermal synthesis performed at 180°C, which yielded VO_x-nanobelts rather than V_2O_5-nanofibers. Most striking is their appearance in the shape of a boomerang with a reproducible angle of 96°. The origin of the kinked structure, as determined with transmission electron microscopy (TEM) and selected area electron diffraction (SAED), was found to be twinning of the crystalline material along the [130]-direction.

Raman spectroscopy and temperature-dependent electrical transport measurements on the V_2O_5-materials revealed their close similarity. In all cases, the electrical transport was found to be dominated by a hopping-like conduction.

To assess the gas sensing properties of V_2O_5-nanofibers and carbon nanotubes, network samples have been investigated at room temperature, using the change of resistance as sensor signal.

For the detection of ammonia with the V_2O_5-nanofibers, the change of resistance has been ascribed to charge transfer. Through evaporation of gold onto the V_2O_5-nanofibers the sensor response could be improved by a factor of seven. The slower desorption of ammonia from the gold-modified fibers, as compared to the unmodified material, is attributed to a stronger binding of ammonia to gold.

The detection of butylamine with V_2O_5-nanofibers has been studied due to the application relevance, as this compound is produced in rotten food. By investigating different contact configurations, the sensor response (∼500 %) has been found to originate from intercalation of the analyte between electrode and fiber, resulting in an increased contact resistance.

Modifying networks of V_2O_5-nanofibers via deposition of an ultrathin layer of palladium rendered the sensors highly sensitive to hydrogen, resulting in responses of more than 100,000 %. The sensor mechanism, as elucidated through a combined study using Raman spectroscopy and temperature-dependent electrical transport measurements, involved atomic hydrogen, formed within the palladium layer. Its reaction with oxygen ions in the V_2O_5-lattice leads to oxygen deficiencies and hence the formation of additional polarons, which combine to less mobile bipolarons, as apparent from an increase in the hopping activation energy.

Besides V_2O_5-nanofibers, the sensor properties of carbon nanotubes have been studied. Their gas sensing behavior has been interpreted in terms of charge transfer between the analyte molecules and the p-type semiconducting nanotubes present in network samples. In the specific case of ammonia exposure, the nanotube sensors do not recover completely to their original resistance, but equilibrate at an increased value. This observation has been accounted for by an adapted Langmuir isotherm, which assumes reversible and irreversible adsorption sites on the nanotube surface. The presence of irreversible sites, which require temperatures up to 500 K for the desorption of ammonia, could be experimentally confirmed by thermal desorption spectroscopy (TDS).

To render carbon nanotubes sensitive to hydrogen, palladium nanoparticles were electrodeposited. This method offers the advantage of restricting the modification to nanotubes which are contacted to the electrodes, while isolated nanotubes and substrate are not affected. Palladium-modified nanotubes prepared in this fashion showed good responses to hydrogen at room temperature.

Résumé

Ce travail de thèse porte sur la synthèse et la caractéristation de nanostructures de V_2O_5 et sur les propriétés de nanofibres de V_2O_5 et de nanotubes de carbone comme capteurs de gaz. Des modifications de ces nanofils ont permis d'augmenter leur sélectivité et leur sensibilité à des composés spécifiques.

Les nanofibres de V_2O_5 ont été synthétisées par voie chimique en solution. Deux modifications du protocole standard de synthèse ont été testées afin de réduire le temps nécessaire à la croissance de fibres de longueur suffisante.

La première utilise des ions argent et permet d'augmenter la vitesse de croissance d'un facteur dix. Afin de déterminer le rôle de l'argent dans la synthèse, des analyses par rayons X dispersifs en énergie (EDX) ont été réalisées et ont permis de mettre en évidence la présence d'agrégats d'argent attachés aux nanofibres de V_2O_5 ainsi que l'incorporation d'argent dans les fibres.

La seconde modification est basée sur une synthèse hydrothermique à 180°C et permet d'obtenir des nano-ceintures de VO_x plutôt que des nanofibres de V_2O_5. Le plus frappant est leur apparence en forme de boomerang avec un angle reproductible de 96°. Des études par microscopie électronique en transmission (TEM) et par diffraction d'électrons selectionnée en aire (SAED) ont permis de montrer que l'origine de cette structure coudée est le maclage du matériau cristallin suivant la direction [130].

La spectroscopie Raman et des mesures de transport électrique en fonction de la température ont permis de mettre en évidence le caractère similaire des propriétés de transport des matériaux en V_2O_5. Dans tous les cas, les propriétés sont dominées par une conductance par sauts.

Tout au long de cette thèse, les propriétés de capteur de gaz des nanofils ont été explorées à température ambiante en utilisant les changements de résistance comme signal.

Dans le cas de nanofibres de V_2O_5 interagissant avec l'ammoniac, la variation de résistance a été attribuée à un transfert de charge. La réponse du capteur a pu être augmentée d'un facteur sept par évaporation d'or sur les nanofibres de V_2O_5. Le fait que l'ammoniac désorbe plus lentement du capteur modifié par l'or que du capteur non modifié a été attribué à la formation de liaison plus forte entre l'ammoniac et l'or.

La détection du butylamine par des nanofibres de V_2O_5 a été étudiée à cause de son caractère pertinent en vue d'applications potentielles, le butylamine étant un produit de décomposition des aliments pourris. En étudiant plusieurs configurations pour le contact, il a pu être déterminé que la réponse des capteurs ($\sim$500 %) provient de l'intercalage du composé à détecter entre l'électrode et la fibre, d'où une résistance de contact plus élevée.

La modification d'un réseau de nanofibres de V_2O_5 par dépôt d'une couche ultramince de palladium rend le capteur très sensible à l'hydrogène avec des réponses supérieures à 100 000%. Une étude combinée par spectroscopie Raman et mesure de transport électrique en fonction de la température montre que le mécanisme du capteur met en jeu de l'hydrogène atomique. L'hydrogène atomique formé au sein du palladium, réagit avec les ions oxygène du réseau de V_2O_5 pour former de l'eau. Les lacunes résultantes conduisent à la formation de polarons additionnels qui se combinent avec les bipolarons moins mobiles, comme le prouve l'augmentation observée de l'énergie d'activation de saut.

Outre le cas des nanofibres de V_2O_5, les propriétés de capteur de gaz de nanotubes de carbone ont également été étudiées. Leur comportement a été interprété en terme de transfert de charge entre les molécules à détecter et les nanotubes semi-conducteurs de type p présents dans l'échantillon. Dans le cas spécifique de l'ammoniac, le capteur ne retrouve pas sa résistance originelle. Sa résistance s'équilibre à une valeur plus élevée. Ce comportement peut être décrit par une isotherme de Langmuir modifiée en prenant en compte des sites d'adsorption réversible et irréversible à la surface des nanotubes. La présence de sites d'adsorption irréversible, pour lesquels la température de désorption monte jusqu'à 500K, a pu être confirmée par spectroscopie de désorption thermique (TDS).

Des nanoparticules de palladium ont été électro-déposées sur des nanotubes de carbone, afin de les rendre sensible à l'hydrogène. Cette méthode offre l'avantange que seuls les nanotubes qui sont connectés aux électrodes sont modifiés, alors que les nanotubes isolés et le substrat ne sont pas affectés. Ces nanotubes modifiés par le palladium montrent une bonne réponse à l'hydrogène à température ambiante.

Zusammenfassung

Die vorliegende Doktorarbeit befasst sich mit der Synthese und Charakterisierung von V_2O_5-Nanostrukturen, sowie den Eigenschaften von V_2O_5-Nanofasern und Kohlenstoff-Nanoröhren als Gassensoren. Eine Modifizierung der Nanodrähte wurde erfolgreich eingesetzt, um eine erhöhte Sensitivität und Selektivität der Sensoren gegenüber spezifischen Gasen zu erreichen.

V_2O_5-Nanofasern wurden auf der Basis von Nasschemie synthetisiert. Zwei Modifikationen der Standardsynthese wurden erprobt, um die Zeit zu reduzieren, die benötigt wird um Fasern mit ausreichender Länge herzustellen.

Die erste Modifikation benutzt Silberionen, was zu einer Verzehnfachung der Wachstumsgeschwindigkeit führt. Um die Rolle des Silbers bei der Synthese zu bestimmen, wurde eine energiedispersive Röntgenanalyse (EDX) durchgeführt, wodurch die Anwesenheit von Silberpartikeln an den V_2O_5-Nanofasern, sowie Silber eingebettet in die Fasern, nachgewiesen werden konnte.

Die zweite Modifikation basiert auf der hydrothermalen Synthese bei 180°C, welche zur Bildung von VO_x-Nanobändern statt V_2O_5-Nanodrähten führte. Besonders bemerkenswert ist ihr Auftreten in Form eines Bumerangs mit einem reproduzierbaren Winkel von 96°. Der Ursprung der abknickenden Struktur konnte der Bildung von Zwillingung entlang der [130]-Richtung zugeschrieben werden, wie mit Transmissions-Elektronen Mikroskopie (TEM) und Feinbereichsbeugung (SAED) gezeigt werden konnte.

Ramanspektroskopie und temperaturabhängige, elektrische Transportmessungen an den V_2O_5-Materialien zeigten ihre grosse Ähnlichkeit zueinander. In allen Fällen werden die Transporteigenschaften von einem hopping-Mechanismus dominiert.

In der ganzen Doktorarbeit wurden die Eigenschaften zur Gassensorik an Netzwerken von Nanodrähten bei Raumtemperatur untersucht, wobei die Änderung des Widerstandes als Sensorsignal genutzt wurde.

Für die V_2O_5-Nanofasern wechselwirkend mit Ammoniak, wurde die Änderung des Widerstandes einem Ladungstransfer zugeschrieben. Durch die Bedampfung mit Gold auf die V_2O_5-Nanofasern konnte das Sensorsignal um den Faktor sieben verbessert werden. Im Vergleich zum unmodifizierten Sensor war die Desorption des mit Gold modifizierten Sensors langsamer, was einer stärkeren Wechselwirkung von Ammoniak mit Gold zuzuschreiben ist.

Die Detektierung von Butylamin wurde untersucht aufgrund seiner Anwendungsrelevanz, da Butylamin in verdorbenem Essen vorkommt. Durch die Untersuchung verschiedener Kontaktierungskonfigurationen konnte der Ursprung des Sensorsignals (∼500 %) bestimmt werden. Er beruht auf die Interkalation des Analyten zwischen Elektrode und Faser, was zu einem erhöhten Kontaktwiderstand führt.

Die Modifizierung eines Netzwerkes von V_2O_5-Nanofasern mittels der Deposition eines ultradünnen Films von Palladium, machte den Sensor hochgradig sensitiv zu Wasserstoff mit Signalen von über 100.000 %. Der Sensormechanismus wurde mit Ramanspektroskopie und temperaturabhängiger, elektrischer Transportmessungen analysiert und beinhaltet atomaren Wasserstoff. Der atomare Wasserstoff, erzeugt im Palladium, reagiert mit den Sauerstoffionen des V_2O_5-Gitters zu Wasser. Das resultierende Sauerstoffdefizit führt zur Bildung weiterer Polaronen, die zu wenig mobilen Bipolaronen kombinieren, wie mit einer Erhöhung der Aktivierungsenergie nachgewiesen werden konnte.

Neben V_2O_5-Nanofasern wurden auch die Sensoreigenschaften von Kohlenstoff Nanoröhren untersucht. Ihre Eigenschaften als Gassensoren wurden interpretiert in Form eines Ladungstransfers zwischen den Gasmolekülen und den p-dotierten halbleitenden Nanoröhren, wie sie in Netzwerkproben vorhanden sind. Im speziellen Fall der Exposition von Ammoniak, erholen sich die Sensoren nicht komplett zu ihrem ursprünglichen Widerstand, sondern erreichen bei einem erhöhten Wert ihr Gleichgewicht. Dieses Verhalten wurde mit einer adaptierten Langmuir-Theorie Rechnung getragen, welche reversible und irreversible Adsorptionsplätze auf der Nanoröhrenoberfläche annimmt. Die Anwesenheit von irreversiblen Stellen, welche Temperaturen von bis zu 500 K für die Desorption benötigen, konnte mit thermaler Desorptionsspektroskopie (TDS) bestätigt werden.

Um Kohlenstoff Nanoröhren sensitiv zu Wasserstoff zu machen, wurden mittels Elektrochemie Nanopartikel aus Palladium abgeschieden. Diese Methode besitzt den Vorteil, dass ausschließlich Nanoröhren modifiziert werden, die über Elektroden kontaktiert sind, während isolierte Nanoröhren und das Substrat nicht beeinträchtigt werden. Die mit Palladium modifizierten Nanoröhren zeigen ein gutes Sensorsignal gegenüber Wasserstoff bei Raumtemperatur.

Contents

Chapter 1

Introduction

Chemical and biological sensors have a profound impact in the areas of personal safety, public security, medical diagnosis, detection of environmental toxins, semiconductor processing, agriculture, as well as the automotive and aerospace industries [1–5]. The past few decades have seen the development of a multitude of simple, robust, solid-state sensors. Their operation is based on the binding of an analyte at the active surface of the sensor to result in a measurable signal.

The evolution of gas sensors closely parallels developments in microelectronics in that the architecture of sensing elements is influenced by design trends in planar electronics. A major goal of the field is to design sensors on a nanometer-scale that could be easily integrated with modern electronic fabrication technologies. Large arrays of macroscopic individual gas sensors used for many years for multicomponent analysis, each having its associated electrodes, filters, heating elements, and temperature detection, should be replaced by an "electronic nose" embodied in a single device that integrates the sensing and signal processing functions in one chip [6–9]. Multicomponent gas analysis with these devices is accomplished by pattern recognition analogous to odor identification by highly evolved organisms [10–12]. By increasing the number of sensing elements, as well as the power of the pattern recognition algorithms, one can envision a versatile device that can detect minute quantities (ultimately a single molecule) of various substances against a complex and changing background. These substances include explosive, biohazardous, toxic, or environmentally sensitive species. However, this task requires an increase in the sensitivity and selectivity of the sensor elements despite the reduction of active area, as the individual components should be miniaturized. Furthermore, as mobile gas sensors are desired, future applications require low power consumption. Therefore heating of the sensors to elevated temperatures is not possible.

In general, gas sensors have to fulfill specific requirements for technical applications, summarized as the four "s"-criteria: sensitivity, selectivity, stability, and speed [13]. Additional requirements are: easy fabrication, simple operation, and reversible response [4]. While these requirements are common to all types of gas sensors, special features have to be addressed for the various application fields, as mentioned above. These features might be exemplified by the case of hydrogen sensors.

The search for effective hydrogen sensors has boomed in recent years, as hydrogen is considered a future energy carrier replacing fossil fuel energy sources [14]. The fabrication of hydrogen fuel cells requires three types of sensors for monitoring the performance of these cells: (i) leak detection sensors, specified for low concentrations, (ii) alarm sensors for detection of hydrogen below the explosive limit of 4 % in air, and (iii) feed stock sensors to detect the hydrogen content within the storage container [14]. The diversity of applications for hydrogen sensors is reflected in a multitude of techniques involved in detection of the gas. These techniques are based on resistive elements [15–19], circuits with Schottky barriers [20], MOSFET devices [21–25], microcantilevers [26], and optical devices [27–29]. A review of hydrogen sensing techniques can be found in Reference [30].

Resistive sensors

In the following, the focus will be on resistive sensors, as the measurement of changes in conductance is in principle compatible to microelectronic devices, including signal processing. The fundamental aspects of resistive gas sensors can be divided into two subfields, the first of which deals with the interaction of gases with the sensor material, while the second describes the change of resistance due to the adsorbed gas.

A strong coupling of the analyte to the sensor material is desired, to yield good sensor responses. For biological species, key-lock interactions are frequently used for high selectivity in the detection of a specific biomolecule. However, the adsorption of the analyte to the sensor surface is irreversible, making such sensors a disposable device.

In general, a reversible adsorption of the gas at the sensor surface is desired. In certain situations, e.g. when detecting reactive gases, desorption can be assured by the operation of the sensor device at elevated temperature [31, 32], or the use of UV-illumination [33], as was shown for sensors based on carbon nanotubes, when detecting NO_2.

The second aspect involved in the resistive detection of gases is the change of resistance itself. As the electrical conductivity is defined as the product of charge carrier density and mobility ($\sigma = e \cdot n \cdot \mu$), changes in resistance can only be observed, if the gas alters either one of these material properties.

The variation of charge carrier density n is commonly known as doping and has been frequently utilized for the detection of gases. In order to obtain easily detectable changes, a small intrinsic charge carrier density is favorable, which suggests the use of semiconductors as sensor material. Special interest has been put on the use of metal-oxide sensors [34–37]. When detecting NO, the increase in resistance has been attributed to the typical n-type semiconducting behavior of many oxides, combined with the property of NO to withdraw electrons.

Furthermore, metal-oxide sensors have the ability to participate in catalytic reactions, which are utilized for the sensing mechanism (e.g. $MO_x + NO \rightarrow MO_{x-1} + NO_2$). These reactions do not only provide a strong interaction of the analyte with the sensor material, but in addition, the removal of lattice-oxygen leads to the creation of defects, which is reflected in a reduced mobility μ of the metal-oxide. Such defects are subsequently repaired in the presence of oxygen, restoring the sensors original resistance.

Sensors made from low-dimensional materials

Resistive sensors based on thick films operated at room temperature show negligible sensitivity to gases, as only the surface atoms are affected by the presence of certain analytes, such that the bulk conductivity remains unchanged. To overcome this problem, these sensors are heated to temperatures exceeding 250°C to enable the diffusion of gases into the bulk of the film, resulting in a measurable resistance change [4].

A natural alternative solution is the use of thin films, i.e. to reduce the dimension of the sensor device to two, thereby increasing the amount of surface atoms. Most prominent is the use of thin metal-oxide films for the detection of NO_x [34–36]. Despite their increased surface/volume ratio, the sensors have to be operated at 200–400°C to achieve responses exceeding 100 %.

Recent advances in the synthesis of nanotubes and nanofibers have allowed to reduce the sensor dimensions to one, resulting in a further increase of the surface/volume ratio. For example, titania-nanotubes [38], Pd/nanotube composites [39], and palladium mesowires [40, 41] have been used for the detection of hydrogen. Moreover, silver mesowires [42] and indiumoxide nanowires [43,44] have been used for detecting ammonia, while SnO_2-nanoribbons are capable of detecting NO_2 [37], CO, and ethanol [45]. Moreover, chemically modified Si-nanowires can be utilized as pH-sensors or bio-sensors [46].

The most prominent type of nanowires for use in sensors are carbon nanotubes [32, 33,39,47–49]. Their extraordinary electrical transport properties and the fact that every atom of the nanotube is a surface atom make them highly suited as gas sensors. Various physical properties have been exploited for sensor applications, such as impedance [50, 51], thermoelectricity [52], and ionization potentials of the gases utilizing nanotubes as

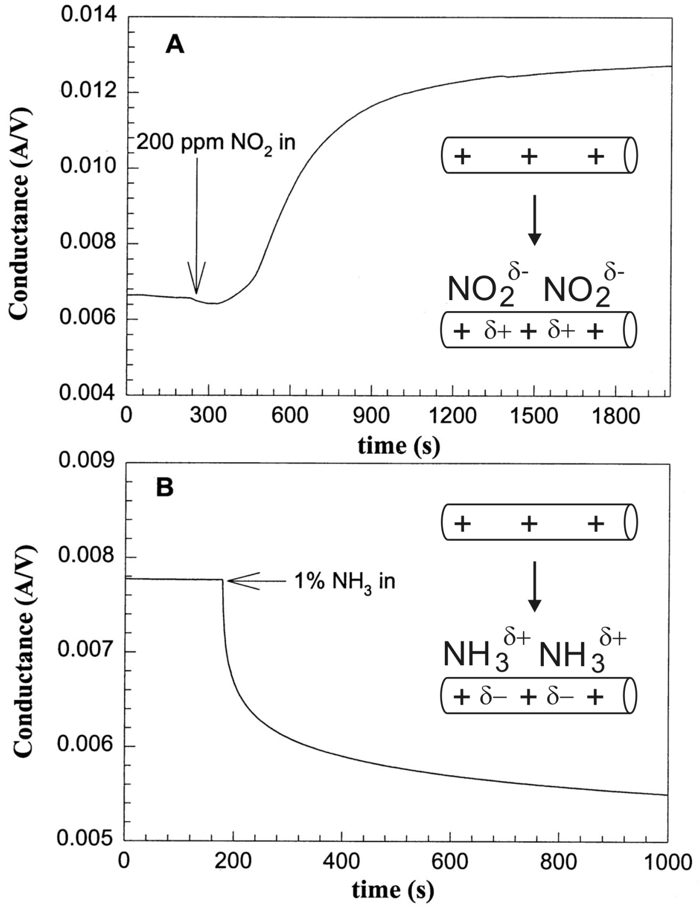

Figure 1.1: Change of conductance of carbon nanotube networks when exposed to (A) NO_2 and (B) NH_3 [47]. The effect of doping, assuming a p-type semiconducting nanotube, is illustrated in the insets.

field emitters [53]. In most cases, however, the change of resistance of the nanotubes has been used as sensor signal. Pioneering measurements on individual semiconducting nanotubes and networks have been performed by Kong et al. [47] for the detection of NO_2 and NH_3. The responses of carbon nanotube networks obtained in their work are reproduced in Figure 1.1. The conductance change has been explained by charge transfer between gas molecules and nanotubes, which alters the charge carrier density, as schematically illustrated in the insets of Figure 1.1. This interpretation is supported by the semiconducting behavior of the nanotubes (p-type for pristine material) together with the electron-donating/-accepting property of the analytes. The p-type character of the semiconducting nanotubes originates from the presence of oxygen on pristine nanotubes, while degassed samples show n-type behavior [48, 54].

Via chemical modification, the sensitivity and selectivity of carbon nanotubes can be enhanced. Evaporation of palladium onto the nanotubes, for instance, renders them

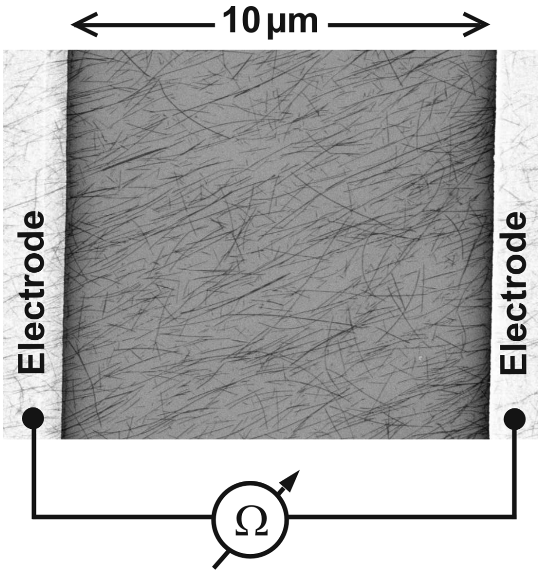

Figure 1.2: Network of V_2O_5-nanofibers deposited onto interdigitated electrodes [59].

sensitive to hydrogen [39]. In addtion, through coating with polymethylmethacrylate (PMMA), polyethyleneimine, or nafion, the tubes become sensitive to amines, NO_2, and NH_3, respectively, while the cross-sensitivity is reduced [49, 55]. Chemical functionalization with amine-terminated oligonucleotide probes makes carbon nanotubes sensitive to DNA [56].

It should be noted that sensors have also been built from zero-dimensional objects. Multilayers of the nanoparticles surface-stabilized by organic-shells [57, 58] show a resistance increase upon analyte intercalation in the organic matrix, as a consequence of the increased tunnelling distance between the nanoparticles.

Goals and structure of the thesis

Throughout this thesis, resistive measurements have been performed on nanowires for the detection of gases. Figure 1.2 exemplifies a typical device. The sensor-signal is expressed as change of resistance normalized to the initial resistance ($\Delta R/R_{ini}$). The normalization of the response with the initial resistance has been introduced to account for different coverages of the electrodes with the sensor material. Normalization with R_{ini} therefore results in a response per unit-length. All sensor experiments have been performed at room temperature, to ensure a low power consumption.

Networks of nanowires have been studied, since these show several advantages compared to sensors made of individual nanowires: Firstly, their ease of fabrication is a

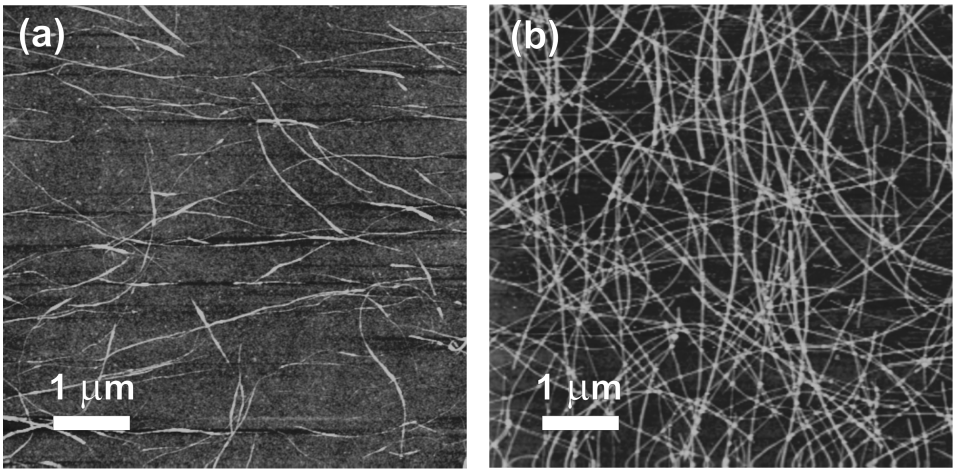

Figure 1.3: AFM-images of (a) carbon nanotubes and (b) V_2O_5-nanofibers

pre-requisite for technical applications. Secondly, the relative contribution of the contact resistance can be minimized, yielding a better signal-to-noise ratio.

Two types of nanowires have been used as components of gas sensors in this thesis: single-wall carbon nanotubes with diameters on the order of 1 nm, and V_2O_5-nanofibers with a rectangular cross-section (1.5×10 nm^2), as displayed in Figure 1.3. Carbon nanotubes have been chosen as a system on the nanometer scale, where the gas-sensing properties are dominated by doping-effects. By contrast, V_2O_5-nanofibers represent nanowires based on a metal-oxide. Special modifications have been performed with the aim of increasing sensitivity and selectivity of the sensors.

The first 1D-material used in this thesis are V_2O_5-nanofibers. These fibers have been investigated in detail due to their possible application in electrochemical devices [60], antistatic coatings [61], and lithium ion batteries [62]. However, the gas sensing properties of V_2O_5-nanofibers remained largely unexplored until present. In contrast to carbon nanotubes, which are normally synthesized via pulsed laser vaporization [63] or chemical vapor deposition [64], V_2O_5-nanofibers can be synthesized close to room temperature [65, 66]. The electrical transport properties of the fibers are governed by a hopping-like conductance [67] operative in all fibers. This represents a clear advantage over carbon nanotubes, as the latter can be either metallic or semiconducting. Crystalline V_2O_5 is a catalyst material used e.g. for the oxidation of carbon monoxide [68,69], the production of methanethiol from CO_2 and H_2S [70], and for converting NO and NH_3 into N_2 and water [71]. The catalytic properties of V_2O_5 have recently been reviewed by Weckhuysen and Keller [72].

As the V_2O_5-nanofibers are not as prominent as the carbon nanotubes, the synthesis and characterization of this material will be described in chapter 3. After a brief introduction of the structure of V_2O_5 bulk crystals and V_2O_5-nanofibers, the regular synthesis route to V_2O_5-nanofibers [73] is described. Two different modifications of the standard approach have been devised. The first one utilizes silver ions to increase the fiber growth speed (chapter 3.1), while the second method is based on hydrothermal synthesis (chapter 3.2), which yields nanobelts in the shape of a boomerang. Regular V_2O_5-nanofibers are compared to the two modifications in chapter 3.3 as a pre-requisite for elucidating the sensing mechanism in the forthcoming chapter.

The sensing properties of V_2O_5-nanofibers are presented in chapter 4. The Langmuir adsorption theory is introduced to describe the interactions of V_2O_5 with ammonia (chapter 4.1). Butylamine is used as an exemplary analyte close to real-world application, as this compound is for example formed in rotten fish (chapter 4.2). A hydrogen sensor has been obtained via evaporation of palladium on the nanofibers, which shows tremendous changes in resistance (chapter 4.3).

The second material used in this thesis are the well-known carbon nanotubes. Since their discovery in 1991 by S. Iijima, nanotubes have been studied in great detail, catalyzed by their commercial availability. Important details can be found in various books and reviews on this topic [74–78]. The sensing behavior of carbon nanotubes will be discussed in chapter 5. First, the interaction with ammonia will be considered (chapter 5.1), followed by the description of their selective modification with palladium via electrochemistry to achieve a high sensitivity towards hydrogen (chapter 5.2).

Many characterization techniques have been applied to shine light on the sensing mechanisms. The experimental details, together with a description of the sensor devices and the gas sensing setups are given in chapter 2.

The experimental results are summarized and compared to the literature in the conclusion (chapter 6). Based on the structure of the thesis, the goals of this work can be summarized as:

1. Synthesis of appropriate nanowires as sensor components.

2. Fabrication of resistive gas sensors for room temperature operation.

3. Modification of these sensors to increase their sensitivity and selectivity.

4. Investigation of the fundamental sensor mechanisms.

Chapter 2

Experimental

In this chapter, the most important details of the employed experimental methods are presented. Not included are the fabrication procedures of the sensors, as they varied from one analyte to the other. Hence, the corresponding experimental details are combined with characterization of the V_2O_5-nanostructures and the sensor results (chapter 3–5).

Several characterization techniques (chapter 2.1) were employed to get a deeper insight into the morphology of the materials used for gas sensing. These techniques included atomic force microscopy and scanning electron microscopy. X-Ray diffraction (XRD) and (scanning) transmission electron microscopy ((S)-TEM), including energy-dispersive X-ray analysis (EDX) and selected area electron diffraction (SAED), gave information on the crystal structure and chemical composition of V_2O_5-nanofibers. Raman-spectroscopy and thermal desorption spectroscopy was used to get a deeper insight into the sensing mechanism.

Different types of sensor devices (chapter 2.2) were needed to electrically contact V_2O_5-nanofibers and carbon nanotubes. For the sensing experiments, two different setups were used. The first is based on a dilution of the test gas with a reference gas, while the second is based on an UHV chamber. In the later case, gas is introduced in small amounts into the chamber. Furthermore, the chamber is equipped with a source of atomic hydrogen, that was needed for the detailed analysis on the interactions of hydrogen with palladium-modified V_2O_5-nanofibers. In addition, temperature dependent transport properties can be performed under UHV conditions to avoid the condensation of water onto the sensor-devices.

2.1 Characterization methods

2.1.1 Microscopic imaging techniques

Atomic force microscopy (AFM, [79]) was used to visualize nanowires and the sensors made out of them. For this purpose a Nanoscope IIIa (Digital Instruments) was operated in the tapping mode using silicon-tips with a resonance frequency of ∼300 kHz.

A field-emission scanning electron microscope (FE-SEM, LEO 1530) operated at 10 kV was used to study the V_2O_5-sensor devices (Figure 1.2 .

The high temperature products (Figure 3.8) obtained from the hydrothermal synthesis of VO_x-nanobelts were examined with a Tescan Vega-TS 5130MM Scanning Electron Microscope (SEM) operated at 20 kV.

2.1.2 X-Ray diffraction and transmission electron microscopy

Powder diffraction measurements (XRD, [80]) were performed on roughly 100 mg of powder with the Cu-Kα line (λ=1.54 Å). A linear position sensitive detector was used to detect the scattered beam (Stoe, Darmstadt). The spectra were integrated over a timespan of 2.5 hours.

Transmission electron microscopy (TEM, [81]) and energy-dispersive x-ray analysis (EDX, [81]) were used for the characterization of Ag-V_2O_5 (chapter 3.1). A Tecnai G2 F20 S-Twin Mat (FEI Company) was utilized for this purpose, which is equipped with a High Angle Annular Dark Field (HAADF, Fischione, Model 3000, [82]) detector and an EDX-detector (EDAX). Ag-V_2O_5 nanofibers were deposited on a carbon-coated copper grid (400 mesh) via dip-coating for 30 sec.

For the investigation of the VO_x-nanobelts (chapter 3.2) a combined TEM and SAED study was performed in a Philips CM30/ST (300 kV) equipped with a LaB_6 cathode. The SAED patterns were performed with the aid of a diaphragm which limited the diffraction to a selected area of 250 nm in diameter. TEM and SAED patterns were recorded with a Multiscan CCD Camera (Gatan).

2.1.3 Raman spectroscopy

Raman spectroscopy [83] is a powerful technique to access the vibrational features of many materials. As vibrational spectra are related to the crystal lattice, information on the structure of a certain material can be gathered, including the perfection of the crystal.

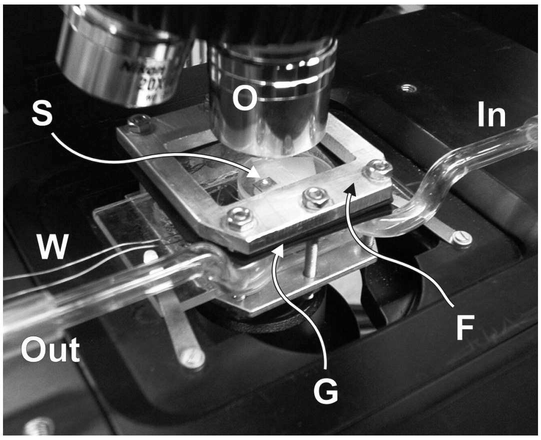

Figure 2.1: Glass cell attached to the Raman spectrometer with objective (O). The glass cell is composed of a quartz cover, a gasket (G), a frame (F), two tubes (In, Out) and two wires (W). The sample (S) is placed inside of the cell.

Raman spectra were acquired with a commercial single grating (1800 lines) spectrometer Labram 010 (Jobin Yvon), utilizing a He-Ne-laser with a wave length of 632.8 nm for excitation. The power of the laser (4 mW) was reduced to $\sim$1 mW with a D0.6 filter in order to avoid radiation damage of the material. The laser was focused onto the sample through a 50× objective (Nikon) with a working distance of 13.8 mm. The objective was also used as collecting lens for the spectrometer (backscattering geometry). For all spectra, the accumulation time was 90 sec. The materials analyzed by Raman spectroscopy were deposited from solution on a gold covered (100 nm) SiO_2/Si-wafer. A gold layer was chosen to avoid interference by Raman signals from the Si-wafer.

To measure changes in the vibrational spectra induced by the interaction with certain gases, a sealed glass cell ($\sim 4 \times 3 \times 1$ cm^3) has been constructed (Figure 2.1). Quartz is used for the top plate to minimize laser absorption and undesired Raman scattering from the cover. Sealing of the top plate has been achieved with a thin rubber foil, that is used as gasket. The cover has been connected to the cell via an aluminum frame. The glass cell is equipped with two tubes that have valves attached to it (not shown). The cell can be operated with a constant gas-flow (valves opened), or as a sealed setup, filled with a certain gas. In addition two copper wires reach into the compartment to allow for a simultaneous measurement of resistance of the device. The long working distance of the objective is needed to focus the laser beam onto the sample within the glass cell.

2.1.4 Thermal desorption spectroscopy

Thermal desorption spectroscopy (TDS, [84]) –used to evaluate the gas kinetics of ammonia on carbon nanotubes (chapter 5.1)– was performed in an UHV chamber with a base-pressure of $1 \cdot 10^{-10}$ mbar. The temperature of the sample holder attached to a continuous helium flow cryostat could be varied between 30 K and 1200 K, and was measured with a type K thermocouple. Details on the experimental setup can be found in the thesis of H. Ulbricht [85].

The high temperature of 1200 K was used to degas the purified SWNT-paper [64] (tubes@rice, Houston, Texas), in order to remove residual solvents and functional groups originating from the purification process. For the desorption experiments, 15 μm thick bucky paper was used which consists of ropes of single wall carbon nanotubes with a typical bundle diameter of 30 nm. Thermal Desorption experiments were also performed on highly oriented pyrolytic graphite (HOPG) for comparison.

Ammonia was admitted to the sample via a pinhole doser, giving rise to an incident gas flux of 10^{-11} mol s^{-1} cm^{-2}. Adsorption of ammonia (99.99 % purity) was performed at a sample temperature of 40 K. The duration of the gas flux was varied to give different gas coverages. The quantity of gas coverage is given in units of monolayers on SWNT ($1\ ML_{SWNT} \equiv 9.25 \cdot 10^{15}$ molecules/cm^2) and monolayers on graphite ($1\ ML_{gra} \equiv 1.85 \cdot 10^{13}$ molecules/cm^2), as calibrated with Xe adsorption [86]. A monolayer is the gas quantity needed to cover the surface completely. The relation $1\ ML_{SWNT} \approx 500\ ML_{gra}$, demonstrates the huge specific surface area of the SWNT sample, as compared to graphite. The sample was subsequently heated at a rate of 2 K/s and 1 K/s for SWNT and graphite, respectively, and the rate of desorption was measured with a quadrupol mass spectrometer.

2.2 Sensor devices and gas sensing equipment

2.2.1 V_2O_5-nanofiber sensors

V_2O_5-nanofibers can be synthesized via a wet chemical route, developed by Livage and coworkers [65, 66, 87]. Muster et al. [73] have been able to disentangle the xerogel network ($V_2O_5 \cdot n\,H_2O$) to yield individual nanofibers with a width of 10 nm, a height of 1.5 nm, and length of several μm. For the preparation 0.2 g ammonium(meta)vanadate NH_4VO_3 (Fluka) and 2 g acidic ion exchanger resin (Dowex 50 WX 8, Fluka) were dissolved in 40 mℓ of water, giving rise to an orange-colored sol. The solution has to be kept at ambient conditions to yield fibers of sufficient length. V_2O_5-nanofibers synthesized in this manner will be referred to as "regular V_2O_5-nanofibers".

If not stated otherwise, the sensors comprising V_2O_5-nanofibers were implemented on chips 2.5×1 cm^2 of BK7-glass, as depicted in the inset of Figure 2.2. Optical lithography was employed to write four electrode-pads and three sensor arrays. A thickness of 95 nm of gold was used on top of 5 nm titanium as adhesion layer for the electrodes. Each sensor array (Figure 2.2, dashed box of the inset) is composed of 50 interdigitated finger-pairs, with a width and separation of 10 μm and an overlap of 1800 μm.

For depositing the V_2O_5-nanofibers onto the chip, the glass substrate was amino-silanized utilizing N-[3-(trimethoxysilyl)propyl]-ethylene diamine (1:1000 H_2O, 2 min). The chip was then placed for 20 sec in a 1:10 diluted suspension of V_2O_5-nanofibers. Examples of V_2O_5-nanofiber networks can be found in Figures 1.2, 4.1(a), 4.11(a). The electrical resistance of the devices was found to be $\sim$10 kΩ at room temperature.

The networks were modified by evaporation of a metal to a nominal thickness of

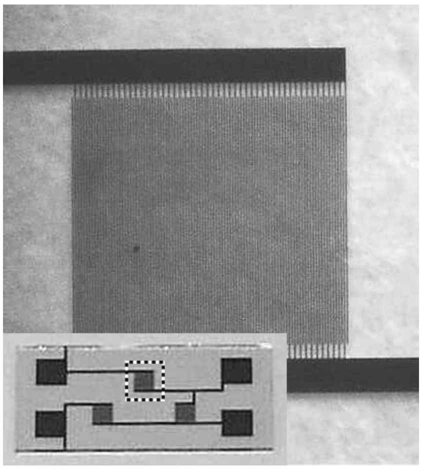

Figure 2.2: Sensor chip used for the experiments with V_2O_5-nanofibers. The inset displays the actual chip, while the main figure shows one sensor array.

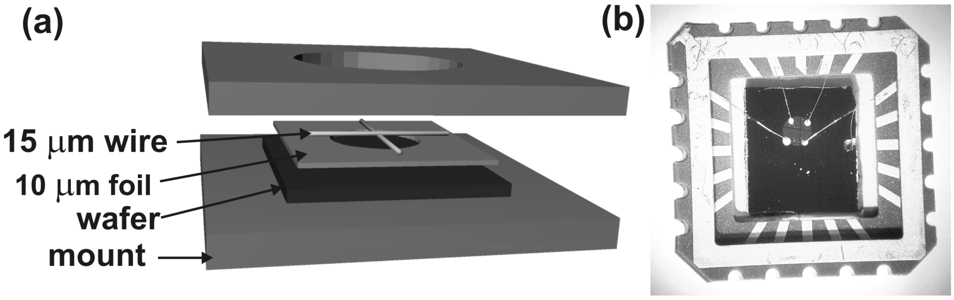

Figure 2.3: (a) Schematic of the mount used for the production of nanotube sensors with shadow mask technique. (b) Nanotube-sensor in a chip carrier.

1 nm. In the case of gold, cluster formation was observed (Figure 4.1(b)), while a homogeneous coverage was obtained with palladium (Figure 4.11(b)). For experiments in UHV, a single sensor array was cut from the sensor-chip and placed in a commercial chip carrier, where it was bonded.

2.2.2 Nanotube sensors

Purified HiPCo material (Carbon Nanotechnology Inc., Houston, Texas) was dispersed in aqueous solution containing 1 wt% lithium dodecyl sulfate (LDS, Fluka). Purification was achieved by ultrasonic treatment (30 pulses of 30 W power; UP 200S, Dr. Hielscher GmbH) to debundle nanotubes from ropes, followed by centrifugation (14,000 rpm, 30 min; Eppendorf Centrifuge 5417C). These two steps were repeated on the decanted sample to increase the purity of the nanotubes. A Si/SiO_2-wafer was treated with an amino silane, similar to the preparation of the V_2O_5-sensors (chapter 2.2.1). The wafer was subsequently dipped into the decanted nanotube solution for ∼2 hours. After removal of the wafer from the nanotube solution, it was dried under a stream of nitrogen. This drying procedure ensured the permanent attachment of nanotubes to the wafer. Finally, the wafer was carefully rinsed with water to remove any residual of the surfactant. It is important to note, that only a too small amount of nanotubes remained on the wafer, if the wafer was rinsed prior the drying procedure.

The electrical contacting of carbon nanotubes required special care. Gold or gold-palladium electrodes were used in order to avoid the formation of Shottky barriers [54], and therefore no adhesion layer was permitted. To minimize the contact resistance, the electrodes had to be evaporated on top of nanotube-networks.

In the gas sensing experiments it was found, that no distinct sensor response could be obtained, if the electrodes were defined on top of the nanotubes via e-beam or optical lithography. This observation was attributed to residual resist layer.

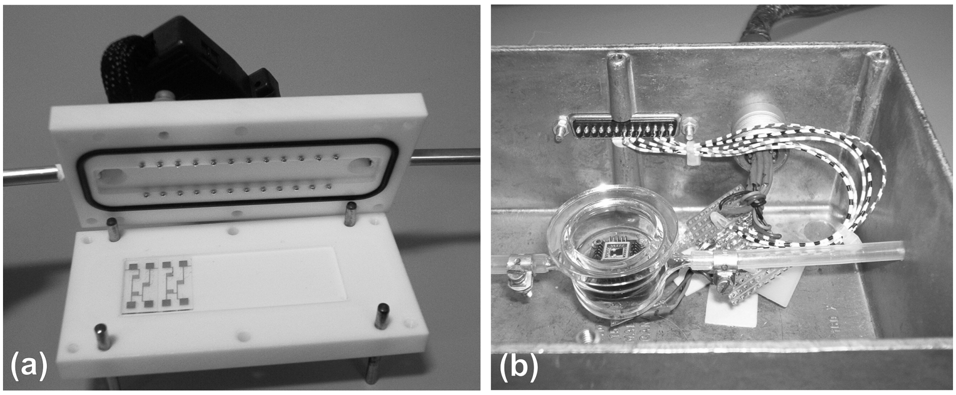

Figure 2.4: (a) Teflon cell used for the experiments with V_2O_5-nanofiber sensors. (b) Open glass cell used for sensor experiments with carbon nanotubes, which have been placed inside a chip carrier.

In order to overcome this problem, evaporation with a shadow mask technique has been used for the preparation of the nanotube sensors. Two crossed wires are used as shadow mask to yield four electrodes with a separation of $\sim$20 μm (Figure 2.3(a)). A thin foil (10 μm thickness) with a 1 mm hole is used as a spacer between wafer and the wires. The spacer is essential to avoid contamination of the nanotube network from the crossed wires. In addition, the hole in the foil restricts the length of the electrodes to $\sim$500 μm. Two copper plates are used as mount, pressing the setup together with the aid of three screws (not shown).

After evaporation of 100 nm gold, the wafer was glued into a chip carrier (9×9 mm^2, Figure 2.3(b)). Since no adhesion layer was used prior evaporation of gold, direct bonding could not be performed. Instead, the bonding wires were glued with silver-paste onto the four electrodes. The electrical resistance of the devices depended on the local density of nanotubes and was found to be 5–20 kΩ.

2.2.3 Dilution system

Experiments with V_2O_5-nanofibers were performed in a teflon cell that is capable to hold six chips, each comprising three sensor arrays (Figure 2.4(a)). Gold pins in the cover are used for contacting the electrode pads of the sensors. For experiments with nanotubes, a glass cell (Figure 2.4(b)) was replacing the teflon cell, to account for the different sample geometry. A corresponding mount for the chip carrier was glued into the cell and six connections were made to an exterior switching box.

Appropriate gas- and vapor-mixtures were generated with a mass flow system (Kalibriersystem MK5, Umwelt Technik MCZ). The same system was also used to switch be-

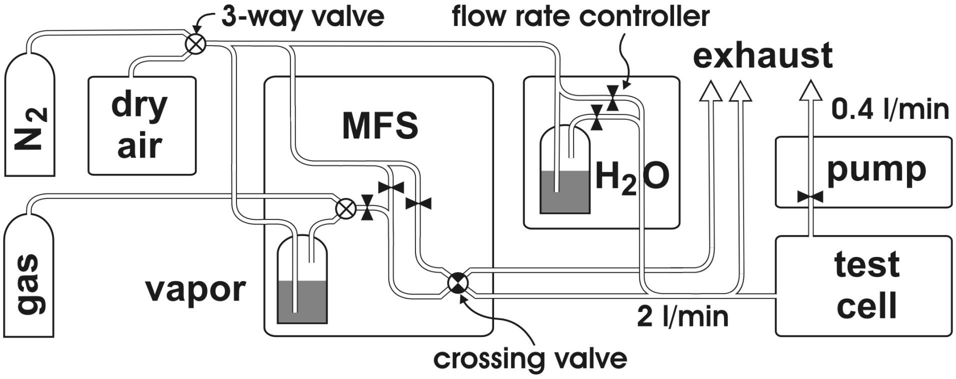

Figure 2.5: Schematic of the mass flow system (MFS) to dilute test gases and vapors with nitrogen or dry air. H_2O indicates the humidifier.

tween test and reference gas[1]. Gases were supplied from bottles containing 1 % or 10 % of the gas diluted in nitrogen. Vapors were generated via bubbling of carrier-gas through a vessel kept at ∼30°C followed by cooling of the super-saturated vapor to 20°C. Gases and vapors could be diluted with pure nitrogen or dry air (Figure 2.5).

If desired, a certain relative humidity could be added to the system via a humidifier (Umwelt Technik MCZ), whose gas stream was added after the mass flow system in order to humidify both the test and the reference gas. The total flow of test and dilution gases was adjusted to 2 ℓ/min. In order to avoid pressure effects during switching between gases, a fraction of 0.4 ℓ/min was pumped over the sensor device. The concentrations of the test gas are always given as fraction of the total amount of gas, the corresponding unit is part-per-million (ppm).

As an illustrative example, the appropriate settings for gas mixtures are exemplified in the following for the generation of 1 ppm butylamine at 20 % relative humidity with a flow-rate of 2 ℓ/min: As butylamine has a vapor pressure of 76 mbar, the saturated vapor contains 76,000 ppm butylamine (=76 mbar butylamine/1000 mbar dry air). As a final concentration of 1 ppm is desired, the saturated vapor has to be diluted by a factor of 76,000. The total flow should be adjusted to 2 ℓ/min, therefore 0.026 mℓ/min of saturated butylamine vapor have to be added to the mixture. The water vapor from the humidifier contains 80 % relative humidity (rh)[2]. In order to achieve 20 %rh it has to be diluted 1:3 (0.5 ℓ:1.5 ℓ) with dry air. Therefore 1.5 ℓ of dry air have been used

---

[1] A crossing valve was used for this purpose, which gave either the test or the reference gas onto the test cell, while the remaining gas was redirected to the exhaust. With this setup a continuous flow of all gases/vapors was achieved, which e.g. avoided a super-saturated vapor in the mass flow system.

[2] In principle 100 % rh are possible, but the humidity was limited to 80 % to avoid a condensation of water in the tubes.

to pre-dilute the 0.026 ml/min of butylamine vapor, giving an intermediate butylamine concentration of 1.33 ppm. Afterwards, the 1.5 ℓ/min butylamine/dry air gas were mixed with 0.5 ℓ/min of water vapor (80 %rh).

2.2.4 UHV chamber

An UHV system (Figure 2.6(a)) was built up and used for electrical transport measurements and gas sensing experiments with atomic hydrogen. The system consists of a main chamber and a loading dock separated with a gate valve. A Trivac D30A (Leybold-Heraeus) is used as roughing pump for both chambers. The pressure in the roughing system ($\sim 10^{-2}$ mbar) is controlled with Thermovac gauges, while ultra high vacuum pressures in both sub-systems are monitored with cold cathode gauges (IKR 270, Pfeiffer).

The loading dock consists of a CF-100 double-cross equipped with a turbo molecular pump (Turbovac 151, Leybold-Heraeus), a quick lock door and a magnetic wobblestick used for the transfer of the sample into the main chamber. A vacuum of $\sim 10^{-8}$ mbar in the main chamber is achieved with a Turbovac 361 (Leybold-Heraeus). The main chamber (∅ 300 mm, h=530 mm) is equipped with two leak valves allowing to dose gases into the system (on the backside of the apparatus, not shown). One of these leak valves is equipped with a nozzle in order to achieve a 50-fold increase in gas-pressure[3] at the position of the sample. In addition, a source for atomic hydrogen is attached to the main chamber. A tungsten-filament (70 mm×8 mm×25 μm) is heated to ~2000 K with an external power-source (9 V, 33 A). A flow of hydrogen is controlled with a leak-valve and atomic-hydrogen is generated on the surface of the heated tungsten-filament. Details on the source of atomic hydrogen can be found in the thesis of O. Kern [88].

A helium flow cryostat (VAB Vakuum Anlagen Bau) is used for temperature control (~100–500 K) of the sample and is mounted on a rotatable xyz-stage, to move the sample in the transfer- or the sensor-position. The cryostat is equipped with ten electrical feedthroughs used for transport-measurement, additional feedthroughs are present to control the temperature of the sample-holder (Pt-100) and the cryostat (thermocouple, type K).

For transferring the sample into the system without loosing the vacuum in the main chamber, a special sample holder was constructed (Figure 2.6(b)). The body of the sample holder ($\sim 45\times 22\times 10$ mm^3) is made of copper and can be attached to the cryostat with the aid of a screw. The screw is fixed to the sample holder enabling its free

---

[3] The factor 50 has been obtained from sensor experiments, during which the sensor was alternatingly exposed with the regular and the high-doser at various pressures in the chamber.

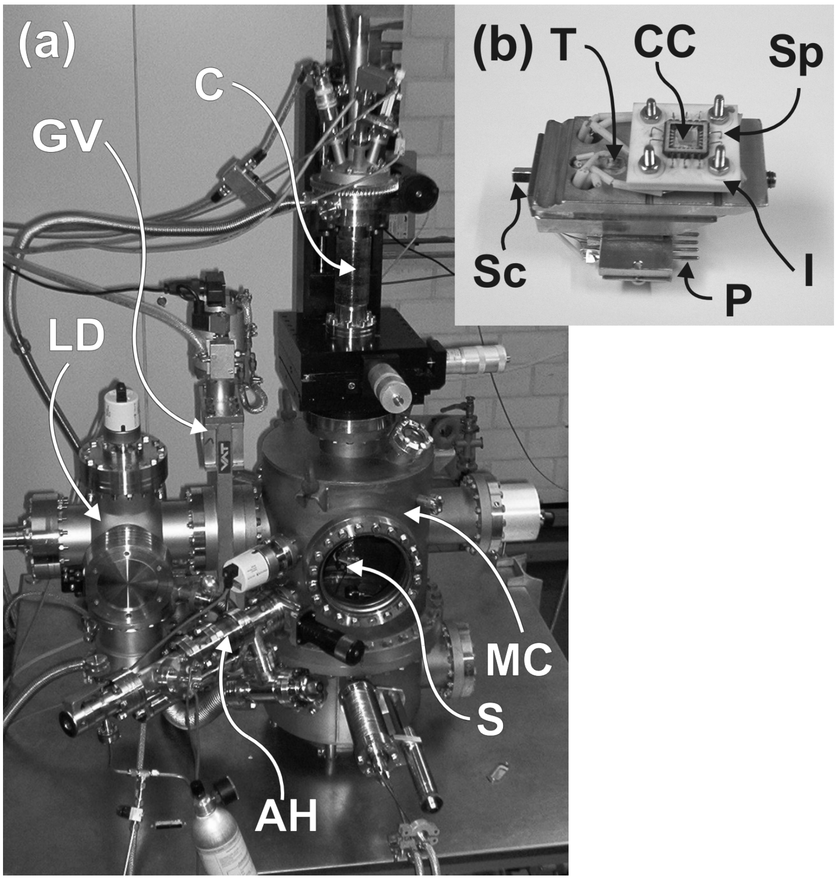

Figure 2.6: (a) UHV chamber composed of a loading dock (LD), gate valve (GV), and main chamber (MC). The system is equipped with a cryostat (C) with a sample (S) attached to it and a source for atomic hyrogen (AH). (b) Sample holder attached to the cryostat via a screw (Sc). Electrical contact to the chip carrier (CC) is achieved via 12 pins (P) and 10 springs (Sp), which are isolated from the body via an aluminum-oxide layers (I). The temperature is measured with a Pt-100 resistor (T).

rotation, while the translation is prohibited. Due to this rigidity, it is possible to remove the sample holder, while unscrewing the device. Electrical connection between sample holder and cryostat is achieved via twelve pins on the backside. Ten of these wires are connected with corresponding CuBe springs, which hold and contact the chip carrier. The remaining pins are connected to a Pt-100 resistor in order to measure the temperature of the setup with an external Keithley 2000 multimeter. The resistor is glued into a trench of the corpus to achieve a good temperature coupling. Two plates of aluminum-oxide are used to electrically insulate the chip carrier from the corpus, while allowing a good temperature coupling at low temperatures. Trenches and holes are made into the plates for positioning the springs.

2.2.5 Electrical transport measurements

The measurement of the electrical transport properties of V_2O_5-nanofibers and carbon nanotubes is the major characterization technique used throughout this thesis. Due to the reduced dimension of the sensor material, special emphasis has been put on the experimental setup, to avoid electrical shocks, which can destroy the nanowire.

Therefore manually operable switching boxes are employed between the sensor setups and the measurement units. They allow for selecting the wanted electrodes on the sensor-chips, and ground the networks, while not used for measurement. Any currents or voltages applied to the V_2O_5-nanofibers or carbon nanotubes were not switched on rapidly, but were ramped from zero to the desired value within 5–10 seconds. Furthermore, the measurement range of the employed multimeters was adjusted and fixed prior the actual experiment, while the sample was still grounded. This procedure allows to obtain an optimal signal-to-noise ratio without the danger of destroying the sample.

For experiments with the dilution unit (chapter 2.2.3), a constant current was applied with a sourcemeter (SMU 236, Keithley). The current was adjusted to give rise to a voltage of $\sim$100 mV prior gas exposure. The voltage was monitored with a Keithley multimeter 2002. Due to the higher electrical stability of V_2O_5-nanofibers compared to carbon nanotubes, the manual switching box could be replaced with an internal switching unit within the Keithley 2002.

Due to the electrical feedthrough from the sample to the exterior via the sample-holder and the cryostat, electrical transport measurements are also possible within the UHV-chamber (chapter 2.2.4). The setup allows to perform temperature dependent transport measurements, transport characteristics, and sensor experiments as a function of time and gas pressure. In analogy to the experiments with the dilution unit, a manually operated switching box is employed to select the corresponding channel and to ground unused connections. The resistance of the V_2O_5-nanofiber and carbon nanotube networks is measured with a Keithley 2400 sourcemeter.

In contrast to the experiments with the dilution unit, gas-sensing experiments within the UHV-chamber are performed at fixed bias voltage (100 mV) to account for the different measurement system.

For the temperature-dependent I-V characteristics of the various V_2O_5-nanostructures, the voltage was ramped from zero to V_{max}, to $-V_{max}$ and back to zero to avoid electrical shocks to the sample. Appropriate values for V_{max} were chosen based on the actual temperature of the sample. The measurement range of the current was adjusted accordingly.

Chapter 3

Synthesis & Characterization of V_2O_5-structures

The synthesis of conventional V_2O_5-nanofibers has been extended by two modifications. Firstly, silver ions have been utilized in order to increase the growth speed of V_2O_5-nanofibers. This new synthesis route will be introduced in chapter 3.1. The composition of the material has been evaluated by EDX spectroscopy. Secondly, an hydrothermal approach has been applied as alternative approach to enhance the growth speed. The hydrothermal treatment gave rise to boomerang-shaped VO_x-nanobelts, which have been analyzed with powder XRD and SAED to unravel the crystal structure of the "L" (chapter 3.2). A detailed comparison was made between all three types of material, including Raman spectroscopy and electrical transport measurements (chapter 3.3).

The crystal structure of V_2O_5-nanofibers, can be best understood from its relation to crystalline V_2O_5, which is depicted in Figure 3.1(a). Its structure is composed of individual layers, linked together via weak V- -$O_{(1)}$ forces (dashed lines), where $O_{(1)}$ refers to the vanadyl oxygen, sticking out of the layer. The orientation of this type of oxygen alternates above and below the layer. Each layer is composed of double chains of vanadium-oxide (V,V',$O_{(3)}$), containing a triple coordinated oxygen $O_{(3)}$. The double-chains are linked to each other via bridging oxygen $O_{(2)}$. Buckling of the chains have been omitted for illustrative purposes. Alternatively, V_2O_5 can be regarded as being composed of VO_5 pyramids with a vanadium-atom in the center, $O_{(2)}$- and $O_{(3)}$-atoms in the base and the $O_{(1)}$-atom at the apex. The bulk crystalline structure is composed of corner- ($O_{(2)}$) and edge-sharing ($O_{(3)}$) pyramids.

Two models are reported in the literature on the crystal structure of V_2O_5-nanofibers. The first model for V_2O_5-nanofibers (Figure 3.2(a)) is in close relation to V_2O_5-crystals. Different from V_2O_5-crystals, the layers in V_2O_5-nanofibers are separated by water

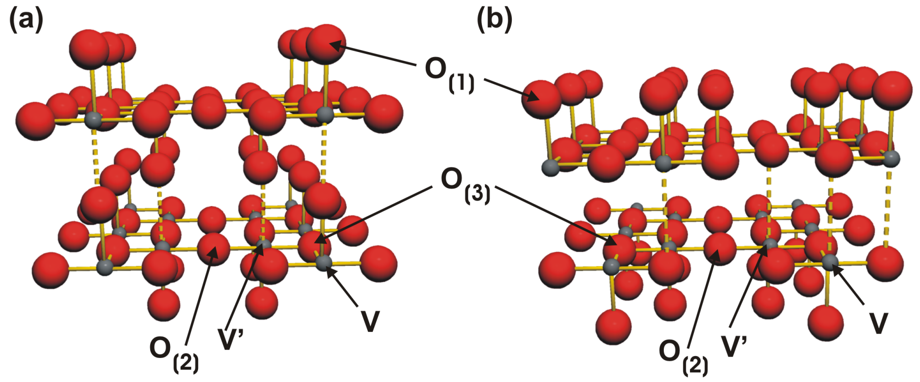

Figure 3.1: Model of (a) crystalline V_2O_5 and of (b) bilayer present in V_2O_5-nanofibers and xerogel. The growth direction of the fibers points perpendicular to the Figure. The dashed lines correspond to weak interactions of adjacent layers.

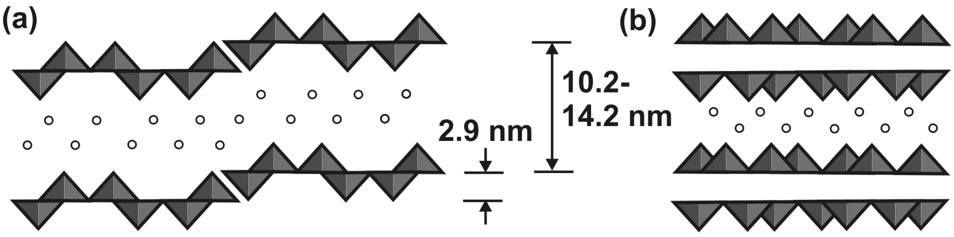

Figure 3.2: Two models for the incorporation of water (circles) into the V_2O_5 structure.

molecules [87]. The layer separation can vary between 10.2 Å and 14.2 Å, as has been found in XRD data. In addition, a stacking fault with a step height of 2.9 Å is added to the model to account for experimental findings.

The second model proposed by Yao et al. [89] assumes a bilayer structure as depicted in Figure 3.1(b). The distance between the two layers is 2.9 Å. Each layer is identical to the one found in crystalline V_2O_5 (Figure 3.1(a)), except for the orientation of the vanadyl oxygens $O_{(1)}$, which always point outwards of the bilayer arrangement. The layers are shifted relative to each other in order to couple V- and O-atoms of neighboring layers. Two of these bilayer are stacked together, separated by a multitude of water layers in between, see Figure 3.2(b). The number of the water layers and therefore separation of the bilayer depends on water content of the material. Based on a recent XRD study with high energy X-rays [90], this model seems to be valid for xerogels and V_2O_5-nanofibers and will be used throughout this thesis.

3.1 Ag-doped V_2O_5-nanofibers

A major disadvantage of the low temperature (e.g. at room temperature) preparation method for V_2O_5-nanofibers (see chapter 2.2.1) is the long time required to grow fibres of sufficient length. To produce fibers with a length exceeding 5 μm, in order to bridge neighboring electrodes prepared with optical lithography, a time span of 1–2 months is needed. Ag-ions have been found effective in reducing the synthesis time, while preserving the simplicity of the method.

For the synthesis, first 15 mg silveracetate (90 μmol, Aldrich) have been dissolved in 80 mℓ H_2O. 100 $\mu\ell$ of vanadium-oxytriisopropoxide $OV(OC_3H_7)_3$ (420 μmol, Aldrich) as V-precursor have then been added in order to obtain an Ag/V ratio of 20 %. The solution was heated for 5 min at 70°C until dissolution occured, giving rise to an orange solution. Afterwards, the solution was kept at ambient conditions. To compare the growth speed of the Ag-V_2O_5-nanofibers, to previous synthesis routes, a reference sample was prepared without the silveracetate. For this purpose, the same V-precursor was used, however, at an increased concentration of 400 $\mu\ell$ $OV(OC_3H_7)_3$ dissolved in 80 mℓ of water, since at lower vanadium concentrations no fibers could be found in the solution.

Fibers of the silver-modified and the reference sample with different ageing times were deposited on an amino-silanized SiO_2/Si-wafer, identical to the preparation of V_2O_5-sensors (chapter 2.2.1). Figure 3.3(a) shows an AFM image of Ag-V_2O_5-nanofibers with an age of 9 hours. While the width of the fibers appears to be constant, the height varies significantly. Two types of fibers are present: The ones which appear brighter have a

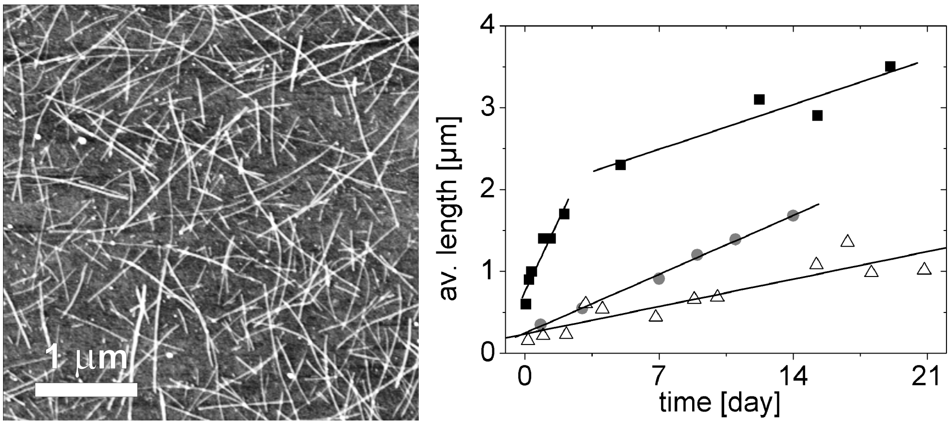

Figure 3.3: (a) AFM image of a 9-hour-old Ag-V_2O_5-sample. (b) Average length of Ag-V_2O_5-fibers as a function of sample age (closed squares) compared to V_2O_5-fibers grown without Ag-ions (open triangles). The lines have been added as guide to the eye.

height of ~2.7 nm, while the remaining fibers have a thickness of ~1.6 nm. The value of 1.6 nm is in close agreement to 1.5 nm observed previously for regular fibres [73, 91]. The increased height of 2.7 nm for the remaining fibers can be understood from the layered structure of the material, in which an additional vanadium-oxide double layer has been added to the structure of regular fibers [89, 90, 92]. The average length of these fibers with an age of 9 hours has been found to be 1±0.6 μm.

In order to determine the growth of the fibers, a series of AFM images has been taken from samples with different age. The average length of Ag-V_2O_5-nanofibers is plotted in Figure 3.3(b) (squares) as a function of ageing time. The growth process appears to be divided into two regions, as indicated by the two lines in the graph. Up to 5 days, a fast growing initial phase with a rate of ~0.5 μm/day can be seen, which is followed by a reduced growth rate of ~0.08 μm/day.

In a similar fashion, the reference sample –V_2O_5 fibres grown without Ag-ions– has been analyzed. The length of the reference V_2O_5-fibers as a function of ageing time has been added to Figure 3.3(b) as open triangles, corresponding to a growth rate of ~0.043 μm/day. Despite the increased concentration of V-precursor used for the reference sample, the growth rate of the Ag-V_2O_5 is 10 times higher for the initial growth period, while it is still slightly higher for the second growth period ($t>5$ day).

For completeness, the average length of regular fibers, as introduced in chapter 2.2.1, has been added as grey circles to Figure 3.3(b). The growth speed is found to be 0.1 μm/day. Compared to the reference sample, an increased slope was observed, which is attributed to the presence of the ion exchanger. However, as a different V-precursor is used[1] for regular V_2O_5-fibers, the comparison to the reference sample and the Ag-V_2O_5 sample is only partially meaningful.

From Figure 3.3(b) it is evident, that the use of silver-ions enhances the speed of growth, although for larger times, the growth rate of the Ag-V_2O_5-nanofibers and the fibers of the reference sample approach equal values. While the growth rate of the reference fibers appears to be constant, this is not the case for the Ag-V_2O_5 sample. This effect may be explained with the limited presence of Ag-ions within the solution. In the initial growth phase, silver ions are able to enhance the speed of growth, while afterwards the ions are depleted, reducing the speed of growth to that of the reference sample.

---

[1] Vanadium-oxytriisopropoxide was used for the reference sample and the Ag-VO_x, while ammonium (meta)vanadate was used for the regular V_2O_5-nanofibers.

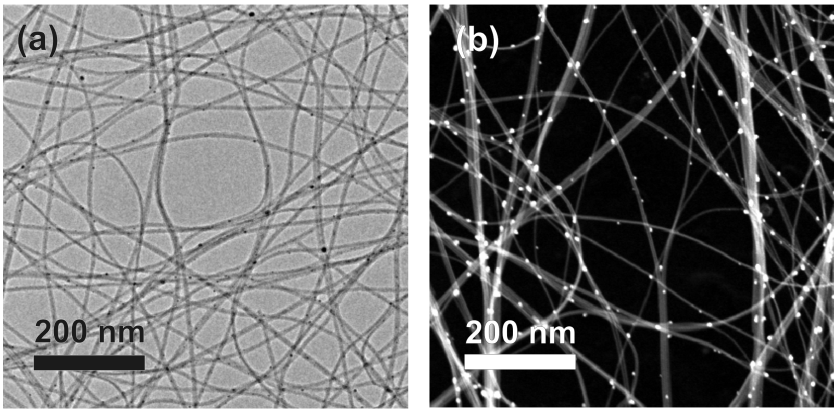

Figure 3.4: (a) TEM image of Ag-V_2O_5. (b) STEM image with HAADF detector at the same magnification.

3.1.1 Characterization

In order to elucidate the effect of the silver-ions on the fiber structure, measurements on a HAADF STEM (chapter 2.1.2) have been performed. Figure 3.4(a) shows a TEM image of the silver-doped fibers at low magnification. The TEM result confirms the uniformity of the nanofibers, e.g. each fiber has a constant width. However, the width of the fibers within the sample vary from 8–15 nm, in good agreement to a value of 10 nm, which is obtained for regular V_2O_5 nanofibers [73, 91]. It should be noted, that the lengths of the fibers displayed in the TEM image are larger compared to the fibers of the AFM image, as they have had a longer ageing time of ∼1 year. In order to increase the fiber-to-background contrast of the image, the TEM is operated in the scanning mode utilizing the HAADF detector. This novel technique [82] allows the detection of heavy elements. Besides a better contrast of the fibers, bright clusters become visible (Figure 3.4(b)).

To reveal the chemical composition of the fibers and the clusters, an EDX analysis has been performed on a similar spot (inset of Figure 3.5(a)). In a first step, the EDX spectrum (Figure 3.5(a)) has been obtained at the upper-right end of the cross sectional line, indicated in the inset. It reveals the presence of V, O, Ag, Cu, C, and traces of Si. Cu and C can be assigned to the copper grid, while Si is a common impurity. Therefore V, O, Ag originates from the sample.

In a second step, a line scan analysis has been performed along the line indicated in the inset of Figure 3.5(a). Note, that the line scan includes nanofibers (A), freestanding clusters aside of the fibers (B), and clusters on top of fibers (C). The energy window of the spectrum has been subsequently limited to 2.8–3.7 keV and 4.8–5.6 keV to be element specific to Ag- and V-atoms, respectively. The energy ranges are indicated as grey bars

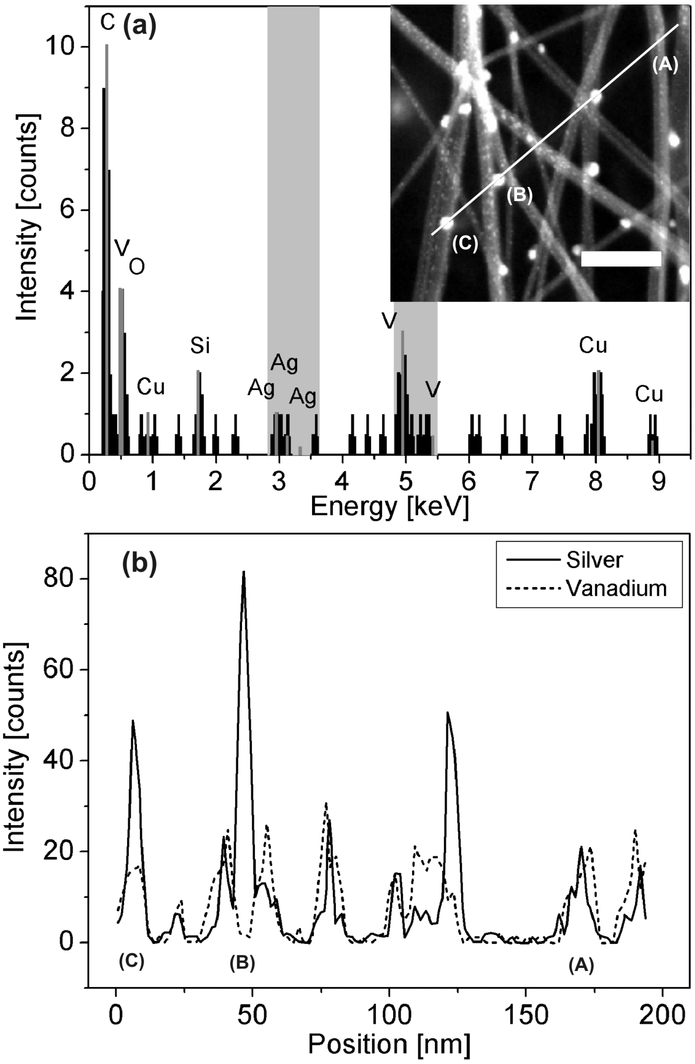

Figure 3.5: (a) EDX spectrum, taken at the upper-right end of the cross sectional line, as indicated in the inset. The grey bars indicate the energy ranges used respectively for the detection of Ag- and V-atoms in the line scan analysis of (b). Inset: STEM image of Ag-V_2O_5 (scale-bar equals 50 nm). The line is used for the line scans adjusted to V- and Ag-ions. Various positions are marked: isolated fibres (A), freestanding clusters (B), and clusters on top of fibres (C). (b) Line scan analysis of Ag-atoms (solid line) and V-atoms (dashed line) as indicated in the inset of (a), the markers (A-C) are those of the inset.

in Figure 3.5(a). Thus obtained line scan spectra of Ag and V are plotted in Figure 3.5(b) as solid and dashed lines, respectively. It is emphasized that equal peak intensities do not reflect a 50:50 composition of the material, since the measured intensities have not been normalized with respect to the cross sections of the corresponding elements.

At the position of the clusters, a high Ag-signal can be observed for all three clusters.

In addition, a V-signal is observed for the first and the third cluster (type C), but not for the second one (type B). As the cluster in the middle is attached next to the fiber (B), while the two other clusters (C) are positioned on top of the nanofibers, the V-signal can be attributed to the superimposed fiber, but not to the clusters themselves. Therefore the clusters are exclusively composed of Ag.

Positions without Ag-clusters (position (A)) show a strong signal from V, as expected for V_2O_5-fibers. In addition a non-vanishing signal of Ag is detected, demonstration that a small amount of silver is incorporated into the fibers. The formation of silver nanoparticles provides a further hint for the above suggested mechanism of the transition from a fast to a slow growth regime, since the silver of the particles should no longer be available for a promotion of the fiber growth.

The synthesis method allowing for in-situ decoration of V_2O_5-nanofibers with Ag-clusters represents an useful modification approach. The effect of these particles on the electronic properties of the fibers will be discussed in chapter 3.3.2.

3.2 Boomerang-shaped VO_x-nanobelts

Low temperature, solution phase synthesis represents an attractive approach towards nano-scale one-dimensional (1-D) materials of high crystalline order [93]. In contrast to pulsed laser vaporization [63] and chemical vapor deposition [94], which are frequently used to produce carbon nanotubes or semiconductor nanowires [95], solvothermal methods require temperatures of only 100–200°C. The latter methodology has proven highly versatile for the production of a wide range of 1D single-crystalline materials, including vanadium-pentoxide (V_2O_5) [96], molybdenum-trioxide (MoO_3) [97], cadmium-sulphide (CdS) [98], bismuth (Bi) [99], and perovskite-manganites ($La_{0.5}(Ba,Sr)_{0.5}MnO_3$) [100]. Depending on the presence of additives (as structural templates and/or reducing agents), as well as the reaction temperature and time, formation of vanadium oxide nanofibers [96] or nanotubes [101] has been observed. Here, hydrothermal synthesis has been utilized to reduce the growth time of V_2O_5-nanofibers below ~1 day.

3.2.1 Hydrothermal synthesis

For hydrothermal synthesis, 150 $\mu\ell$ of vanadium-oxytriisopropoxide $OV(OC_3H_7)_3$ (Aldrich) was added to 15 $m\ell$ of ultra-pure water at room temperature. The mixture was stirred for 3 min at 70–80°C until the formed, orange-colored gel had been completely dissolved. Then the solution was transferred into an autoclave cell (Teflon) of 20 $m\ell$ volume, and kept for 3.5 hours at 180°C. After cooling to room temperature, the greenish product[2] was deposited on a SiO_2/Si-wafer, using a similar procedure as for the preparation of V_2O_5-sensors (see chapter 2.2.1).

Although V_2O_5-nanofibers were expected from the hydrothermal synthesis, the product contained broad VO_x-nanobelts, as observed by atomic force microscopy (Figure 3.6(a)). Most striking is their appearance in the shape of a boomerang (or "L"), which is reproducibly observed for all objects. Analysis of a larger number of belts has shown that the internal angle between their arms is identical, with a value of 96°. Although the belts are of equal shape, they show a distribution in the width and length of their arms. For the present sample, the arm width amounts to 650±50 nm and the length varies from 2–4.5 μm. The end regions of the belts are round-shaped, and terminated by a relatively sharp tip. Such tapering at the ends, together with the fact that the two arms within each belt are of almost identical length, suggests that the crystal growth starts at the center of the kink, from where it simultaneously progresses along

---

[2] The green color of the solution indicates a partial reduction of the V^{5+}-precursor, therefore the term VO_x is used, rather than V_2O_5.

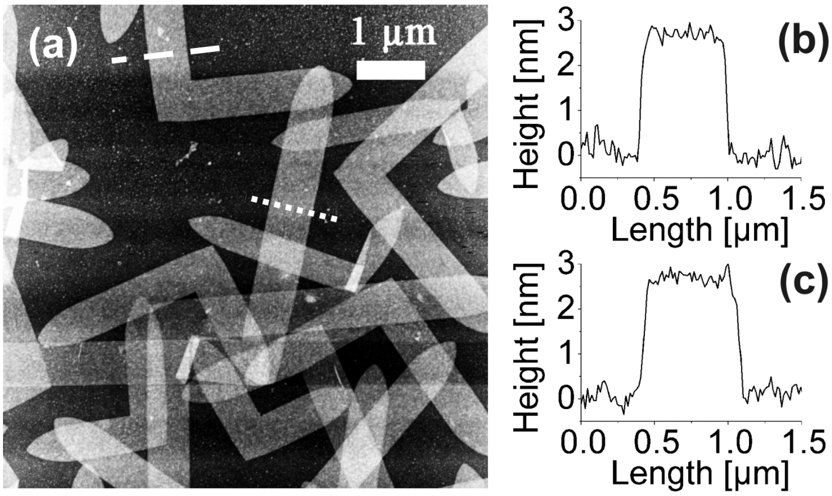

Figure 3.6: (a) Atomic Force Microscopy image of boomerang-shaped VO_x nanobelts. The height scale of the image is 10 nm. (b), (c) Averaged cross-sections of two nanobelts, as indicated in the AFM image with a dashed line (b) and a dotted line (c), respectively [102].

the two arm directions.

The nanobelts reveal a reproducible, uniform thickness of ~2.8 nm, as exemplified by the cross-sectional profiles in Figures 3.6(b), (c). This height is in close agreement to the value of 2.7 nm observed for the thick species of Ag-V_2O_5-nanofibers (chapter 3.1), which is composed of three double layers and two water channels. The regular thickness indicates a layered structure of the material [89, 90, 92] and will be discussed in more detail below (chapter 3.2.2).

The dimensions and morphologies of the hydrothermal product can be easily by changing the synthesis temperature, while holding the precursor concentration and duration of synthesis constant. The formation of boomerang-shaped nanobelts occurs in the temperature range of 150–210°C. From the respective AFM images (Figure 3.7) it becomes evident that with increasing synthesis temperature, the belts become wider

Table 3.1: Dimensions of the boomerang-shaped VO_x-nanobelts as a function of synthesis temperature.

synthesis temperature	average length	average width
150°C	3.2 μm	0.36 μm
180°C	2.9 μm	0.59 μm
210°C	1.4 μm	0.90 μm

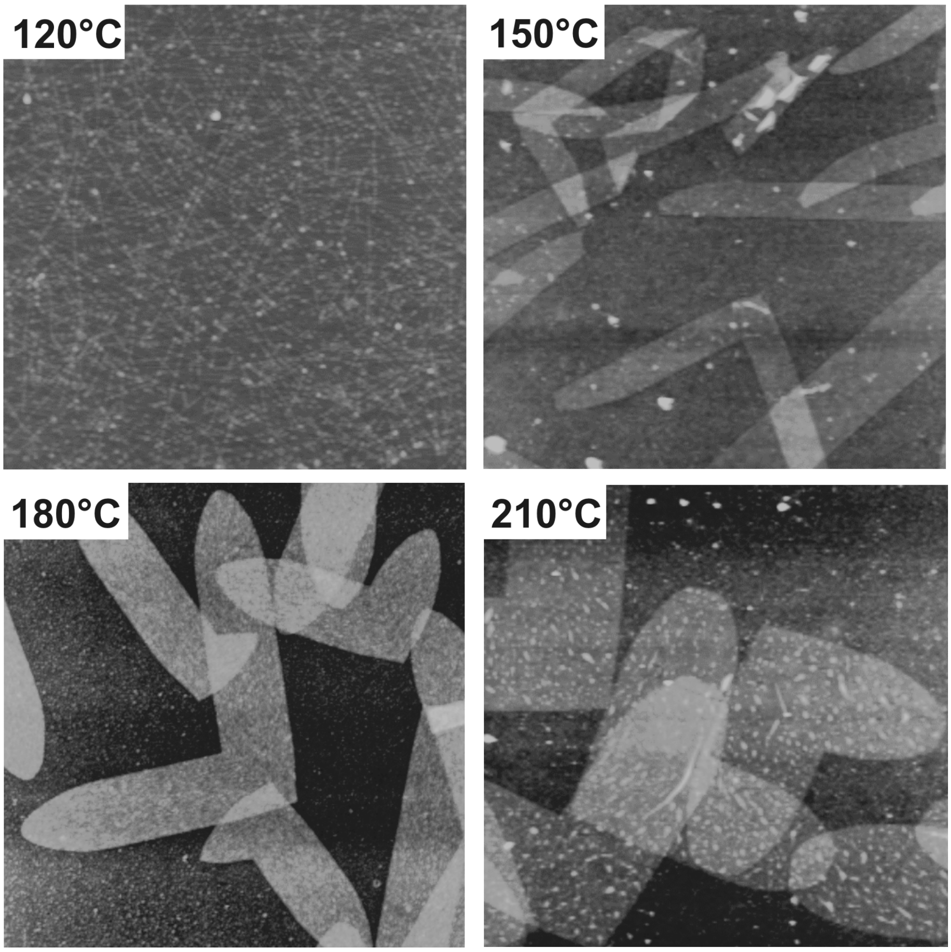

Figure 3.7: AFM image of hydrothermally synthesized VO_x-nanostructures, grown at various temperatures, as indicated in the figures. The size of the images is 4×4 μm^2.

and shorter. Table 3.1 summarizes the average dimensions as a function of synthesis-temperature. At a temperature of ∼120°C, non-uniform nanofibers are formed (upper left image of Figure 3.7). By contrast, when 250°C is used as temperature for the synthesis within the autoclave cell, a black solution is obtained. No clear AFM images could be obtained in this case, as the objects have heights exceeding 150 nm. The SEM image (Figure 3.8) of the high temperature product reveals the presence of long micro-crystallites with length exceeding 10 μm and width of ∼600 nm. The shape (increased thickness) suggest a modified stoichiometry, which is attributed to a chemical reduction of the V^{5+}-precursor, due to the high-temperature treatment. Such reduction has been observed also after heat treatment of thin V_2O_5-films in vacuum [103].

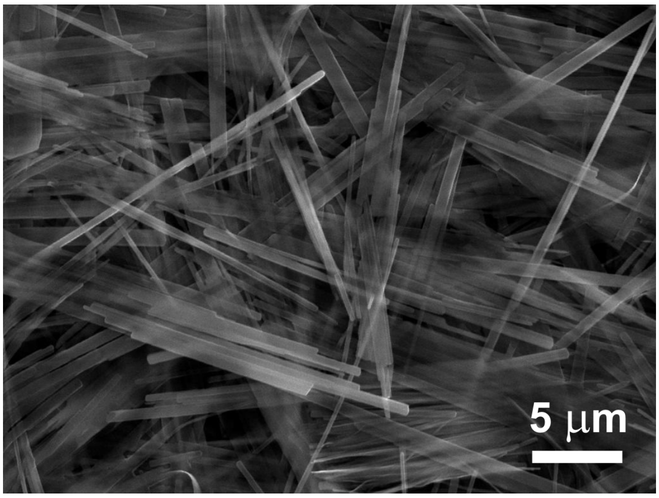

Figure 3.8: SEM image of microcrystallites, as obtained from the synthesis at 250°C.

3.2.2 Crystal structure

XRD measurements have been performed to evaluate the layered structure of the material. Powders (~100 mg) of regular V_2O_5-nanofibers and boomerang-shaped VO_x-nanobelts (synthesized at 180°C) have been obtained from evaporating the solutions to dryness at ~80°C. Spectrum (1) of Figure 3.9 shows the diffraction pattern of regular V_2O_5-nanofibers, which exhibits broad (001) and (003)-reflections, indicative of a layer separation of d=10.1 Å. The disappearance of the (002)-peak has been reported previously for xerogels [90, 92]. Despite a long integration time, only broad and noisy features could be obtained, which can be attributed to the microcrystalline structure of the material. In addition disorder may have been introduced to originate from the drying procedure at 80°C.

Sharper features could be obtained for the L-VO_x (spectrum (2) of Figure 3.9), consistent with the higher degree of crystallinity for this material. Based on the main diffraction peaks (001)–(005), the distance of adjacent layers was found to be d=14.3 Å.

The significant difference in layer separation of the two materials can be attributed to a different water content between the bilayers. Yao et al. [89] have shown that three stable phases are present in $V_2O_5 \cdot n\ H_2O$ xerogels, which differ from each other by the water content. Phase I (n=2.6) is composed of four water layers in the channel with a V_2O_5-bilayer separation of 14.2 Å in good agreement to the boomerang-shaped material. Upon heating to 70°C the xerogel is transformed into the Iα-phase (n=1.2, d=11.6 Å), which is not observed in both samples. Phase Iβ has been obtained at 122°C and contains n=0.45 of water, the layer separation is found to be d=10.2 Å in

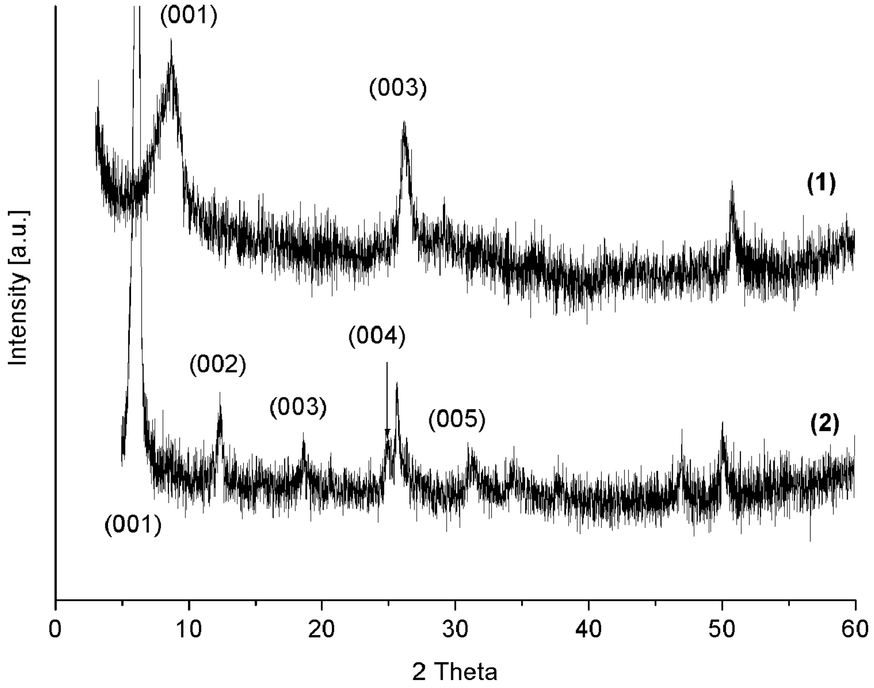

Figure 3.9: XRD spectra of (1) regular V_2O_5-nanofibers, and (2) boomerang-shaped VO_x-nanobelts.

close agreement to 10.1 Å observed for regular nanofibers.

To determine the respective structures of the layers, a combined study using Transmission Electron Microscopy (TEM) and Selected Area Electron Diffraction (SAED) was performed. For this purpose, the two materials were deposited on a polymer support (Formvar, 300 mesh, SPI Supplies), similar to V_2O_5-nanofibers on a SiO_2/Si-wafer. Figure 3.10(a) displays a network of V_2O_5-nanofibers, while Figure 3.10(c) shows an isolated VO_x-nanobelt. The presence of an additional morphology (Figure 3.10(e)) was detected within the solution of the VO_x-nanobelts. It comprises a thin VO_x-film with dimensions exceeding 10×10 μm^2. This film could not be observed by AFM, as it might have been washed away upon rinsing the wafer with water. As the contrast of the film in the TEM image is comparable to the boomerang-shaped material, its thickness is assumed to be comparable ($\sim$2.8 nm).

Figures 3.10(b), (d), (f) show the SAED patterns of the three morphologies. The [001]-diffraction pattern of an isolated L-shaped species (Figure 3.10(e)) attests the single-crystallinity within the arm of a nanobelt. This pattern is in accordance to a pattern simulation based on the model of $V_2O_5 \cdot$ n H_2O xerogel [90]. Lattice parameters a=12.55 Å and c=3.76 Å in the $C2/m$-symmetry have been used for the simulation, which are significantly larger than those reported for $V_2O_5 \cdot n$ H_2O xerogel

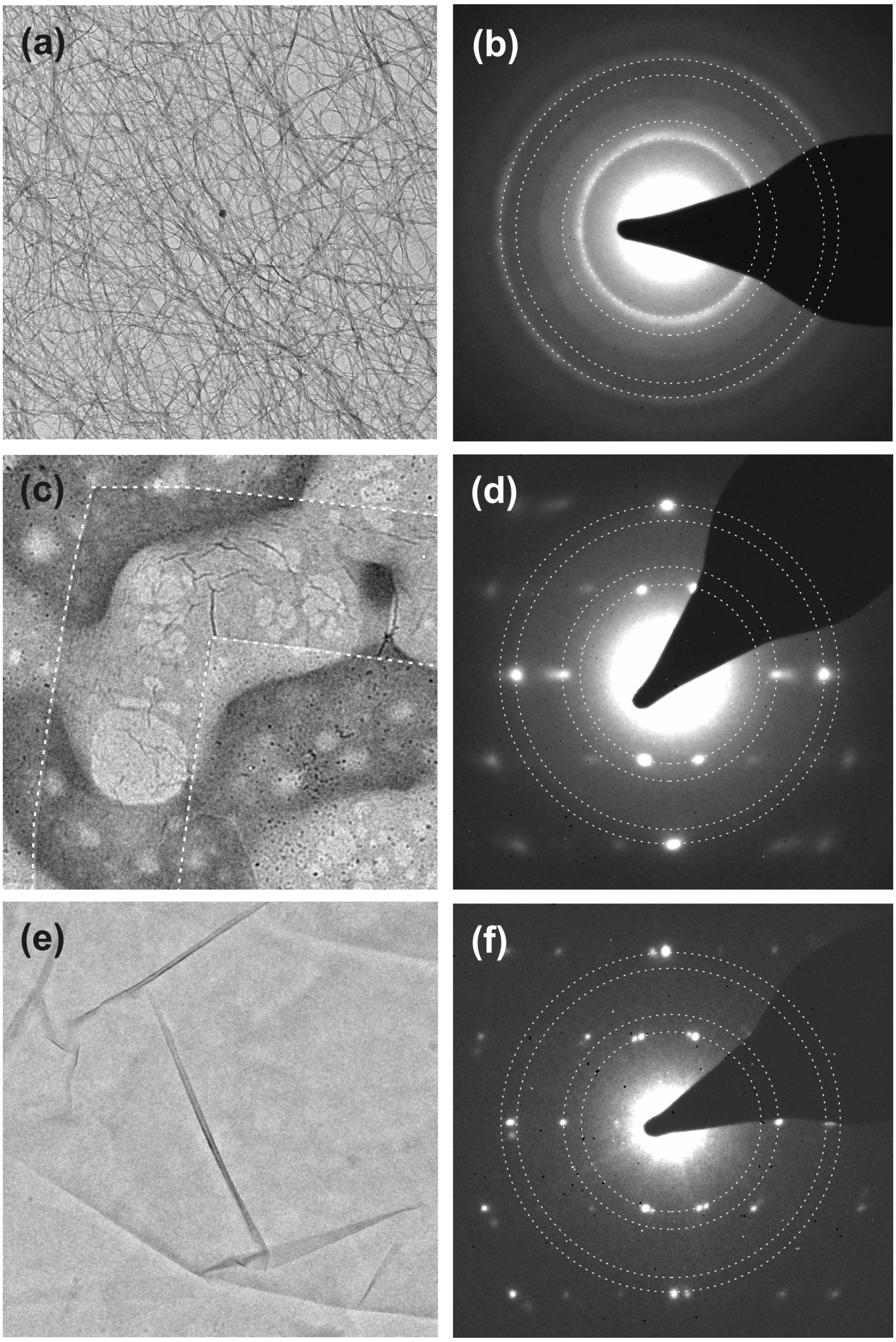

Figure 3.10: TEM images of (a) V_2O_5-nanofiber network, (c) boomerang-shaped VO_x-nanobelts and the (e) VO_x-film. The image size is 2.4 *times* 2.4 μm^2 each. (b),(d),(f) display the corresponding SAED patterns of the three materials.

(a=11.722(3) Å, c=3.570(3) Å, [90]). Since the nanofibers of Figure 3.10(a) are randomly oriented within the selected area used for the diffraction, a powder-like diffraction pattern is observed (Figure 3.10(b)). The diffraction fringes of the fibers are in accordance with the diffraction spots of the boomerang-shaped nanobelts as indicated by the dashed lines in both diffraction patterns. In addition, the diffraction pattern of the thin film (Figure 3.10(f)) closely resembles that of the single-crystalline L-shaped material. However, one observes a double spot feature, where the two spots are related to each other by a small angle of rotation ($\sim$5°). This phenomenon can be attributed to the wrinkled structure of the foil and the resulting superposition of two layers whose planes are rotated relative to each other by the specified angle. Despite their different morphology, all three species have the same crystal structure along the [001] direction, in accordance with the finding reported by Petkov et al. [90].

3.2.3 Twinning

To unravel the origin of the kinked structure, a series of SAED patterns was collected along a boomerang-shaped VO_x-nanobelt (Figure 3.11(a)). The diffraction pattern of Figure 3.11(c) has been obtained from the "center" (kink position) of the belt (marked by "c" in Figure 3.11(a)). Comparison with the diffraction patterns of the two arms (Figure 3.11(b), (d)) clearly shows that the central pattern corresponds to a superposition of the crystal orientations of the two arms. The L-shape of the VO_x nanocrystals is consequently attributed to the presence of twins. The occurrence of twins is well-documented for bulk crystals formed under natural conditions, such as the Japanese twin of quartz [104]. Since the twin domains do not superimpose in [001] orientation of real space, double diffraction is not apparent in the SAED patterns. It is evident from Figure 3.11(c) that both domains contribute separate reflections. Accordingly the twinning can be described as twinning by non-merohedry [105].

The twinning direction can be determined from the superimposed pattern of the center region. For this purpose, a high-resolution[3] SAED-pattern has been obtained from the center region of another L-VO_x-nanobelt (Figure 3.12(a)). For comparison, Figure 3.12(b) shows the simulated pattern of the central region, which is based on the model of Petkov et al. [90]. Whereas the spots of only one color (black or gray) are giving rise to the diffraction pattern of an isolated arm (as displayed in Figures 3.10(d), 3.11(b), (d)), the sum of both patterns is required to reproduce the superimposed pattern observed in the center of the kink (Figure 3.12(a)).

---

[3] The term "high-resolution" refers to the number of distinct diffraction spots, rather than to lateral resolution.

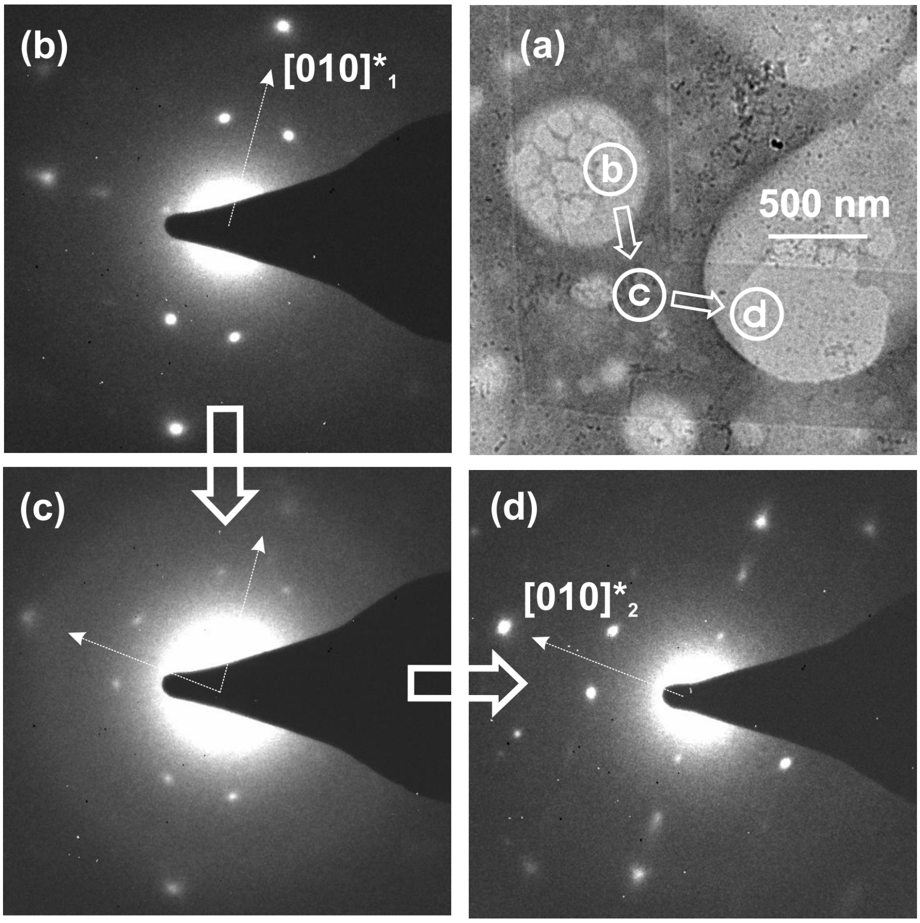

Figure 3.11: (a) TEM image of a boomerang-shaped VO_X nanobelt. (b)-(d) Series of SAED diffraction patterns along the "L", the respective position are marked in (a).

The spots along the vertical axis belong to both patterns as indicated with the two-colored circles. Therefore this direction is the twinning axis. Based on the $[010]^*{}_{1,2}$ directions, the twinning axis can be identified to be [310]* in reciprocal space, corresponding to [130] in direct space. Significant is the consistency of the angle of 84° between $[010]^*_{1,2}$ in reciprocal space obtained in the superimposed diffraction pattern of a twinned region (Figures 3.11(c), 3.12(a)) with the angle of 96° in real space, as observed in the morphology (compare Figures 3.6(a), 3.7, 3.10(c), 3.11(a)). The small deviation from rectangular twinning is also known in the bulk from numerous crystalline compounds, e.g. $TbVO_4$ [106] and V_2O_5 [107].

A precise determination of the atomistic model of the twin boundary region in real space would require high-resolution TEM images, which could not be obtained due to the rather small, homogeneous thickness of the VO_x crystals. Nonetheless, a reasonable model of the twin boundary region can be developed on the basis of the geometry of the

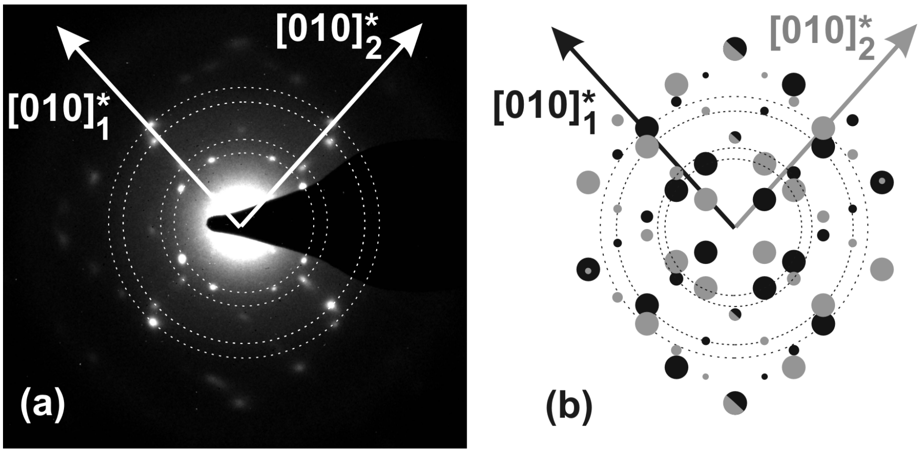

Figure 3.12: (a) SAED pattern of the center position of a boomerang-shaped VO_X nanocrystallite. (b) Simulated SAED pattern of two V_2O_5 crystals, twinned along the [310]* orientation (vertical direction).

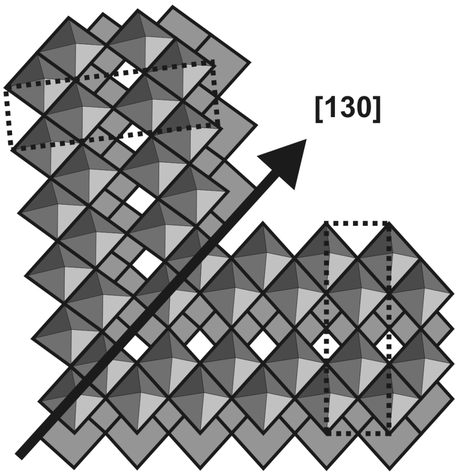

Figure 3.13: Model of the twin boundary region. The VO_5 pyramids constitute the upper layer, while the rhombi below belong to the lower layer (in which the apex of the pyramids points downward). The arrow indicates the twinning direction, while the dashed boxes reflect the unit cells of the two domains. The model resembles the observed angle of 96°.

twinning as well as the good agreement between the diffraction pattern with simulations based on literature data [89,90,92]. Within this model (Figure 3.13), the crystal consists of stacks of double layers made of joint VO_5-pyramids, as proposed by Petkov et al. [90]. The twinning occurs along the [130] direction, which leads to the observed real space angle of $\sim$96°. It is worth to note, that the slight distortion at the twin boundary was also proposed for bulk V_2O_5 [107].

3.3 Comparative characterization

So far, the different V_2O_5-nanostructures were discussed separately. In this section, the different V_2O_5-morphologies are compared to each other on the basis of Raman spectroscopy and electrical transport measurements.

3.3.1 Raman spectroscopy

Raman spectroscopy has been utilized to analyze a wide variety of V_2O_5 materials. Depending on the presence as crystal [108] or xerogel [109, 110], the crystalline perfection [111, 112], the partial reduction of the vanadium [113], the hydration level of the xerogel [109, 114, 115] or the amount of lithium intercalated into the V_2O_5-crystal [108,116,117], strong differences in the Raman spectra can be observed.

For Raman spectroscopy, ~10 μl of a diluted (1:10 H_2O), regular V_2O_5-nanofiber solution was dried on a gold covered SiO_2/Si-wafer. The Raman measurement has been performed as described in chapter 2.1.3 and the corresponding result is displayed as spectrum (1) in Figure 3.14. The vibrational features labelled (A–J) will be assigned on the basis of five spectra ((2)–(6)) obtained from the literature, which have been added to the Figure. The respective Raman spectra correspond to:

1. V_2O_5-nanofibers (this study)
2. hydrated xerogel ($V_2O_5 \cdot 1.6\ H_2O$, [109]),
3. dehydrated xerogel ($V_2O_5 \cdot 0.3\ H_2O$, [109]),
4. crystalline V_2O_5 [108],
5. crystalline V_2O_5 with oxygen deficiency [113],
6. lithium intercalated crystalline V_2O_5 (1.8 % Li, [108]).

Despite minor deviations for the hydrated xerogel, the low energy peaks in the range of 250–600 cm^{-1} are identical for regular V_2O_5-nanofibers (1), the two xerogel samples (2), (3) and crystalline V_2O_5 (4). Therefore the assignment of the literature values has been used to index the corresponding peaks (A–E). The vibrations at 275 cm^{-1} (A), 500 cm^{-1} (D), and 545 cm^{-1} (E) are assigned to the bending mode of the vanadyl oxygen δ-V–$O_{(1)}$, the bending mode of the bridging oxygen δ-V–$O_{(2)}$, and the stretching mode of the triply coordinated oxygen V–$O_{(3)}$, respectively [108,109]. No agreement has been found for the modes at 310 cm^{-1} (B) and 370 cm^{-1} (C). According to normal mode

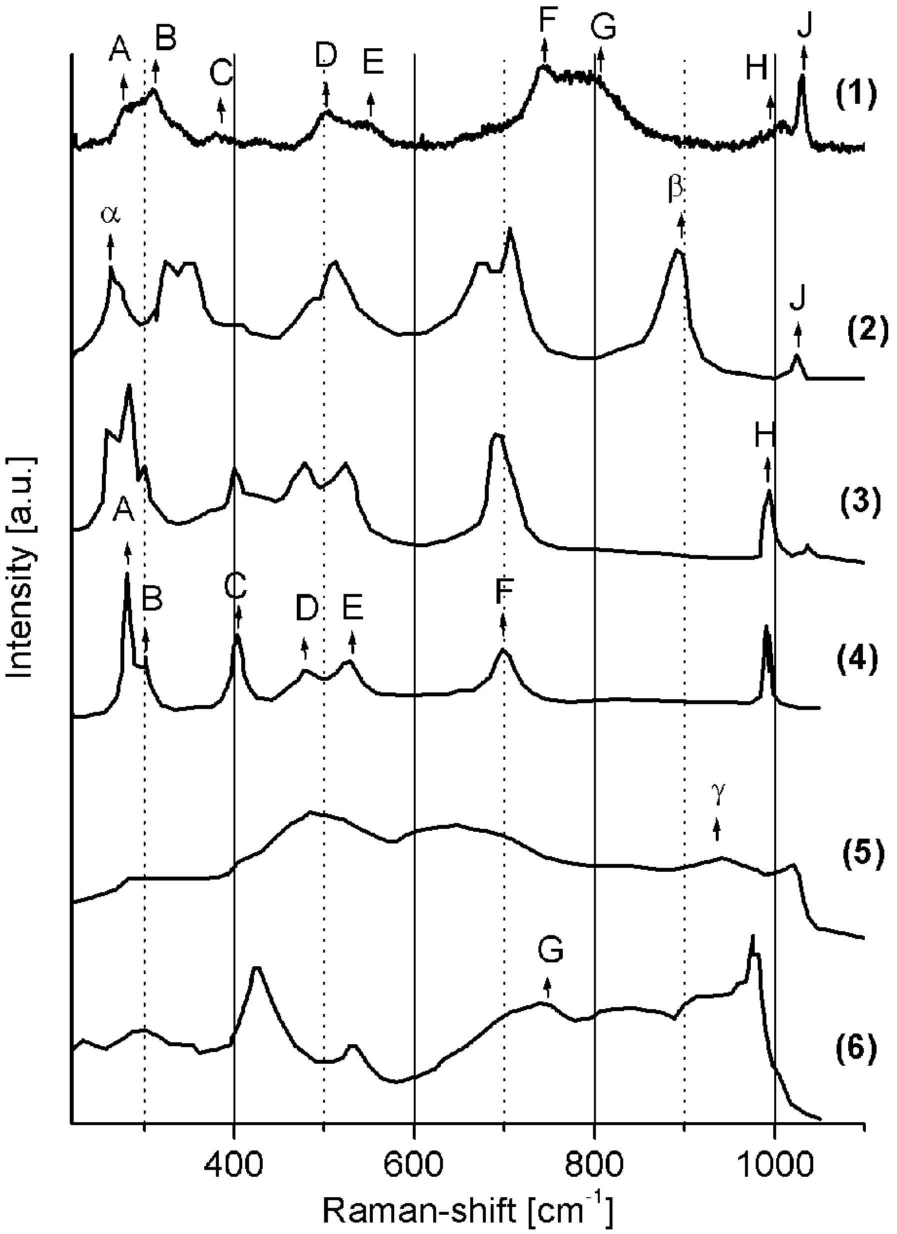

Figure 3.14: Normalized Raman spectra of different V_2O_5 materials. Spectrum (1) corresponds to the V_2O_5-nanofibers measured in this study. Spectra (2)–(6) show literature spectra and are used for the assignment of the vibrational features. See text for a detailed description of the actual material corresponding to these spectra [108, 109, 113].

calculations [110], the 310 cm^{-1}-vibration (B) may originate from a bending of the triply coordinated oxygen δ-V–$O_{(3)}$ [113] or a translational mode of the crystal R_x [108]. For peak (C) at 370 cm^{-1}, the bending mode of the double- δ-V–$O_{(2)}$ and single-coordinated δ-V–$O_{(1)}$ oxygen has been proposed in the literature [108, 113]. The additional feature at 265 cm^{-1} (labelled α) in the hydrated xerogel (spectrum (2)) has been attributed to a bending mode of the vanadyl oxygen along the long-axis of the nanofibers [109, 110], but is not present in regular V_2O_5-nanofibers (spectrum (1)).

The vibration at 745 cm^{-1} (F) is found to be up-shifted compared to the literature peaks found at 700 cm^{-1} (spectra (3), (4)), which is assigned to the stretching mode of the bridging oxygen V–$O_{(2)}$ [108, 109]. Such up-shifts of Raman frequencies have been observed in lithium intercalated V_2O_5-crystals [108]. The observed variation of peak position is attributed to a partial amorphization of the crystalline structure. Furthermore, the creation of disorder in the crystalline structure due to lithium intercalation was observed with additional modes at 736, 822, and 924 cm^{-1}, that are displayed in spectrum (6) of Figure 3.14 [108, 117]. Based on the observed shift of the V–$O_{(2)}$-vibration from 700 to 745 cm^{-1}, the broad feature at 800 cm^{-1} (G) is assigned to originate from disorder.

The stretching vibration of the vanadyl-oxygen V=$O_{(1)}$ depends strongly on the local environment of the corresponding V-atom. In crystalline V_2O_5 the vanadium-atom weekly couples to the vanadyl-oxygen $O_{(1)}$ of the adjacent V_2O_5-layer giving rise to a vibration at 995 cm^{-1} [108, 109, 113]. In xerogels and V_2O_5-nanofibers, adjacent V_2O_5-layers are separated from each other, giving rise to the double layered structure. This leads to a decoupling of the vanadyl oxygen of one layer from the vanadium-atom of the next layer. The decoupled vanadyl vibration is found at 1025 cm^{-1} [109]. The extend of this coupling depends on the amount of water incorporated in the channel. While for the dehydrated xerogel (spectrum (3)), the oxygen-coupled vanadyl vibration dominates, the hydrated sample (spectrum (2)) clearly shows the decoupled vibration. With increasing water content in the channel, an additional feature becomes visible at 895 cm^{-1} (labelled β in spectrum (2)), which has been attributed to attached water to the vanadium atoms, similar to the coupling of the adjacent vanadyl oxygen in the crystalline material [109]. It should be noted that a fourth type of vanadyl vibration has been reported in the literature. Depending on the oxygen pressure during sputter-deposition of crystalline V_2O_5-films, oxygen deficiencies can be created, which leads to the formation of V^{4+} centers [113]. Spectrum (5) of Figure 3.14 has been obtained from a sample, after sputtering at an oxygen concentration of 3 % in argon, while 10 % would have been needed to achieve a stoichiometric-perfect crystal. The vanadyl vibration has been observed to shift from 995 $\mathrm{cm}^{-1}$to 930 cm^{-1} (labelled γ in spectrum (5), [113]).

Based on the above mentioned vanadyl vibrations, the feature at 1010 cm^{-1} (H) is attributed to the oxygen-coupled vibration $O_{(1)}$- -V=$O_{(1)}$, while the peak at 1030 cm^{-1} (J) is assigned to the decoupled vibration - -V=$O_{(1)}$. The vibrations α (265 cm^{-1}), β (895 cm^{-1}), and γ (930 cm^{-1}) are absent in spectrum (1) of regular V_2O_5-nanofibers, indicating, that no reduction of the V-atoms has occurred and that only a small amount of water is present in the intermediate channel. However, the shift of the V–$O_{(2)}$ mode (745 cm^{-1}) to higher energies and the presence of the disorder mode at 800 cm^{-1} proof, that the crystal structure of regular V_2O_5-nanofibers is far from perfect. Table 3.2 summarizes the assignments of the observed peaks in regular V_2O_5-nanofibers to the literature-reported vibrations.

The Raman spectra of regular V_2O_5-nanofibers (spectrum (1)), Ag-V_2O_5-nanofibers (spectrum (2)), and boomerang-shaped VO_x-nanobelts (spectrum (3)) are displayed in Figure 3.15 for comparison. The assignment of the peaks are in accordance to the labels introduced for the regular V_2O_5-nanofibers (A–J, α–γ).

For silver-modified V_2O_5-nanofibers (spectrum (2)) an additional peak is observed at low energies (255 cm^{-1}, α). This feature is attributed to a bending mode of the vanadyl oxygen along the long axis of the nanofibers and has been observed in hydrated

Table 3.2: Assignment of Raman peaks to literature values and there respective type of vibration. For the peaks B and C, the assignment varies in the literature and both possibilities are displayed.

peak	peak-position	reported-value	vibration	reference
α		265	δ-V–$O_{(1,z)}$	[109]
A	275	280	δ-V–$O_{(1)}$	[108, 113]
B	310	300	δ-V–$O_{(3)}$, R_x	[108, 113]
C	370	405	δ-V–$O_{(1)}$, δ–V-$O_{(3)}$	[108, 113]
D	500	480	δ-V–$O_{(2)}$	[108, 113]
E	545	525	V–$O_{(3)}$	[108, 113]
F	745	700	V–$O_{(2)}$	[108, 113]
G	800	735-925	disorder	[113]
β		895	H_2O- -V^{4+}=$O_{(1)}$	[109]
γ		930	$O_{(1)}$- -V^{4+}=$O_{(1)}$	[113]
H	1010	995	$O_{(1)}$- -V^{5+}=$O_{(1)}$	[108, 109, 113]
J	1030	1025	- -V^{5+}=$O_{(1)}$	[109]

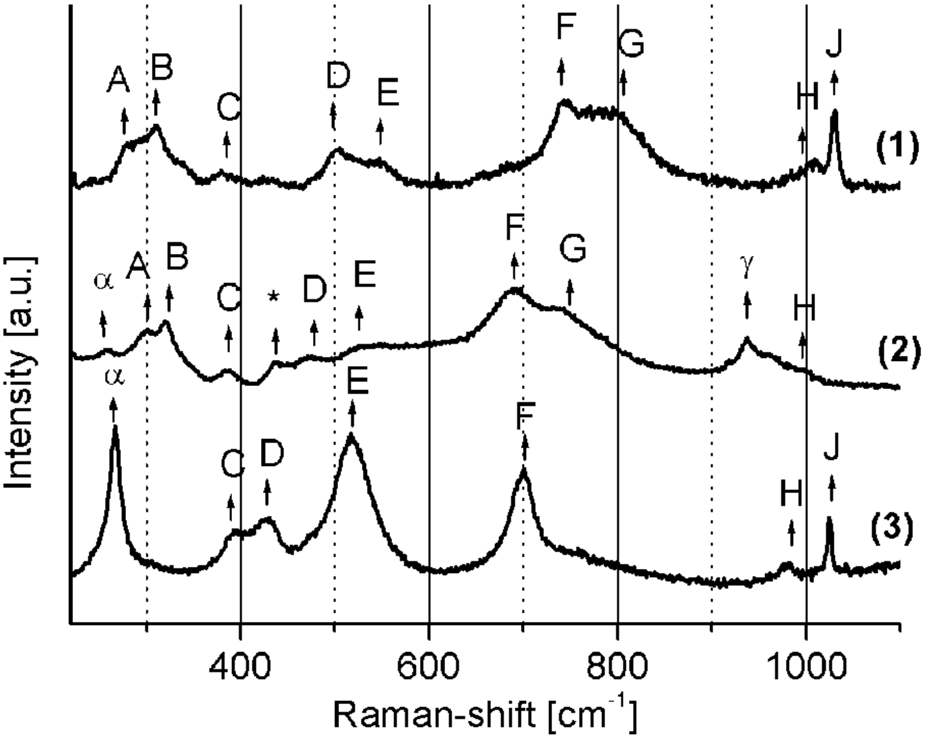

Figure 3.15: Raman-spectra of V_2O_5 materials. Spectrum (1) represents the Raman signal of regular V_2O_5-nanofibers. Ag-V_2O_5-nanofibers and boomerang-shaped VO_x-nanobelts are displayed as spectra (2) and (3), respectively.

xerogel (spectrum (2) of Figure 3.14). As a high hydration level is suggested due to the presenceof theα-peak, an addition vibration is expected at 895 cm^{-1} [109]. However, this feature is not observed in Ag-V_2O_5-nanofibers. The stretching mode of the bridging oxygen (700 cm^{-1}, F) and the disorder peak (750 cm^{-1}, G) are shifted towards lower energies, while peak G decreases in intensity compared to the regular fibers. Both effects can be attributed to an increased degree of order within the Ag-V_2O_5-nanofiber structure. Most striking is the appearance of a vibrational feature at 935 cm^{-1} (γ), which has previously been attributed to the stretching mode of the vanadyl oxygen coupled to a reduced vanadium-atom (V^{4+}=$O_{(1)}$, [113]).

The Raman spectra of the the boomerang-shaped VO_x-nanobelts (spectrum (3)) displays several differences. Whereas the low energy bending vibrations (A, B) completely vanished, the bending vibration of the vanadyl oxygen along the fiber axis (265 cm^{-1}, α) increased in intensity. Such shifts of the bending modes (A, B $\rightarrow$ α) have been observed for an increased content of water in hydrated xerogels (see spectra (2) and (3) of Figure 3.14, [109]). Moreover, the streching modes of the double- (515 cm^{-1}, E) and triple-coordinated oxygen (700 cm^{-1}, F) significantly increased in intensity. Together with the disappearance of the disorder vibration (G), this increase indicates a high degree of order within the nanobelts. Finally, the vanadyl oxygen vibrations can be observed as a double feature of oxygen-coupled (985 cm^{-1}, H) and -decoupled (1025 cm^{-1}, J) vanadium species.

3.3.2 Electrical transport properties

Due to the fact that the change of resistance is used as a measure of sensor performance, the investigation of the electrical transport properties of the pristine V_2O_5-materials is important [118, 119]. As previous studies [67, 73, 120] have shown for regular V_2O_5-nanofibers, the transport properties are dominated by variable range hopping [121], which can be described by the small polaron model proposed by Mott [122]. Hopping of electrons occurs from V^{4+} centers to V^{5+}, exchanging the valence state of the involved vanadium atoms. The V^{4+} centers are naturally present in V_2O_5 as defects within the crystal. An activation energy E_{act} has to be overcome to restore the lattice deformations caused by the polaron. The temperature dependence of conductivity can be expressed as:

$$\sigma = \frac{\nu_0 e^2 C(1-C)}{k_B T a} \exp\{-2\beta a\} \exp\left\{-\frac{E_{act}}{k_B T}\right\} = \frac{\sigma_0}{T} \exp\left\{-\frac{E_{act}}{k_B T}\right\}, \tag{3.1}$$

where ν_0 corresponds to an optical phonon frequency, C the concentration ratio $V^{4+}/(V^{4+}+V^{5+})$, a the hopping distance and β the wave-function decay. Figure 3.16(a) compares the linearized temperature dependence of the low voltage (V_{SD}=100 mV) resistance for regular V_2O_5-nanofibers (circles), silver-modified nanofibers (squares) and boomerang-shaped VO_x-nanobelts (L-VO_x, triangles). Experiments have been performed in an UHV-chamber (chapter 2.2.4) on network-samples, which are identical to structures used for gas sensing experiments (chapter 2.2.1). At high temperature a good agreement to equation (3.1) can be observed, yielding activation energies of 125 meV, 160 meV, 143 meV for regular V_2O_5, Ag-V_2O_5, and L-VO_x, respectively. These values are in agreement to 92–180 meV reported previously [67].

Variations from the straight lines in Figure 3.16(a) have been discussed in the frame work of disorder within the system, that originates from the crystalline imperfection and the random distribution of fibers/nanobelts within the network [67, 120, 123]. The activation energy E_{act} is composed of the energy required for hopping E_{hopp} and an disorder energy E_{dis}. At high temperatures the activation energy is found to be $E_{hopp} + \frac{1}{2}E_{dis}$, while it reduces to $\frac{1}{2}E_{dis}$ at lower temperatures [73, 120, 123].

The dimensionality d of the system can be determined within the variable range hopping approximation. Dependencies on dimensionality are triggered by the average

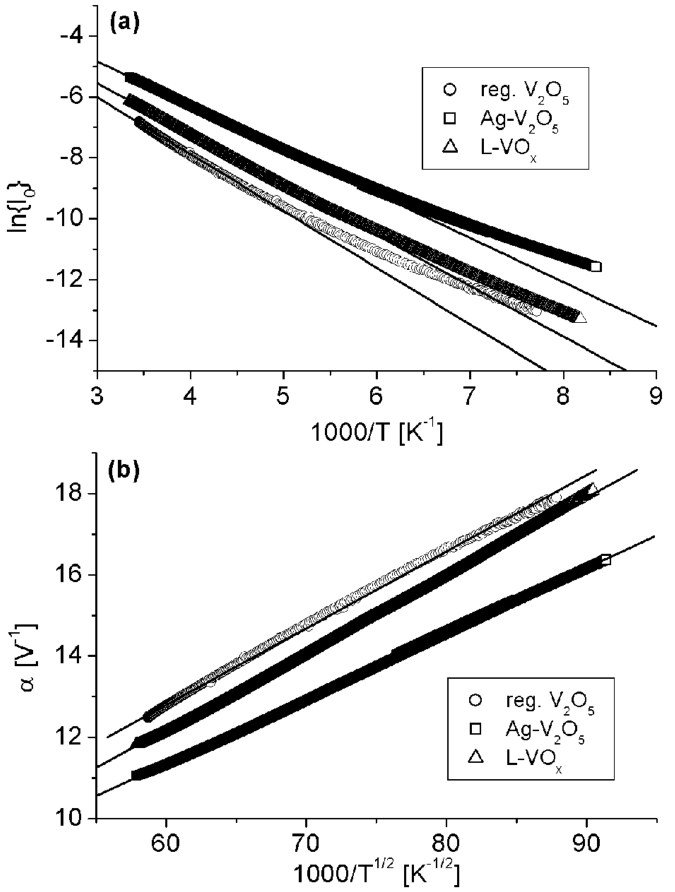

Figure 3.16: (a) Linearized temperature dependence of resistivity for regular V_2O_5, Ag-V_2O_5, and boomerang-shaped VO_x-nanobelts (L-VO_x). (b) Validation of one-dimensional conductance within the three materials.

hopping distance a, as a polaron tries to find a neighbor, that is in close proximity both laterally and energetically. Upon reducing the dimensionality the number of neighbors decreased, giving rise to a temperature dependency of conductivity given by:

$$\sigma(T) = \sigma_0 \exp\left\{-\left(\frac{T_0}{T}\right)^{\frac{1}{d+1}}\right\}. \tag{3.2}$$

The best fit could be obtained for d=1 (Figure 3.16(b)), from which characteristic temperatures T_0 of 35,600 K, 25,700 K, and 36,100 K are calculated for regular fibers, Ag-V_2O_5, and L-VO_x, respectively. While the one-dimensional characteristic of electrical transport was expected for the two type of V_2O_5-nanofibers, it is remarkable, that the transport property of nanobelts with width of ~500 nm have the same dependence. Similar effects have been observed in crystalline V_2O_5 [124,125], and can be attributed to the structure of the material. Transport perpendicular to the V_2O_5-layers occurs along V-$O_{(1)}$-V in crystalline V_2O_5 (see Figure 3.1) and is strongly suppressed due to

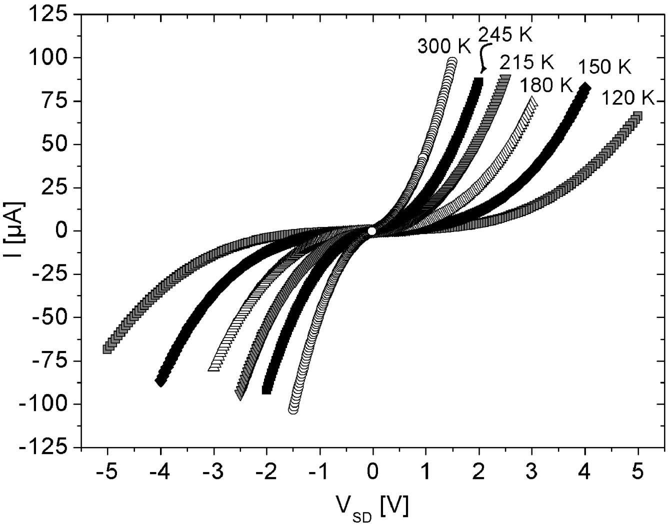

Figure 3.17: I-V characteristic of Ag-V_2O_5-nanofibers as a function of temperature.

the weak binding between adjacent layers. In xerogels/nanofibers, transport is hindered due to the presence of a water channel between two V_2O_5-bilayers. Transport within the V_2O_5-layers, but perpendicular to the long axis, follows V-V'-$O_{(2)}$-V'-V and is limited by the bridging oxygen $O_{(2)}$. Only along the fiber direction the transport does not involve oxygen-atoms, as the current can pass along V-V'-V in a zigzag-like manner. Therefore the one-dimensional transport properties observed in the three materials are not dominated by the morphology, but rather by the crystal-structure, which is similar for all three species.

The small separation of the electrodes (L=10 μm) allows for applying high electric fields exceeding 10^5 V/m. This has a strong influence on the conductivity, as the external electric field modulates the profile of the potential barriers and opens up new accessible hopping centers. The current as a function of voltage can be described by:

$$j = \frac{en\nu_0}{\pi} \exp\left\{-\frac{E_{act}}{k_B T}\right\} \sinh\left\{\frac{eV_{SD}}{2k_B T}\frac{a}{L}\right\} = I_0 \sinh\left\{\alpha V_{SD}\right\}, \tag{3.3}$$

where n is the carrier concentration, and L reflects the channel length. The effect of high electric fields at various temperatures is presented in Figure 3.17 for the silver-doped V_2O_5-nanofibers. Similar dependencies of conductance on voltage and temperature have been found for regular V_2O_5-fibers and boomerang-shaped VO_x-nanobelts.

The I-V characteristics of the three materials have been analyzed at all measured temperatures according to equation (3.3). Special care has to be taken on the voltage range used for the fitting procedure. This range has been fixed for each material. The temperature dependence of the pre-exponential factor I_0 is dominated by the exponential

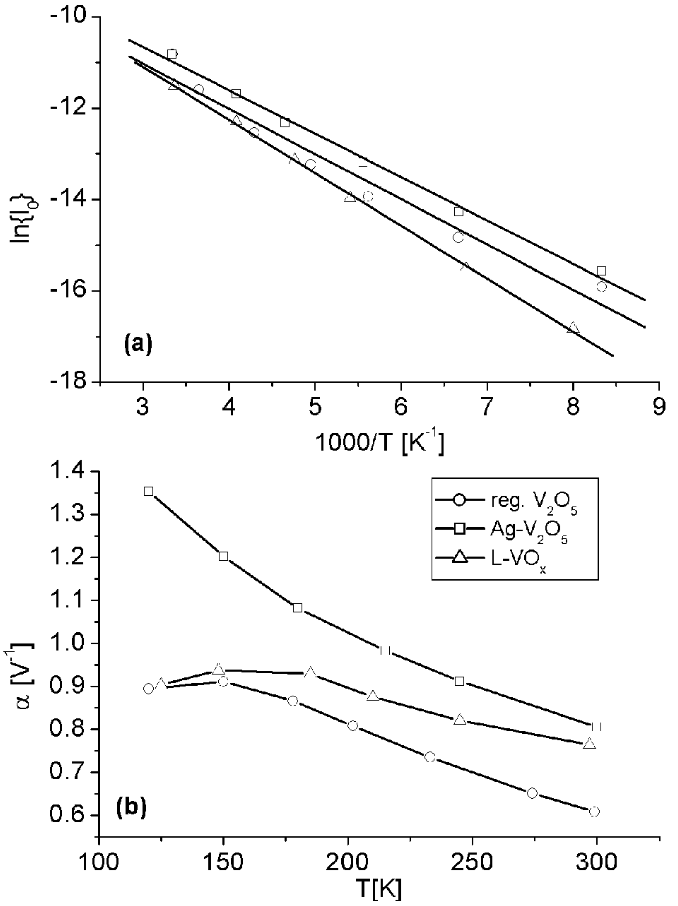

Figure 3.18: Temperature dependence of (a) the pre-exponential factor I_0 and (b) the exponential factor α for regular nanofibers (circles), Ag-V_2O_5 (squares), and boomerang-shaped VO_x-nanobelts (triangles). The solid lines in (a) are linear fits to the data, while the lines in (b) are added as guide to the eye.

term including the activation energy. Therefore, a plot $\ln\{I_0\}$ vs. T^{-1} shows a linear relation (Figure 3.18(a)), providing respective activation energies of 86 meV, 84 meV, and 98 meV for the regular nanofibers, Ag-V_2O_5, and boomerang-shaped VO_x-nanobelts. Compared to the results obtained from the analysis of the measured resistances, the activation energies are lowered. The origin of this variation remains unclear at the present stage, but the contact resistance at the fiber-electrode interface may be one explanation.

The average hopping distance a increases with temperature ($a \propto T^{d/(d+1)}$). As the hopping distance is included in the exponential factor, only a weak dependence on temperature is observed for the exponential factor α (Figure 3.18(b)). A decrease of α has been obtained with increasing temperature, in accordance to the theory. Towards lower temperature, deviations from this behavior can be observed, which are attributed to the shift in activation energy, as discussed above in the frame-work of disorder.

Chapter 4

Gas sensors based on V_2O_5-nanofibers

The electrical response of V_2O_5-nanofibers to ammonia (NH_3) is presented in chapter 4.1, where the Langmuir adsorption isotherm will be introduced as a simple, yet powerful theory.

The detection of organic amines, such as butylamine, is an important task, since amines are present in rotten food. Sensors sensitive to this vapors have therefore a high impact for food freshness monitoring. Chapter 4.2 describes the sensitivity of V_2O_5-nanofibers to butylamine vapors. By investigating devices with different electrode geometry, the interaction centers, which are responsible for the observed change in resistance, could be identified.

Modifying the V_2O_5-nanofibers with palladium enables a high sensitivity to hydrogen with responses exceeding 100,000 % at room temperature (chapter 4.3). To unravel the origin of this tremendous response, experiments with atomic hydrogen have been performed in an UHV environment. Temperature dependent transport measurements have been used to elucidate the electronic nature of this effect. In addition, Raman spectroscopy has been used to monitor structural changes upon exposure to hydrogen.

4.1 Ammonia sensor

Chemical sensing experiments have been performed with networks of V_2O_5-nanofibers deposited on interdigitated electrode structures. These samples exhibited a base resistance of ∼10 kΩ. See chapters 2.2.1 and 2.2.3 for experimental details. Figure 4.1(a) shows a typical atomic force microscopy (AFM) image of these networks, whereas Figure 4.1(b) displays a network, which was modified by evaporation of gold to a nominal thickness of 1 nm.

Figure 4.2(a) shows the response $\Delta R/R_{ini}$ (change of resistance ΔR, normalized to initial resistance R_{ini}) of an unmodified V_2O_5 network, upon exposure to various concentrations of ammonia. The response traces comprise three regimes: (i) an equilibration time (0–1 min), (ii) an exposure phase (1–3 min), and (iii) a recovery period (3–8 min). A fast resistance drop within a period of ∼1 min is observed, and for recovery less than 5 min are required. The observed resistance decrease is in accordance with the known electron donor property of ammonia and the n-type semiconducting behavior of V_2O_5 [67].

It was found that evaporation of gold improves the performance of the sensors. For this purpose, nominally 1 nm of gold has been evaporated onto the same network, which resulted in clusters showing a wide variation of diameters, as can be seen in the AFM image of Figure 4.1(b). The discontinuity of the evaporated gold excludes an electrical short-circuit of the V_2O_5-network. This conclusion is supported by a small increase of network resistance after modification. The response of the sensor has been measured prior and after the modification to various concentrations of ammonia (Figure 4.2(b)),

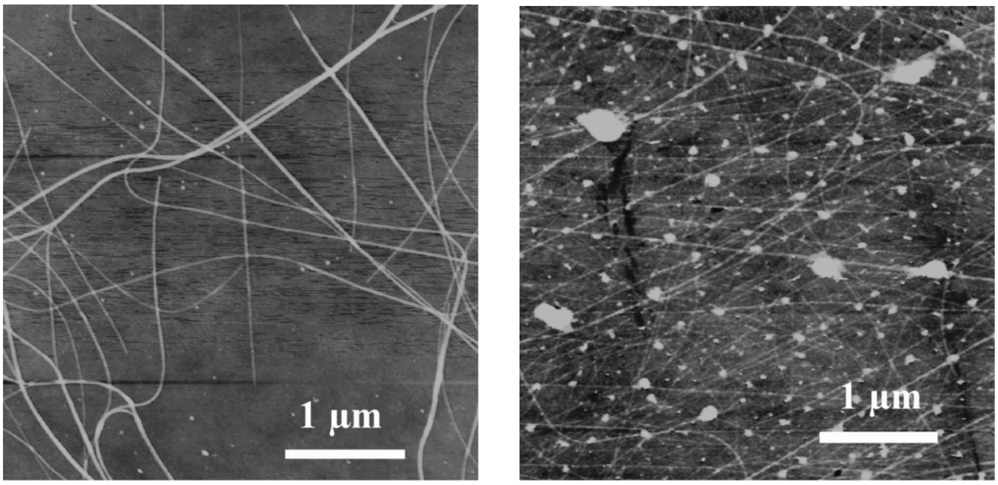

Figure 4.1: Atomic Force Microscopy image of (a) unmodified and (b) with nominally 1 nm gold modified V_2O_5-network deposited on SiO_2/Si-wafers [126].

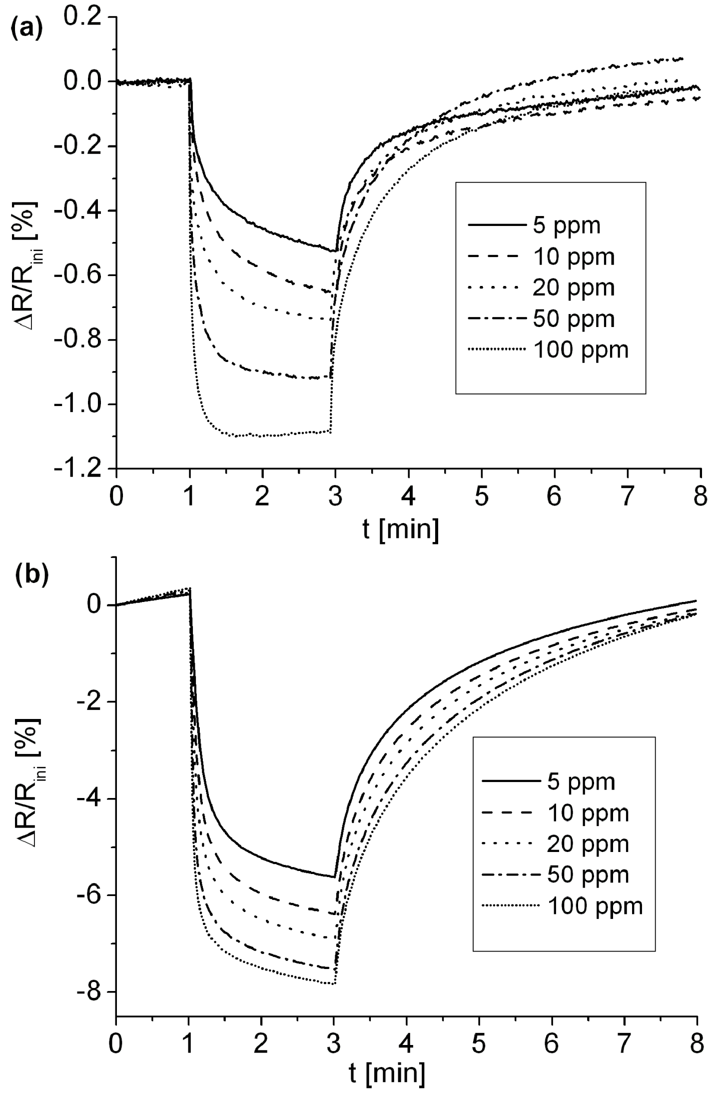

Figure 4.2: Response of an unmodified (a) and with 1 nm gold modified (b) V_2O_5 sensor to various concentrations of ammonia [126]. Note the different scale of the vertical axis.

revealing an increase in sensitivity by a factor of seven (against 100 ppm NH_3).

4.1.1 Langmuir isotherm and time-evolution of responses

To shine more light onto the gas-nanofiber interactions, the sensor response has been analyzed in terms of coverage θ ($0 \leq \theta \leq 1$) of the sensor material. The sensor response $\Delta R/R_{ini}$ is related to the coverage θ via proportionality:

$$\Delta R/R_{ini} = \Delta R_{\infty} \cdot \theta, \tag{4.1}$$

where ΔR_∞ is the change of resistance at maximum coverage ($\theta = 1$). The adsorption kinetics, which describes the coverage as a function of gas concentration c, has been frequently described with the Langmuir adsorption isotherm [84, 127, 128]. This theory contains only very little constraints on the experimental conditions, as follows:

1. The gas molecules neither interact in the gas phase nor on the surface with each other (individual particles).
2. The number of free sites on the surface is limited. It reaches a maximum coverage θ of 1 (monolayer coverage).
3. The adsorption rate is proportional to the gas concentration c and the number of free sites $(1 - \theta)$. The proportionality is assured with the adsorption rate constant k_{ads}.
4. The desorption rate is proportional to the coverage θ with the corresponding constant k_{des}.

Following these assumptions, the time-dependence of coverage can be formulated as:

$$\frac{d\theta}{dt} = \underbrace{k_{ads} \cdot c \cdot (1 - \theta)}_{adsorption} - \underbrace{k_{des} \cdot \theta}_{desorption} . \tag{4.2}$$

In equilibrium ($t \to \infty$), the ad- and desorption rates become equal and the time-derivative (equation (4.2)) vanishes, giving rise to a concentration dependent coverage θ_c[1]:

$$\theta_c = \frac{k_{ads} \cdot c}{k_{ads} \cdot c + k_{des}}. \tag{4.3}$$

This is the well-known Langmuir isotherm. Defining $K = k_{ads}/k_{des}$ as ratio of transition rates, which can be inserted in equation (4.3):

$$\theta_c = \frac{K \cdot c}{1 + K \cdot c}. \tag{4.4}$$

The plot in Figure 4.3(a) demonstrates a reasonable agreement between the experimental results (symbols) and the Langmuir fits (lines), for both undoped (triangles) and gold modified (squares) V_2O_5 sensors. The quality of the fit can be judged best from the linearized form of equation (4.4), as displayed in Figure 4.3(b). The fitting parameters are given in Table 4.1, reflecting the increased sensitivity of the modified sensor compared to the unmodified one. Deviations from ideal Langmuir adsorption behavior are discussed below.

---

[1] The index c indicates saturation at a given concentration c

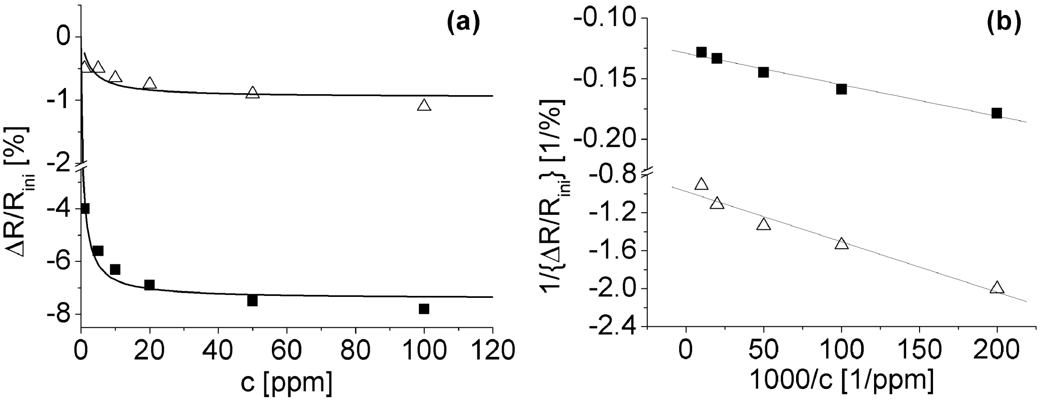

Figure 4.3: (a) Response of unmodified (triangles) and modified (squares) V_2O_5 network as a function of ammonia concentration. The solid lines correspond to the Langmuir fits [126]. (b) Linearized plot of the same data.

Table 4.1: Fitting parameters of the Langmuir isotherm and the time-evolution analysis, applied to the unmodified and with 1 nm gold modified V_2O_5-network exposed to NH_3.

		unmodified	1 nm gold modified
Langmuir	ΔR_∞	-1.0 %	-7.7 %
	K	0.18 ppm^{-1}	0.50 ppm^{-1}
time evolution	k_{ads}	0.0019 (ppm·s)$^{-1}$	0.0011 (ppm·s)$^{-1}$
	k_{des}	0.022 s^{-1}	0.011 s^{-1}
	K	0.09 ppm^{-1}	0.10 ppm^{-1}

Equation (4.2) can be explicitly solved for all times, using the ansatz:

$$\theta_{exp}(t) = \theta_c \cdot [1 - \exp\{-t/\tau_{exp}\}] \,, \tag{4.5}$$

where θ_c is defined as in equation (4.3) and τ_{exp} is a characteristic time corresponding to the exposure[2], which depends on the concentration c. Figure 4.4 shows the exponential fit of the response curve for the example of exposure to 100 ppm NH_3 on the unmodified sample. Inserting equation (4.5) in equation (4.2) yields:

---

[2] The terms "exposure" and "recovery" are used as macroscopic variables, which correspond to the conditions, when the test gas is switched on or off. The terms "adsorption" and "desorption" correspond to microscopic variables, which describe the ad- and desorption of a single gas molecule to the surface. Note, that during exposure both ad- and desorption take place, while during recovery only desorption can occur.

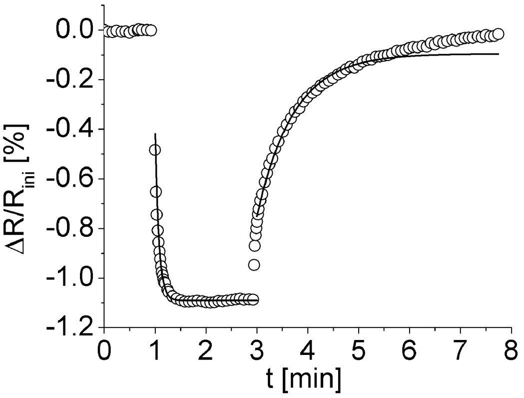

Figure 4.4: The response trace of the unmodified V_2O_5-sensor exposed to 100 ppm NH_3 (open circles), fitted to equation (4.5) during exposure (1–3 min) and to equation (4.7) during recovery (3–8 min). The distance of data points has been adjusted to achieve a equidistant separation of neighboring points.

$$\frac{1}{\tau_{exp}} = k_{ads} \cdot c + k_{des}, \tag{4.6}$$

which connects the macroscopic and experimentally accessible variable τ_{exp} to the microscopic variables k_{ads}, k_{des}. Fits like in Figure 4.4 have been performed for all concentrations on both the unmodified and the gold-modified sample. $1/\tau_{exp}$ is plotted as a function of gas concentration c in Figures 4.5 for the unmodified ((a), open triangles) and the modified ((b), filled squares) V_2O_5-network. In both cases, a linear dependence can be observed in accordance to equation (4.6)

Similarly, the recovery can be described as a function of time. Equation (4.2) can in this case be simplified ($c = 0$). The time dependence follows a simple decay of occupied states:

$$\theta_{rec}(t) = \theta'_c \cdot \exp\{-t/\tau_{rec}\}, \tag{4.7}$$

where τ_{rec} is a characteristic time for recovery and θ'_c equals θ_c when saturation is reached during exposure, otherwise θ'_c represents the coverage when the gas was switched off. Combining equation (4.7) with the modified ($c = 0$) equation (4.2) yields again a relation between macroscopic and microscopic variables:

$$\frac{1}{\tau_{rec}} = k_{des}. \tag{4.8}$$

Apparently, the characteristic time τ_{rec} does not depend on the gas concentration and the actual coverage. The exponential function of equation (4.7) has been applied to both types of samples and at all ammonia concentrations. Figure 4.4 exemplifies a fit

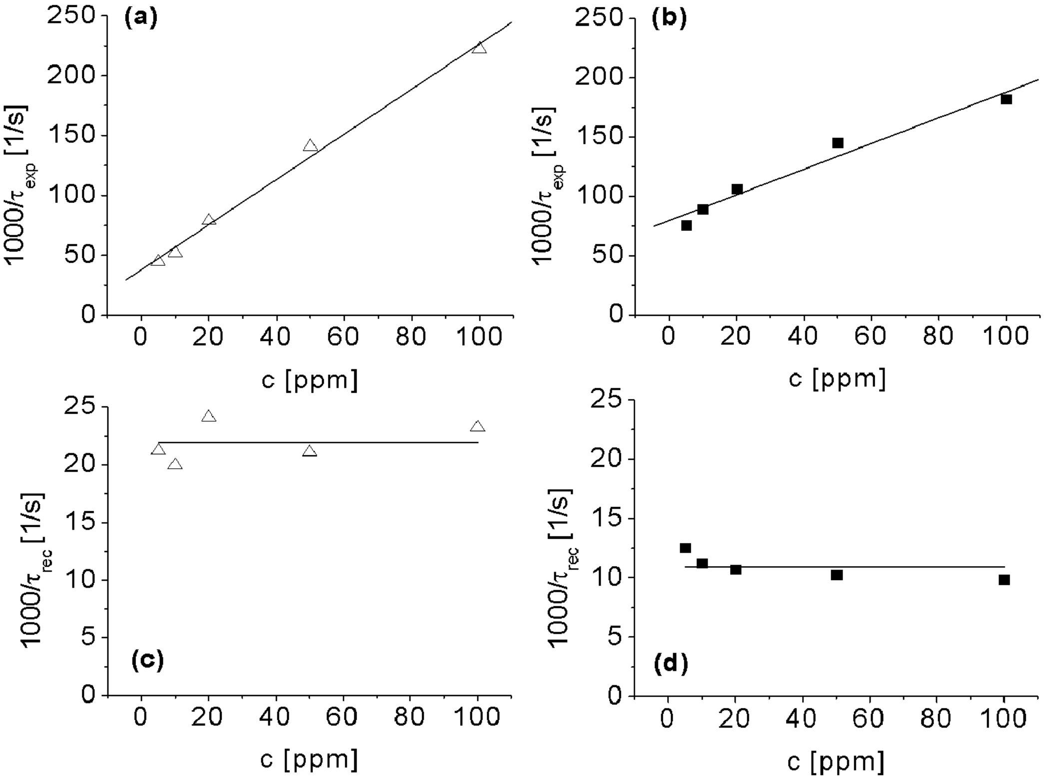

Figure 4.5: (a),(b) $1/\tau_{exp}$ vs. c and (c),(d) $1/\tau_{rec}$ vs. c for the unmodified (open triangles (a),(c)) and with 1 nm gold modified (closed squares (b),(d)) V_2O_5-networks, when exposed to NH_3.

to the recovery trace for the case of 100 ppm NH_3 applied to the unmodified sample. The inverse of the characteristic time τ_{rec} as a function of gas concentration c is plotted in Figures 4.5(c), (d) for the unmodified and the modified sample, respectively. Almost constant values are obtained in accordance to equation (4.8). The fitting parameters as obtained from the time evolution analysis for both samples have been added to Table 4.1. The transition rates k_{ads} and k_{des} can be combined to yield the respective ratio K, which can be compared to the evaluation of sensor response via Langmuir isotherm.

The values for the ratio K depend on whether they are derived from Langmuir isotherms or via the analysis of time-dependence. This discrepancy, as well as the deviation from ideal Langmuir behavior, can be attributed to the finite exposure time of 2 min. During exposure, the sensor response did not reach its equilibrium (see Figure 4.2). This is true especially for the lower ammonia concentrations. Additional deviations arise from fitting the time evolution with a simple exponential function. The imperfect fit can be explained by the presence of different adsorption sites, such as the electrode-fiber contact, on the fiber or on fiber-fiber interconnects.

Nonetheless the overall sensor performance can be well described with Langmuir theory and the corresponding time dependence. Therefore it can be concluded that although different adsorption sites seem to be present, their respective ad- and desorption properties show almost identical behavior, e.g. in terms of binding energy. Furthermore, the only moderate response (~7 %) ensured the required proportionality of coverage and sensor response. A variation in conductance due to the presence of ammonia can be treated as small perturbation to the overall conductivity.

From Table 4.1 it is evident, that the desorption rate constant (k_{des}) is reduced in the 1 nm gold modified sample (0.011 s^{-1}) compared to the unmodified one (0.022 s^{-1}). This effect can be illustrated with the time t_{90} needed to achieve 90 % recovery, which increases from 100 s for the unmodified sensor to 180 s for the gold modified sample after an exposure to 100 ppm ammonia (see Figure 4.2). Both, the increased response and the slower recovery indicate a stronger interaction of ammonia with the gold-nanoparticle/V_2O_5-system, compared to the non-modified sample.

A more detailed understanding of the fundamental processes involved in the ad- and desorption from ammonia on the V_2O_5-nanofibers would require a variation of temperature during the sensor experiments. Due to technical limitations with the teflon cell, this type of experiments could not be made. A comparison of the V_2O_5-nanofibers to other ammonia sensors presented in the literature will be given in the conclusion at the end of this thesis.

4.2 Butylamine sensor

In the above described experiments with ammonia, the analyte gas was diluted with nitrogen to minimize parasitic effects associated with the presence of oxygen. However, such dilution conditions do not represent a real world environment. By comparison, detection of butylamine ($C_4H_9NH_2$), represented in this chapter, is a model system much closer to these conditions. Experiments have been performed in cooperation with the Materials Science Laboratories of Sony International (Europe) GmbH. In order to simulate ambient conditions, butylamine has been diluted with dry air instead of nitrogen, and relative humidity has been added to the test gas.

The detection of butylamine is of interest for technical applications, due to its presence in rotten food. Butylamine sensors may find application as quality control for food freshness [129,130]. Medical diagnosis is another application field for this type of sensor, since butylamine has been observed in patients with uremia (kidney failure) [131] and various types of cancer [131,132].

Like for the preparation of the ammonia sensors (chapter 4.1), V_2O_5-fiber networks have been deposited onto interdigitated electrodes (50 electrode pairs, separation 10 μm, 1800 μm overlap) via dip-coating[3]. A voltage on the order of 100 mV has been applied across the 10 μm electrode gap. See chapters 2.2.1 and 2.2.3 for technical details.

To simulate typical ambient conditions, the relative humidity has been adjusted to 40 %. Butylamine concentrations ranging from 150 ppb to 9.5 ppm have been used as a test vapor. The V_2O_5-sensor has been exposed for 5 min to the test vapor, Figure 4.6 shows the room temperature response of a V_2O_5-network. A steep increase in resistance could be observed reaching values exceeding 500 %. While the large response is favorable for technical applications, it should be noted that no saturation of the sensor signal has been observed after exposure for 5 min. Recovery of the sensor is reached within ~10 min, without requiring elevated temperature or UV-irradiation. The limit of detection has been tested at a butylamine concentration of 30 ppb, and the corresponding trace is displayed in the inset of Figure 4.6. An easy detectable signal of 10 % has been obtained, demonstrating that the limit of detection (LOD) lies below 30 ppb of butylamine. Strikingly, this sensitivity exceeds even the human olfactory system, which requires at least 240 ppb of the vapor to be recognized [133].

Similar to the ammonia sensor (chapter 4.1), the response of the sensor after 5 min of exposure can be displayed as a function of butylamine concentration (Figure 4.7). In

---

[3] It should be noted, that 3-aminopropyldimethylethoxysilane (ABCR, Germany) has been used instead of N-[3-(trimethoxysilyl)propyl]ethylenediamine as linker-molecules between the substrate and the fibers. 50 μl of this solution have been diluted in 5 ml toluene at 60°C.

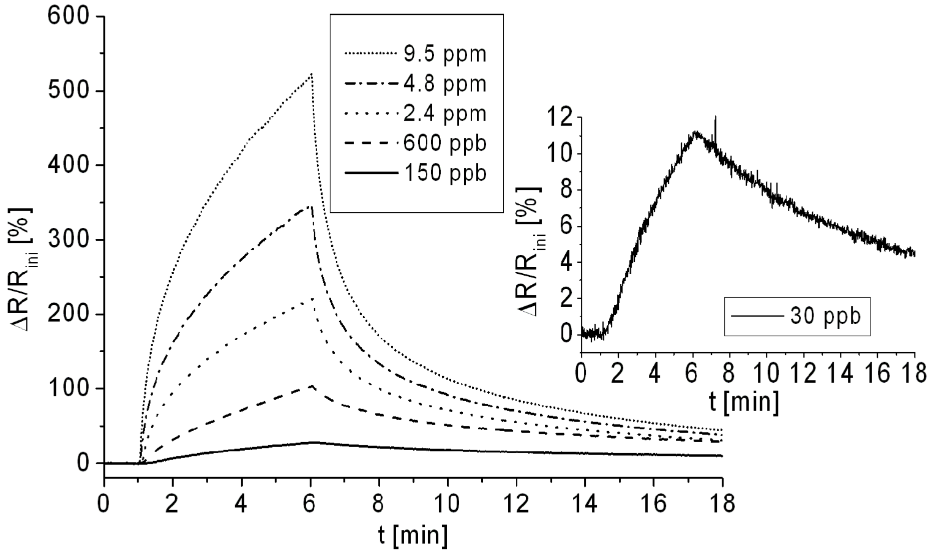

Figure 4.6: Response of a V_2O_5 network when exposed to various concentrations of butylamine. The relative humidity has been adjusted to 40 % to simulate ambient conditions. (inset) Response of the same sensor, when exposed to 30 ppb of butylamine at 40 %rh.

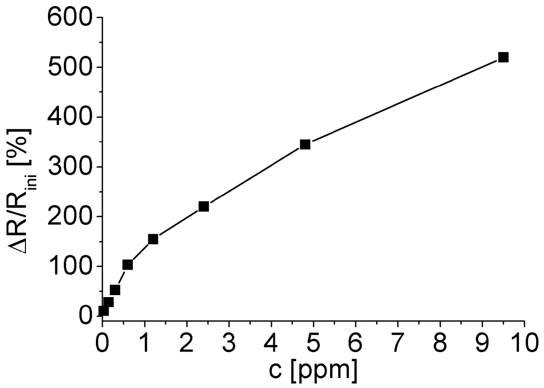

Figure 4.7: Response after 5 min as a function of butylamine concentration. The relative humidity of the test vapor has been adjusted to 40 %.

this plot the lines between experimental data points are only drawn for clarity. They do not represent Langmuir isotherms, as in the case of the V_2O_5-sensors detecting ammonia (chapter 4.1). The Langmuir theory can not be used for the butylamine sensor, as it applies only to the equilibrium response at a given concentration, which has not been reached after the 5 min exposure. The dynamic range, in which the gas concentration can be identified by its respective sensor response, spans two order of magnitude (30 ppb–9.5 ppm).

The effect of relative humidity and selectivity has been studied in detail by our

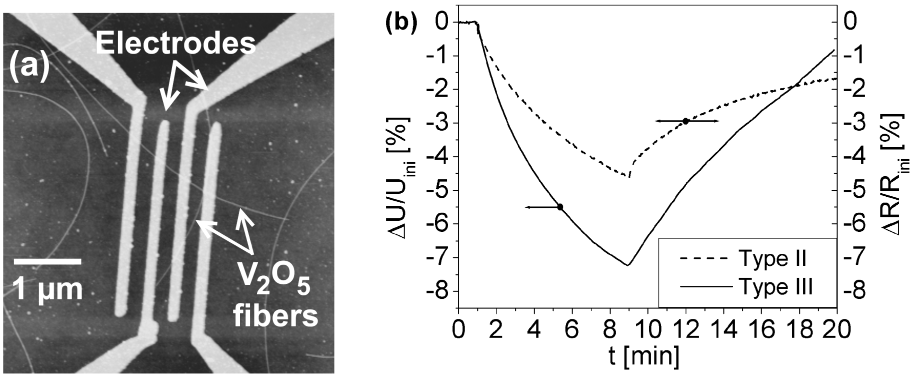

Figure 4.8: (a) Atomic force microscopy image of two isolated V_2O_5-fiber contacted with electrodes on top (type III). (b) Sensor response of this sensor (type III), when exposed to 9.5 ppm butylamine at 40 %rh (solid line). The dashed line correspond to a network sample, where the electrodes have been deposited on top of the electrodes (type II). The butylamine concentration has been adjusted to 240 ppm, while the relative humidity was set to 40 %.

cooperation partner I. Raible [59, 134] at Sony. The results can be summarized as follows: (i) The sensor response to butylamine increases with relative humidity, which is remarkably, as in many cases water poisons the sensor, which leads to a decreasing response with increasing humidity. (ii) The device shows good responses to various amines, while being insensitive to propanol and toluene.

4.2.1 Interaction centers

As the results on a V_2O_5-network sample deposited on top of interdigitated electrodes (in the following denoted as sensor type I) showed good responses to exposures with butylamine at finite relative humidities, it has been attempted to reduce the size of the sensor to an isolated fiber. For this purpose, a diluted network of fibers has been deposited on a SiO_2/Si-wafer and electrodes with a separation of 150 nm have been deposited on top with the aid of electron-beam lithography. The new type of sensor (type III[4]) is displayed in Figure 4.8(a). The AFM image shows that only two fibers are employed for the actual gas sensing.

In order to achieve a sufficient signal-to-noise ratio, the initial bias voltage[5] was increased to ∼3V applied between the two middle electrodes (Figure 4.8(a)). At this

---

[4] Type II will be introduced at a later time. For reasons, that become evident below, it is useful to denote the sensor based on an isolated fiber as type III

[5] The experiment is performed in constant current mode, therefore the current was adjusted in order to give an initial voltage of 3V.

increased voltage, the sensor device no longer showed ohmic behavior (see chapter 3.3.2 for details), therefore the sensor response can not be described as $\Delta R/R_{ini}$, but rather as $\Delta U/U_{ini}$. For samples showing ohmic behavior, both expressions are equivalent, as the measurements have been performed in the constant current mode. The solid line in Figure 4.8(b) shows the sensor response of the two fiber device, when exposed to 9.5 ppm of butylamine at 40 %rh. Most strikingly, the sign of the response inverses compared to the network sample (type I). Moreover, it can be seen that the absolute value of sensor response based on isolated fibers is an order of magnitude smaller compared to that of the network sample.

To gain insight into the origin of the reversed response, a third type of sensor (type II) has been investigated. It consists of an interdigitated electrode array with an electrode separation of 5 μm, an overlap of 900 μm and 50 electrodes. Different from the sensors of type I, the electrodes have been deposited on top of the V_2O_5-network. Therefore, the sensors of type II are intermediate between type I and type III in the sense that, while sensor type I and II are composed of fiber networks, type III represents isolated fibers. Type II and III have in common, that the electrodes have been deposited on top of the fibers, while for the sensor of type I the electrodes have been deposited underneath the fibers. The sensor response to 240 ppm butylamine of sensor type II has been added to Figure 4.8(b) as dashed line. The response of the type II sensor is similar to the sensor composed of an isolated fiber, although the concentration has been increased by a factor of ~25, to give a sufficient response. A summary of the different types of sensor configurations together with the sensor responses is given in Table 4.2.

The responses obtained for different sensor configurations can be explained in terms of various interaction centers, to which the vapor molecules bind. Three centers are

Table 4.2: Responses of three types of V_2O_5-sensors to various concentrations of butylamine for the different contact configurations displayed in Figure 4.9. The term “configuration” implies the arrangement of fibers relative to the electrodes. Depending on the geometry of the sensor, different interaction centers are accessible or hindered for the gas: the fibers themselves (A), the fiber-fiber junctions (B) and the interface between fiber and electrode (C).

type	density	configuration	concentration	response	interaction
I	network	on top	9.5 ppm	+520 %	A, B, C
II	network	below	240 ppm	-4 %	A, B
III	individual	below	9.5 ppm	-7 %	A

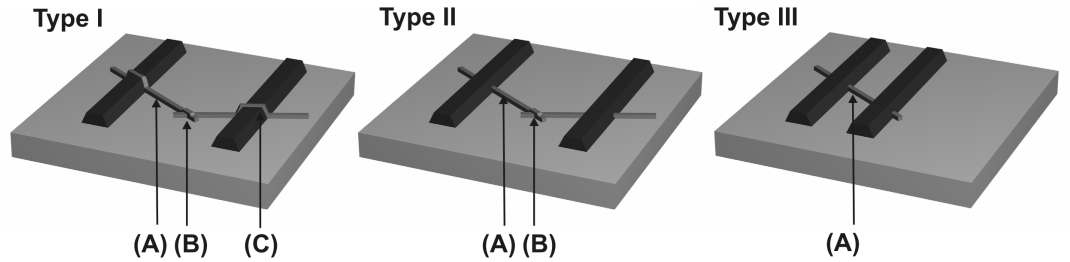

Figure 4.9: Schematic representation of the three sensor geometries together with the accessible interaction centers. The interaction centers are: (A) the fibers themselves, (B) the fiber-fiber interface, (C) the fiber-electrode contact. Note, that the graphs are not drawn to scale.

possible:

- the molecules can directly interact with the fibers (site A).
- the molecules can adsorb at the fiber-fiber interconnects (site B).
- the molecules can adsorb between the fiber-electrode contact (site C).

In dependence of the actual sensor geometry (type I–III), some of the interaction centers are not accessible for the vapor. For example, when the electrodes are placed on top of the fibers, the fiber-electrode interface is buried below the electrodes, therefore the site C is not a possible interaction center for the sensor types II and III. The various interaction centers have been added to Table 4.2.

From the schematic representation of the various devices (Figure 4.9) it becomes evident, that only sensor type I allows the interaction of the vapor with the fiber-electrode contact. As this sensor device is the only sensor with a large positive response upon exposure to butylamine, it is concluded, that the large increase of resistance originates from the modification of the fiber-electrode interface. This finding is in accordance to the strong interaction of gold with amines [135], as well as with the V_2O_5 surface [136]. When butylamine intercalates between the gold electrode and the V_2O_5 nanofibers, the vapor increases the electrode-fiber separation, yielding an increased contact resistance.

A comparison of sensor types II and III would in principle allow a separation of the responses, originating either from interaction of butylamine with the fibers themselves (A), or with the fiber-fiber interface (B). However, such comparison is complicated by the scatter of responses from one sensor to the other, which is on the order of 50 % of the sensor signal. Nevertheless, it can be concluded, that the decrease in resistance upon exposure to butylamine for the sensors of type II and III, is most likely due to charge transfer from the butylamine to the n-type semiconducting V_2O_5-fibers. The increase of charge carrier density, results in a reduced fiber resistance. Charge transfer has also been invoked to explain the sensor response of ammonia interacting with a network of V_2O_5-fibers in the previous chapter 4.1. In addition, this explanation has been previously shown to be valid for the interaction of the fibers with aniline [137] and water [138].

The insensitivity to propanol and toluene might be interpreted, if it is assumed that electrode-fiber intercalation plays the essential role in resistance change. As both molecules show only weak interactions with gold and V_2O_5, the intercalation becomes less favorable compared to amines, resulting in the observed insensitivity to propanol and toluene.

Up to now, the role of the water-channel within the V_2O_5-nanofibers on the sensing mechanism has not been investigated in detail. One could envision, that the ability of amines to protonate in water enhances the intercalation of the analyte into the electrode-fiber interface. The low tendency of propanol and toluene to protonate in water, makes this pathway inefficient.

Further experiments are required in order to understand, on whether the butylamonium-cation, the hydroxyde-anion, or both participate in the intercalation process. Such experiments might be possible with a variation of the chain length of the primary amine, and a variation of the pH-value.

4.3 Hydrogen sensor

The V_2O_5-nanowire networks used as hydrogen sensors were fabricated similarly to the sensors described in chapter 4.1 for the detection of ammonia and to the original design used for sensing butylamine (chapter 4.2). V_2O_5-nanowires have been deposited as thin networks onto interdigitated gold electrodes with a separation of 10 μm.

For testing their performance, the sensors were subjected to the following conditions: (i) equilibration with nitrogen (0–1 min), (ii) exposure to hydrogen at the indicated concentration, diluted in nitrogen (1–4 min), (iii) flushing the device with nitrogen (4–6 min), and (iv) recovery of the sensor in dry air (6–10 min). The reason for using nitrogen followed by dry air after hydrogen exposure will be discussed below. Figure 4.10 shows the response of an unmodified V_2O_5-sensor, exposed to various concentrations of hydrogen. Only a weak resistance change can be observed for the unmodified sensor device. However, the behavior changes dramatically after evaporation of nominally 1 nm of palladium on top of the same device.

In contrast to the evaporation of nominally 1 nm gold on top of the networks, performed to achieve an improved detection of ammonia (chapter 4.1), no metal clusters could be detected after evaporation of palladium. A comparison of the unmodified fiber networks (Figure 4.11(a)) to the fibers modified with nominally 1 nm palladium (Figure 4.11(b)) reveals that the modified fibers appear brighter. This indicates a homogeneous coverage of the fibers with palladium. The surface of the device appears much rougher compared to the AFM images used for the V_2O_5/NH_3 study (Figure 4.1), as BK7-glass was used as substrate, which contains grooves from the polishing procedure. The resistance of the network is reduced after evaporation of palladium, which might be

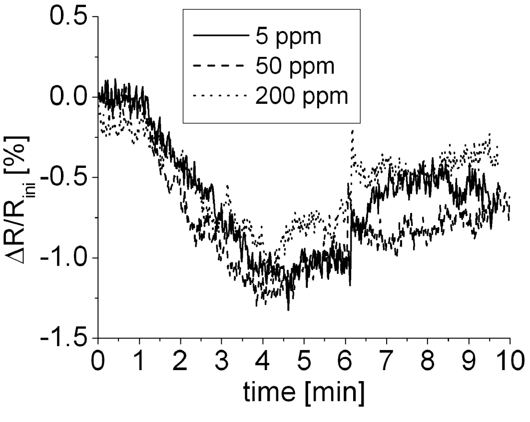

Figure 4.10: Response of an unmodified V_2O_5 network when exposed to various concentration of hydrogen diluted in nitrogen.

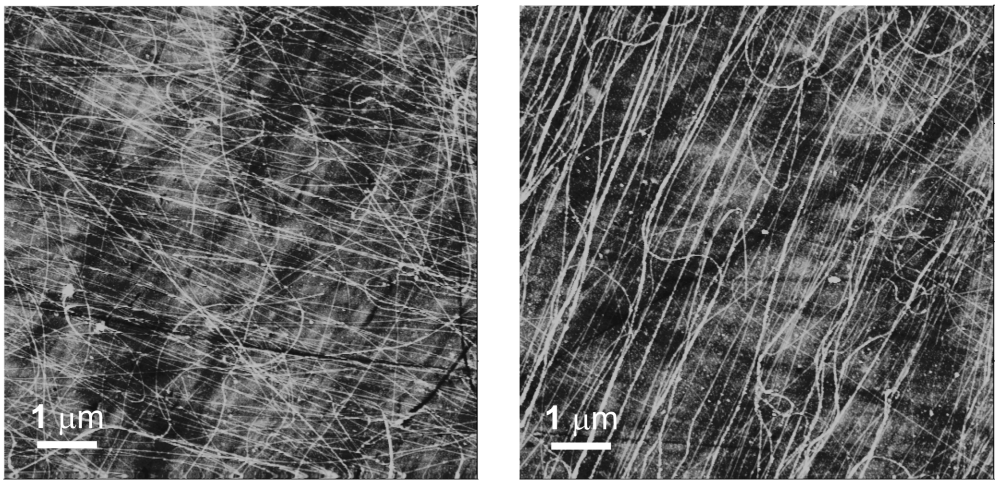

Figure 4.11: AFM images of (a) unmodified and (b) with nominally 1 nm palladium modified V_2O_5-network deposited on the interdigitated sensor device, fabricated on BK7-glass.

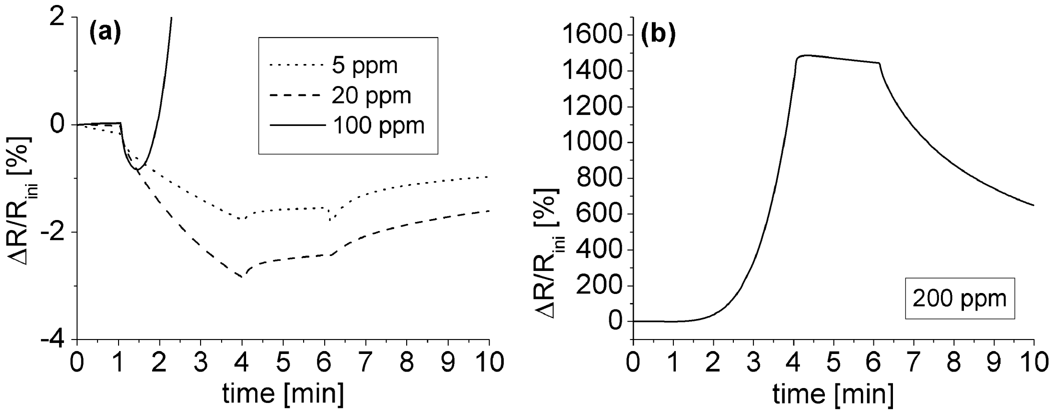

Figure 4.12: Response of a V_2O_5-sensor modified with nominally 1 nm palladium, when exposed to various concentrations of hydrogen diluted in nitrogen. Graph (a) covers the low concentrations of hydrogen, while part (b) shows the 200 ppm response.

attributed to a partial short-circuit of the nanowires by the metal. However, for reasons described below, it can be excluded that the sensor response is dominated by metallic pathways.

Figure 4.12(a) shows the responses of the Pd-modified V_2O_5-sensor exposed to low concentrations of hydrogen. Both the responses to 5 and 20 ppm of hydrogen show no distinct features with very moderate responses. Switching between test and reference gas causes fast drifts in the response, which are attributed to an abrupt change of pressure, rather than to the presence of a certain analyte. In comparison, a strong response is

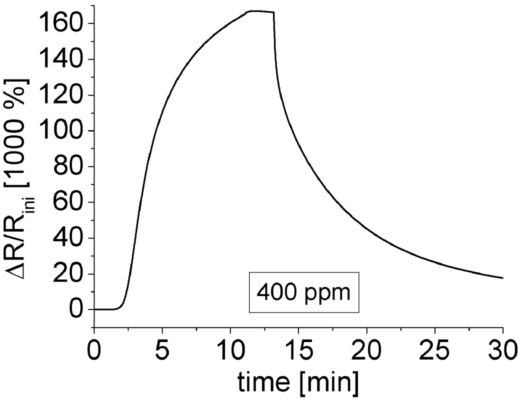

Figure 4.13: Saturation behavior of a Pd-modified V_2O_5 sensor, when exposed to 400 ppm of hydrogen. Note, that the scale of the y-axis is in units of 1,000 %, rather than in 1 %.

detected at an increased concentration of 100 ppm (solid line of Figure 4.12(a)). After a small negative dip in response (-1 %), the sensor shows a positive signal, which reaches a value of ~50 % after 3 min of exposure. Only part of the trace is displayed in order to highlight the responses within the low concentration range. A response of 1,400 % after 3 min exposure to 200 ppm hydrogen can be observed (Figure 4.12(b)), which is still below the saturation of the sensor device. Saturation behavior could be obtained after an exposure time of ~10 min at a hydrogen concentration of 400 ppm (Figure 4.13), giving rise to 160,000 %. This effect is dramatic, when compared to the maximum values on the order of 10 % obtained for the detection of ammonia or 500 % observed during exposure to butylamine.

4.3.1 Exposure to atomic hydrogen

Palladium is able to generate atomic hydrogen at room temperature [30, 139]:

$$2H_2 \xrightarrow{\text{Pd}} 4H$$

Atomic hydrogen can be removed with the aid of oxygen. The reaction between atomic hydrogen and oxygen creates water, which can subsequently desorb from the sensor surface:

$$4H + O_2 \longrightarrow 2H_2O$$

From Figures 4.12(b) and 4.13, it becomes evident that no recovery occurs under pure nitrogen, while a fast recovery is observed in dry air, in accordance to the reaction

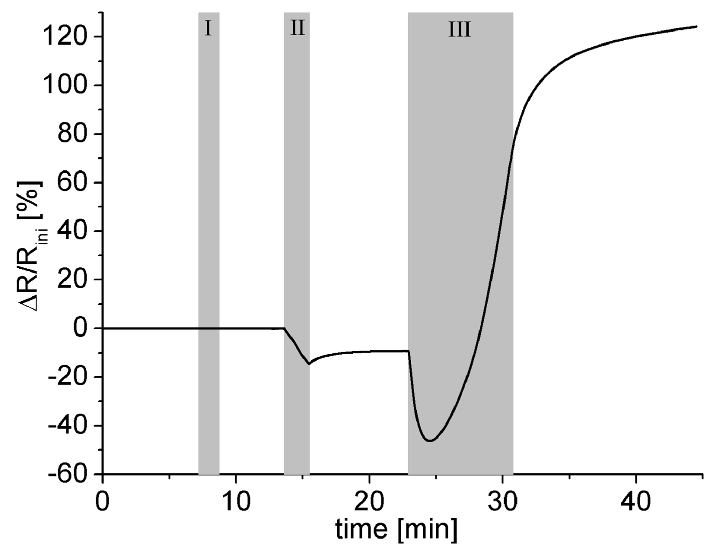

Figure 4.14: Response of an unmodified V_2O_5-sensor in an UHV environment, when subsequently exposed to 10^{-5} mbar H_2 (phase I), an indirect heat treatment (phase II), and a combined heat treatment in addition to a hydrogen pressure of 10^{-5} mbar (phase III).

scheme. In order to verify, that atomic hydrogen is responsible for the tremendous sensor response, additional experiments have been performed in an UHV-chamber equipped with an atomic hydrogen source. See chapter 2.2.4 for technical details. For this purpose an unmodified V_2O_5-sensor has been introduced to the UHV-system and kept for ~2 days at a pressure below 10^{-8} mbar in order to remove water and other contaminations from the surface.

To separate the effects of molecular hydrogen, atomic hydrogen as well as the indirect heat treatment originating from the tungsten filament of the atomic hydrogen source, the sensor has been exposed to the environments specified in Figure 4.14. During the exposure of the device to 10^{-5} mbar H_2 (phase I) no significant change of resistance has been observed in accordance to the measurements performed on the unmodified V_2O_5-network (see Figure 4.10). When the tungsten filament is operated at 9 V with a current of 33 A, a filament temperature of ~2000 K is reached (phase II). Due to the close proximity of the atomic hydrogen source to the sensor device (~10 cm), the temperature of the device increases by 6 K. As V_2O_5 is a hopping conductor, the conductivity of the device increases with rising temperature, as is evidenced by the experimental finding during phase II (Figure 4.14).

When hydrogen flows over the heated tungsten filament at a background pressure of 10^{-5} mbar (phase III), hydrogen dissociates at the filament and atomic hydrogen desorbs, which reaches the V_2O_5-sensor in front of the source. An initial decrease of the sensor response is followed by a steep increase of resistance. After both the filament and the hydrogen flow are turned off, the resistance of the sensor rises to a value of 120 %. This increase of resistance can be understood from cooling of the device after it has been heated up by ∼8 K due to the indirect heating by the tungsten filament. A temperature influence may also be responsible for the initial decrease of resistance during phase III, in which the temperature of the sensor device rises. However, it is also possible, that the initial decrease of resistance has a similar origin as the observed decreased of the Pd-modified V_2O_5-device in the case of exposure to low concentrations of hydrogen (100 ppm H_2, solid line of Figure 4.12(a)) performed at a constant temperature (∼300 K). As molecular hydrogen does not affect the resistance of an unmodified V_2O_5-network (phase I) and an increase of temperature yields a decrease of resistance of the fibers (according to phase II), the steep increase of resistance observed in phase III must be due to the presence of atomic hydrogen. It can therefore be concluded that palladium acts as a generator of atomic hydrogen, as has been suggested in the literature [39, 139].

4.3.2 Effect on charge transport behavior

Gas sensors composed of palladium films can reach a maximum change of resistance of 80 %, which has been explained in terms of a lattice expansion of palladium, due to the incorporation of hydrogen in the system [14, 15, 28, 139]. Sensor responses far beyond the 80 %-limit of pure Pd-sensors have been observed for the Pd-modified V_2O_5-sensor upon exposure to hydrogen, excluding a complete short-circuit of the V_2O_5-network. Therefore the lattice expansion cannot account for the hydrogen detection with the Pd-modified V_2O_5-sensor. It is furthermore unlikely that a pure doping of the wires, as described in the case of the ammonia sensor (chapter 4.1), is responsible for this effect.

The resistance of V_2O_5-crystals increases dramatic in the presence of atomic hydrogen. Responses between 1,000 % and 10,000 % have been reported in the literature [125] and were assigned to the formation of bipolarons. The formation of bipolarons has been theoretically predicted [140–142] and experimentally observed in heavily doped $M_xV_2O_5$ systems (M=Na [143, 144], Ag [145], Cu [146]) utilizing NMR and XRD studies.

Within the bipolaron model [125], the change of resistance can be understood in terms of the creation of V^{4+} sites upon dosing with atomic hydrogen. Initially, the increase of V^{4+}-sites yields an increased concentration of polarons, which causes an initial reduction of resistance. However, with increasing concentration of polarons it

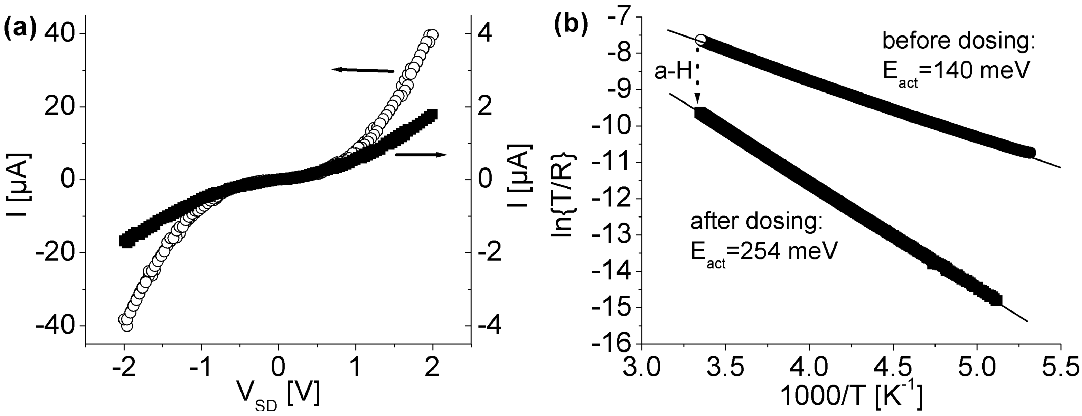

Figure 4.15: (a) I-V characteristic and (b) temperature dependence of resistance of a V_2O_5-network prior to (open circles) and after dosage with atomic hydrogen (solid squares).

becomes probable, that two neighboring polarons combine to bipolarons. Under this condition, charge transport can only occur, if (i) the bipolaron is split up in two separate polarons, or if (ii) the bipolaron is simultaneously transferred to a neighboring site. In the first case, the activation energy for hopping is predicted to be three times as high as the activation energy of a single polaron, while in the second case, the energy is four times as high [147, 148]. The increased activation energy reduces significantly the mobility of bipolarons compared to the polaron mobility. In a mixed system containing both polarons and bipolarons an effective activation energy is expected, ranging between those of polarons (E_a) and bipolarons ($4\,E_a$). This intermediate activation energy reflects both the increased activation energy due to the formation of bipolarons, as well as the reduced concentration of polarons.

In order to consolidate the model of bipolaron formation, temperature-dependent electrical transport measurements have been performed under UHV on unmodified V_2O_5-networks. Prior to dosing with atomic hydrogen, the V_2O_5-network shows an I-V characteristic (open circles in Figure 4.15(a)) typical for a hopping conductor (equation (3.3)). The resistance of the sample has been measured in the temperature range of 200–300 K and is plotted in Figure 4.15(b). On the basis of equation (3.1), an activation energy of 140 meV is calculated prior to application of atomic hydrogen.

In analogy to the previous section, atomic hydrogen has been dosed onto the device, while the sensor was close to room temperature (300–315 K). The dosage has been maintained until the resistance increased by roughly two orders of magnitude, as apparent from the I-V characteristic after modification (solid squares in Figure 4.15(a)). Similar to the results of phase III in Figure 4.14, an initial drop in resistance was observed. The measurement of the temperature dependence of resistance has been repeated after the treatment with atomic hydrogen (solid squares in Figure 4.15(b)). Under the assumption, that the electrical transport can still be described with the hopping-like model, an increased activation energy of 254 meV is obtained.

The activation energy increased by a factor of ∼2. From theory a factor of 3–4 is predicted [148, 149] for a saturated system of bipolarons with only a minor fraction of thermally activated polarons. However, in the present study no saturation with atomic hydrogen has been obtained, as the duration of the exposure to atomic hydrogen was only maintained until the resistance of the sensor was altered by two orders of magnitude. Therefore the V_2O_5-network reflects a mixed system of polarons and bipolarons, giving rise to an activation energy only twice as high as that of the sample prior exposure with atomic hydrogen.

4.3.3 Structural changes

The change of resistance has been related to the creation of V^{4+}-sites within the V_2O_5-nanofibers as a result of chemical reduction by atomic hydrogen. So far, however, it is not clear, by which mechanism the atomic hydrogen alters the valence of the V-atoms from 5+ to 4+. Two different models for the interaction of atomic hydrogen with V_2O_5 can be found in the literature. At first sight, both appear equally suited to describe the creation of V^{4+} centers and the recovery of the sensor response in the presence of oxygen.

Hydrogen insertion

The insertion of atomic hydrogen into the structure of V_2O_5-crystals has been described by various authors and experimentally observed by XRD-measurements [150–152]. The change of resistance due to the creation of bipolarons has been explained in the framework of the hydrogen insertion [125].

Within this model, hydrogen is inserted between two bridging oxygen atoms. Electrons are transferred from the hydrogen atoms to adjacent vanadium atoms reducing their valences from V^{5+} to V^{4+}. Removal of hydrogen from the V_2O_5-crystal can be achieved with the aid of oxygen, yielding water. The following two equations describe the microscopic mechanism of this model:

$$\begin{aligned} V^{5+} - O_{(2)} - V^{5+} \ + \ 2H \ &\longrightarrow \ V^{4+}H^+ - O_{(2)} - V^{4+}H^+, \\ V^{4+}H^+ - O_{(2)} - V^{4+}H^+ \ + \ \tfrac{1}{2}O_2 \ &\longrightarrow \ V^{5+} - O_{(2)} - V^{5+} \ + \ H_2O \end{aligned}$$

Catalytic reaction with hydrogen

The second model is based on the catalytic activity of V_2O_5, which follows in most cases the two-step Mars-van Krevelen mechanism [153]. In the first step, the educt (for example CO) is oxidized by the surface oxygen (yielding CO_2), producing a reduced and defective catalyst. In the second step, environmental oxygen is used to re-oxidize the catalyst. For the reaction with atomic hydrogen as educt, these two processes can be formulated as:

$$\begin{aligned} V^{5+} - O_{(2)} - V^{5+} \ + \ 2H &\longrightarrow V^{4+} \cdots \quad \cdots V^{4+} \ + \ H_2O, \\ V^{4+} \cdots \quad \cdots V^{4+} \ + \ \tfrac{1}{2}O_2 &\longrightarrow V^{5+} - O_{(2)} - V^{5+} \end{aligned}$$

Belousov et al. [154] have shown that in the presence of palladium on top of a V_2O_5-crystal, the addition of hydrogen can remove lattice-oxygen. This reaction takes place at room temperature, while a temperature of $\sim$300°C is needed in the absence of palladium. There is currently no consensus regarding which type of oxygen ($O_{(1)}$–$O_{(3)}$) is involved in the catalytic reaction [155, 156]. The quality of the V_2O_5 material (crystalline/powder) has a significant influence on its catalytic properties [157], while theoretical modelling strongly depends on finite size effects and faces difficulties with a correct relaxation of the crystalline structure after oxygen removal [158]. In a review by Surnev, Ramsey and Netzer [159], it was concluded that this problem is still unsolved. Most studies are in favor of the vanadyl oxygen $O_{(1)}$ (see [156] and references therein), while a few others favor the bridging oxygen $O_{(2)}$ to participate in the Mars-van Krevelen mechanism [157, 158]. It is noteworthy, that a recent HREELS study by Tepper and co-workers [157] on an UHV-cleaved $V_2O_5(001)$ surface reported the disappearance of the V-$O_{(2)}$-V vibration upon dosage with atomic hydrogen, while no intermediate OH-vibrations were observed, which would be expected for the decomposition of oxygen from the V_2O_5-surface.

Raman spectroscopy

Whether the hydrogen insertion or the catalytic mechanism is operative in the present sensors, cannot be distinguished on the basis of pure electrical measurements. However, this task can be achieved with the aid of Raman spectroscopy, as the two predicted mechanisms alter the crystal structure in different ways, which should be reflected in distinct Raman spectra.

Raman experiments on a Pd-modified V_2O_5-network have been performed in analogy to chapter 3.3.1. Upon exposure to a constant flow of nitrogen in the glass cell (chap-

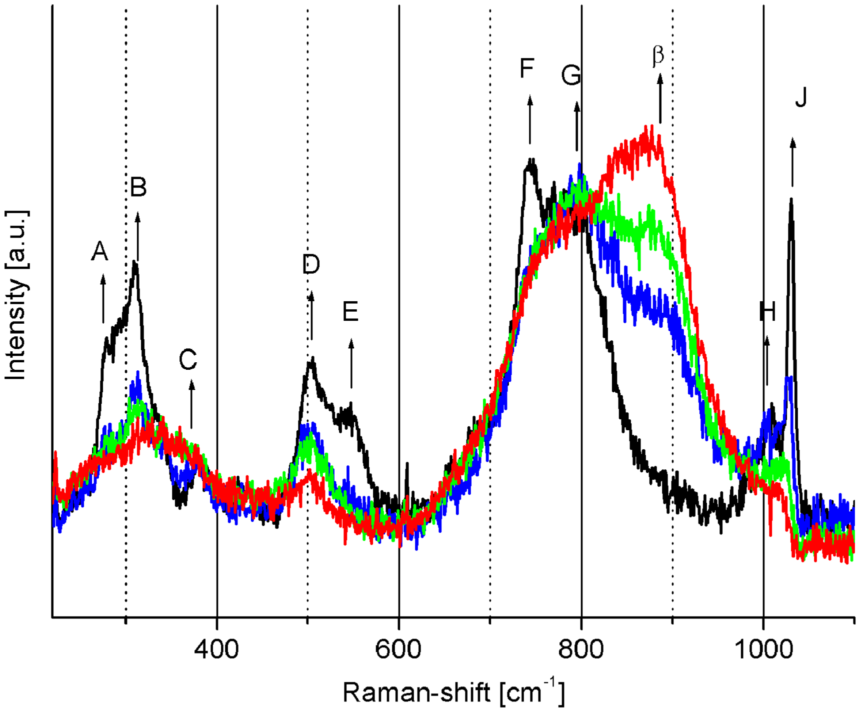

Figure 4.16: Evolution of Raman spectra of a palladium-modified V_2O_5-network with time (duration ~3 h), as the device has been exposed to a pure hydrogen atmosphere. The evolution goes from black, blue, green to red with time. The peaks are assigned in accordance to the Raman measurements of chapter 3.3.1.

ter 2.1.3), no significant changes of the Raman spectra could be observed. Slight variations in the overall intensity have been observed, which are attributed to pressure variations and different positions of the glass cell relative to the optical setup. These variations could be compensated by re-adjusting the sample height.

Significant changes of the Raman signal have been observed upon exposure of the palladium-modified V_2O_5-nanofibers to 100 % hydrogen at room temperature. Figure 4.16 shows the temporal evolution of the Raman spectrum in the range of 200–1100 cm^{-1} over a time-span of ~3 h (black → blue → green → red). The peaks are labelled according to chapter 3.3.1. Except for the broad peak at 800 cm^{-1} (peak G), all peaks decrease in intensity. In addition, the emergence of a new peak at 875 cm^{-1} (labelled β) is observed. Compared to the sensor responses, the change of the Raman spectra is very slow, although a maximum hydrogen concentration was used. This difference is attributed to the larger film thickness (0.3 μm), required to achieve sufficient Raman intensity. The increased thickness has the drawback of a slow diffusion of atomic hydrogen through the film.

In the framework of the hydrogen insertion scheme, the vanadyl-oxygen vibration (1030 cm^{-1}, J) should be shifted to 930 cm^{-1} (γ). However, no peak is observed at this position, excluding the hydrogen insertion scheme to be responsible for the gas sensing mechanism. The catalytic mechanism implies the removal of $O_{(2)}$- and/or $O_{(1)}$-atoms from the V_2O_5-surface, which should be reflected by the disappearance of the corresponding vibrations (V-$O_{(2)}$-V, V=$O_{(1)}$). The reduction of Raman intensities of most of the peaks (A–F, H, J) is in accordance to this scheme. However, as all peak intensities are reduced, it is not possible to determine which type of oxygen-atoms are removed. The removal of oxygen from the V_2O_5-nanofibers appears to be associated with a reduction of the crystalline order of the system, it becomes partially amorphous. Another indication for the presence of additional disorder is the remaining intensity of the broad disorder-related band at ~800 cm^{-1} (G).

The appearance of the new peak β has previously been assigned to weakly bound water attached to the vanadium. These molecules are capable to shift the vanadyl-oxygen vibration from 1030 cm^{-1} to 895 cm^{-1} [109]. In the light of the catalytic reaction scheme, one can imagine that the atomic hydrogen couples to an $O_{(2)}$-atom, accompanied by breaking one of the bridging bonds (and therefore reducing the previously joint V-atom) and creating an OH-group attached to the second V-atom. In a subsequent step, a second hydrogen atom attaches to the OH-group forming a water molecule that remains weakly coupled to the second V-atom, while reducing its valence:

$$\begin{aligned} V^{5+} - O_{(2)} - V^{5+} \ + \ 2H \ &\longrightarrow \ V^{4+} \quad HO - V^{5+} \ + \ H \\ &\longrightarrow \ V^{4+} \quad H_2O \cdots V^{4+} \end{aligned}$$

A similar reaction scheme may be envisioned for the $O_{(1)}$-atoms. Recovery of the sensor follows the catalytic reaction scheme as described above, while releasing the weakly coupled water molecule to the water channel. Compared to the predicted interactions of V_2O_5-crystals with atomic hydrogen [157], two differences are observed: (i) the disappearance of vibrational features that are not exclusively related to the $O_{(2)}$-atom, and (ii) the coupling of water molecules to the V-atoms, which do not desorb. Both differences may be explained by the different experimental conditions. While Tepper et al. [157] have used an UHV-cleaved $V_2O_5(001)$ surface that has been dosed with atomic hydrogen, the V_2O_5-nanofiber sample is composed of a thick network of V_2O_5-nanofibers, which have been indirectly dosed with atomic hydrogen via the use of palladium. The difference in crystal structure may be of great importance for the reactivity of the surface oxygen. While V_2O_5-crystals are composed of stacked layers, V_2O_5-nanofibers are comprised of bilayers separated by a water channel. These water channels may also be responsible for the strong binding of water molecules to the vanadium atoms, as the freshly created water molecules can not only couple to the vanadium atom, but also to the water channel via hydrogen bonds.

Despite the small differences to the predictions of Tepper and coworkers [157], the catalytic reaction of atomic hydrogen accounts well for the creation of V^{4+}, which is essential for the observed rise in resistance. The inability of the hydrogen insertion mechanism to explain the experimental findings may be understood in the difference between surface and bulk effects. The insertion mechanism has been previously observed in a bulk crystal [150], while the above discussed measurements have been performed on V_2O_5-nanofibers, which essentially are composed of surface atoms exclusively.

4.3.4 Sensor performance

After addressing the sensor mechanism operative in the detection of hydrogen with a network of palladium-modified V_2O_5-nanofibers, the sensor performance has been studied. As described above, the sensing mechanism most likely involves the creation of disorder in the fibers, which are subsequently “healed” with atmospheric oxygen. In order to elucidate the sensor behavior upon repeated exposure/recovery, a fresh Pd-modified V_2O_5-sensor has been alternatingly exposed to 2000 ppm hydrogen in nitrogen (3 min) and dry air (7 min). The resulting changes of resistance are plotted in Figure 4.17. It is noted, that during the time period 32–43 min, pure nitrogen has been used and no recovery could be observed due to the absence of oxygen. The increase of resistance during each exposure step is 8,200±500 %. The recovery of the sensor is not complete after 7 min in dry air and a residual sensor response of ∼1/3 of the maximum response remains. In turn the overall response shifts to higher values, as a residual “loading” of oxygen vacancies already exist on the V_2O_5-nanofibers during subsequent exposures. No decrease in sensor response is observed with increasing time, indicating that no irreversible damage of the sensor occurs.

The experiments described so far have been performed with hydrogen diluted in nitrogen in order to prevent a partial recovery of the sensor during exposure, and dry air has been subsequently used for the recovery of the sensor. In order to simulate ambient conditions, hydrogen has been diluted in dry air. In this case, however, no relative humidity has been added, which may be subject of future work. Furthermore, the flushing with nitrogen after hydrogen exposure was omitted for obvious reasons. Despite the presence of oxygen, significant responses could be detected at low concentrations of hydrogen for the Pd-modified sensor device (Figure 4.18). Similar to the results obtained in nitrogen, the low concentration responses of hydrogen in dry air are initially negative, but turn to positive values at a concentration of 200 ppm (Figure 4.18(a)). Responses

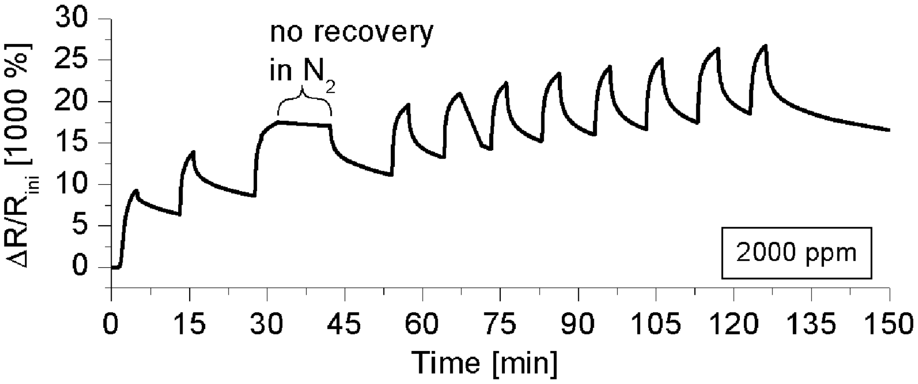

Figure 4.17: Repeated exposure to 2000 ppm H_2 in nitrogen. Recovery occurred in dry air. During the time-period 32-43 min pure nitrogen was added to the system, in order to attest that oxygen is needed for recovery. Note, that the scale of the y-axis is in 1000 % rather than in 1 %.

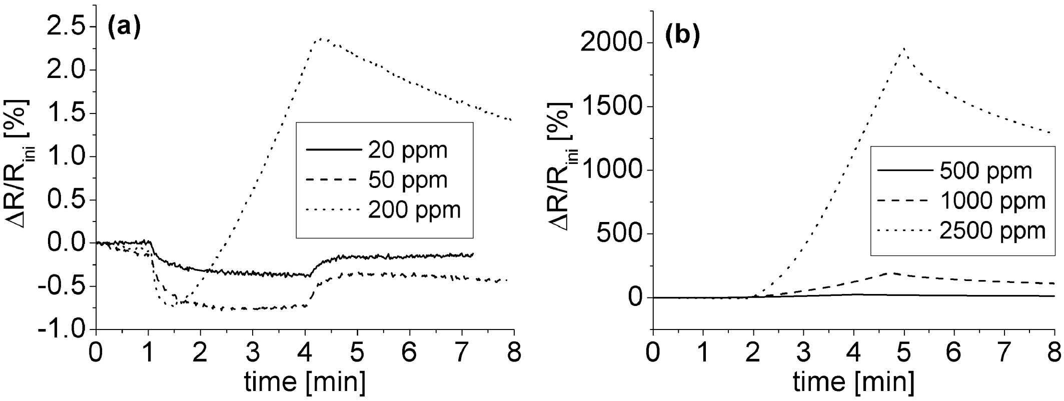

Figure 4.18: Sensor responses of a Pd-modified V_2O_5-sensor, when exposure to various concentrations of hydrogen diluted in dry air.

exceeding 1,800 % have been obtained at a hydrogen concentration of 2,500 ppm (Figure 4.18(b)). As discussed previously, these responses do not correspond to saturation, but describe the responses obtained after 3 min. Compared to the results of the experiments performed in nitrogen, e.g. 1,500 % at 200 ppm, the responses in dry air are significantly lower. However, one should keep in mind, that vacant oxygen sites are instantaneously "repaired" during the exposure. Furthermore, compared to the results of the detection of ammonia, the absolute values of responses are still tremendous, making the Pd-modified V_2O_5-device attractive for technical applications in a "real-world" environment.

Chapter 5

Gas sensors composed of carbon nanotubes

Carbon nanotubes have attracted strong interest as components of gas sensors [32, 33, 39, 47–49], due to their high surface-to-volume ratio. Despite the complication that single-walled carbon nanotube samples generally contain a mixture of semiconducting and metallic tubes, two advantages are clearly apparent compared to V_2O_5-nanofibers. Firstly, the physical properties of carbon nanotubes including their electronic structure and their interaction mechanism with gases can be estimated from the known properties of graphite. Secondly, the electrical conductivity of carbon nanotubes is much higher compared to V_2O_5-nanofibers.

The first type of sensor (chapter 5.1), which comprises unmodified nanotubes, has been employed to detect ammonia. These experiments were supplemented by thermal desorption spectroscopy, as this technique allows direct insight into the interactions of ammonia with carbon nanotubes.

The evaporation of palladium on top of nanotubes has been shown to yield a good hydrogen sensor [39], which is based on the creation of atomic-hydrogen, in analogy to the case of the palladium-modified V_2O_5-sensor (chapter 4.3). Here an electrochemical deposition method is employed, which yields a selective deposition of palladium clusters onto the nanotube network (chapter 5.2). The sensitivity of these modified networks to hydrogen is characterized with Langmuir adsorption theory.

5.1 Ammonia sensor

In order to achieve a sufficient sensor signal, the detection of gases exhibiting pronounced donor (NH_3, [47, 49, 160]) or acceptor (NO_2, [32, 33, 47, 49]) properties have been investigated. The sensor mechanism is well understood in terms of charge transfer from the adsorbed gas to the nanotube [160–163]. As O_2 and NO_2 are electron acceptors, the conductivity of a p-type semiconducting nanotube increases, while the electron donating NH_3 decreases the conductivity. Experimentally it was observed that this effect is also valid for network samples, which are composed of metallic and semiconducting nanotubes.

While adsorption-induced electronic changes in the nanotubes have been studied in great detail, little information is known on the molecular interaction, including binding energy and adsorption sites (e.g. nanotube surface, grooves of a bundle, defect sites). As reactive gases have been used, strong interactions with the nanotubes are expected. In the case of NO_2, desorption at room temperature could only be obtained with the aid of UV-irradiation [32, 33]. As an example for the interaction of carbon nanotubes with a polar gas, ammonia has been studies as analyte.

Isolated nanotubes (arrows) and small bundles of 3–7 tubes per rope (triangles) have been deposited as a SWNT-network on a SiO_2/Si-wafer, as depicted in Figure 5.1. The network is electrically contacted via gold electrodes with a separation of ~20 μm (see chapter 2.2.2 for details). Figure 5.2 displays the response of such a network, when subsequently exposed to 1, 5, 20 and 100 ppm of ammonia. A significant and fast increase in resistance can be observed, in accordance to the electron donating property of

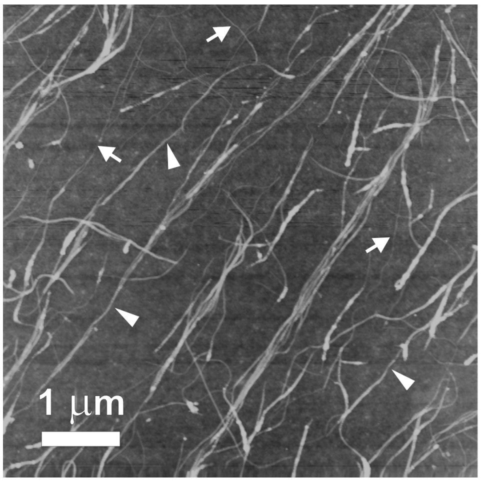

Figure 5.1: AFM-images of carbon nanotubes. The arrows indicated individual nanotubes, while the triangles refer to small bundles.

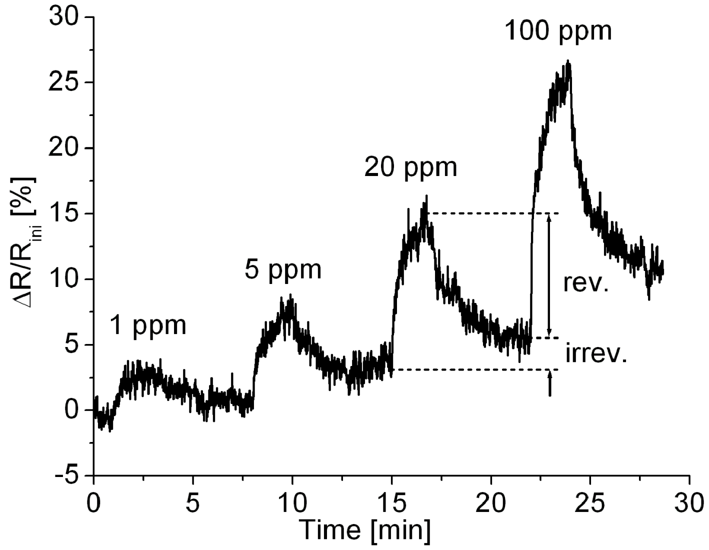

Figure 5.2: (a) Response $\Delta R/R_{ini}$ of a nanotube-network, when exposed to ammonia. The numbers within the figure indicate the corresponding concentrations. The arrows "rev." and "irrev." show, respectively, the reversible and irreversible contribution of the response for the exposure to 20 ppm ammonia.

ammonia, and consistent with the fact, that the sensor contains p-type semiconducting nanotubes [47,160].

After the ammonia is turned off, a decrease of resistance can be observed, which is attributed to (partial) desorption of ammonia from the nanotube material. However, the initial resistance of the sensor is not completely recovered.

To understand the kinetic behavior of the nanotube sensor, it is important to recognize that the response consists of a reversible and an irreversible component. The irreversible component for a single exposure can be defined as the difference between the equilibrium resistance after desorption and the resistance prior this exposure.

As the maximum sensor response for each concentration originates from both, the reversible and irreversible adsorption of the gas molecules to the nanotubes, the reversible contribution to the signal is given by the difference between the total and irreversible response. As an example, the two contributions are indicated with arrows in Figure 5.2 for the case of exposure to 20 ppm ammonia.

5.1.1 Modified Langmuir isotherm

To model the adsorption kinetics associated with the two contributions to the sensor signal, proportionality of response $\Delta R/R_{ini}$ and coverage θ ($0 \leq \theta \leq 1$) is assumed ($\Delta R/R_{ini} = \Delta R_{\infty} \cdot \theta$), as in the case of the ammonia sensor based on V_2O_5-nanofibers.

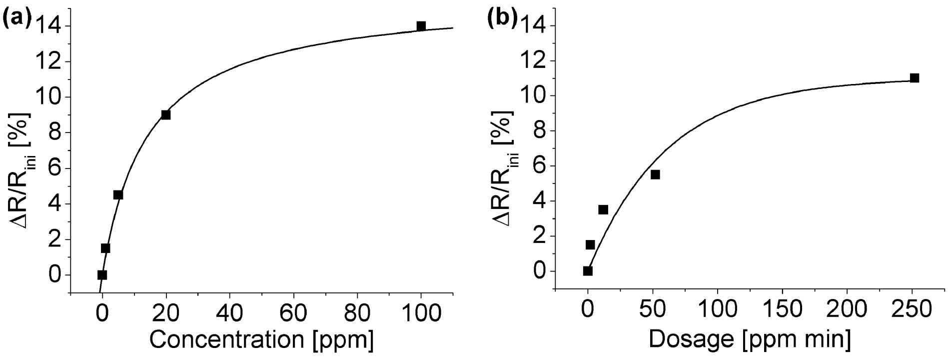

Figure 5.3: (a) Reversible response as a function of gas concentration. Langmuir analysis yields $\Delta R_{\infty,rev} = 15.7\%$ and $K = 0.07$ ppm^{-1}. (b) Irreversible total response as a function of total dosage ($\Delta R_{\infty,irrev} = 11.0\%$, $k_{ads} = 0.016$ (ppm·min)$^{-1}$).

For the case of regular (fully reversible) ad- and desorption, the coverage θ can be modelled with the Langmuir isotherm (equation (4.4), [127]), as has been introduced in chapter 4.1. A plot of the reversible contribution to the sensor response as a function of concentration c is given in Figure 5.3(a). The solid line represents the corresponding Langmuir fit, from which a maximum reversible response of $\Delta R_{\infty,rev} = 15.7$ % is determined. Despite the presence of different adsorption sites in carbon nanotubes (e.g. surface and grooves), a good Langmuir fit could be obtained.

The irreversible contribution of the sensor performance can be modelled with a modified Langmuir theory. With the constraint $k_{des} = 0$, it follows immediately from equation (4.3), that the coverage always approaches saturation ($\theta = 1$), independent of concentration c. For successive exposures (as depicted in Figure 5.2), a pre-coverage θ_{n-1} of the sensor must be taken into account. The time-evolution during the n-th adsorption step is found to be:

$$\theta_n = 1 - [1 - \theta_{n-1}] \cdot \exp\{-k_{ads} \cdot c_n \cdot t_n\}, \tag{5.1}$$

where c_n and t_n correspond to the gas concentration and duration of exposure at step n, respectively. Note the close relation to equation (4.5) found for reversible adsorption, which has been modified with $\theta_c = 1$ and $1/\tau_{exp} = k_{ads} \cdot c$. The pre-exponential factor has been replaced by $[1 - \theta_{n-1}]$ to account for the pre-coverage.

As only the change of resistance can be observed, rather than the actual coverage of the sensor, equation (5.1) can not directly be applied to the experimental data. Instead the equation needs to be solved iteratively[1] with the condition of negligible coverage

---

[1] Successively inserting the definition of θ_{i-1} according to equation (5.1) in θ_i.

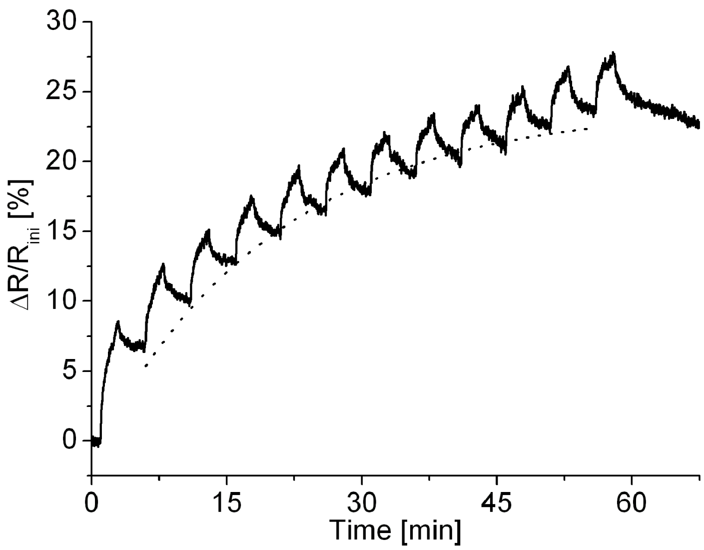

Figure 5.4: Repeated exposure to 50 ppm of ammonia. The dashed line indicates the saturation behavior of the irreversible contribution to the sensor response.

prior the first exposure ($\theta_0 = 0$):

$$\theta_n = 1 - \exp\left\{-k_{ads} \cdot \sum_{i=1}^{n} c_i \cdot t_i\right\} \tag{5.2}$$

Defining the product $c_i \cdot t_i$ as dosage at step i, the total coverage –that is the sum of all previous irreversible adsorption– can be expressed as a function of total dosage (Figure 5.3(b)). A value of 11.0 % was obtained for the maximum irreversible response $\Delta R_{\infty,irrev}$.

Figure 5.4 shows the response of a nanotube sensor, repeatedly exposed to 50 ppm of ammonia. The dashed line indicates the irreversible contribution to the sensor signal, which saturates in accordance to equation (5.2). The constant amplitude of the reversible part clearly proofs the independence of the ir- and reversible adsorption sites, as proposed above. If there would be an interplay between the two types of adsorption centers, a decrease of the reversible signal would become visible.

The above developed adsorption model could be supported by intentionally introducing additional defects in the carbon nanotubes. To this end, a nanotube sensor was exposed to a mild oxygen plasma treatment (20 W, 3 sec, [164,165]), after initial testing the responses to ammonia. The resulting sensor signal was larger by a factor of three for exposure to the identical concentration of ammonia. The enlarged response can be attibuted to a dominant adsorption on freshly created defects. Subsequent exposure to ammonia gave rise to a reduced response, as the defect sites where already occupied and

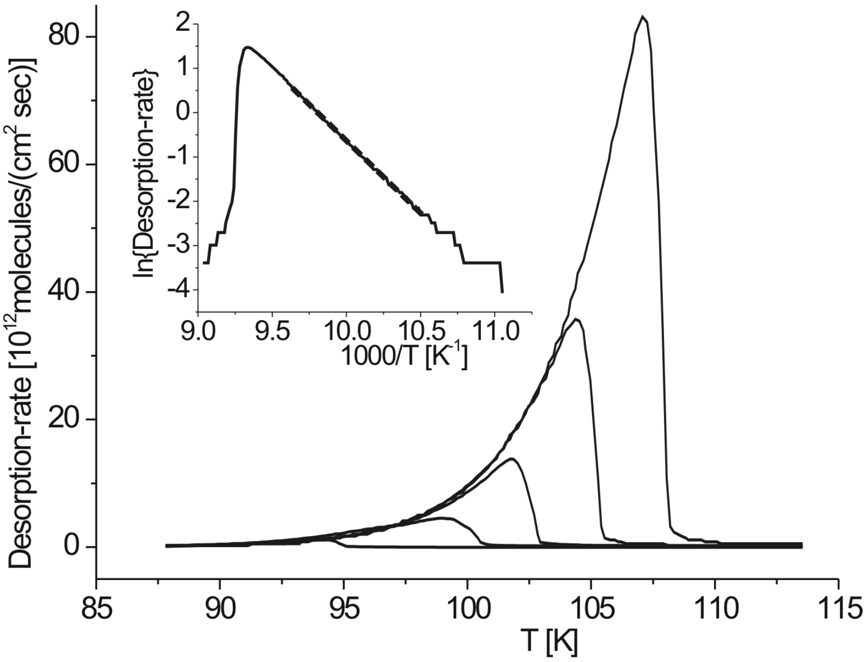

Figure 5.5: Thermal desorption spectra of ammonia on graphite for coverages of 0.4–19.8 ML$_{gra}$. (inset) Arrhenius plot of (a) for determining the binding energy [85].

could not further contribute to the large sensor response.

5.1.2 Thermal desorption spectroscopy

To clarify the origin of the irreversible contribution to the sensor signal, thermal desorption spectroscopy (TDS) has been performed. This method enables an evaluation of the gas-nanotube interactions and experiments have been performed previously for inert species (e.g. Xe [86, 164, 166]), whereas only little attention was paid to more reactive molecules. See chapter 2.1.4 for experimental details.

Thermal desorption spectra of ammonia on graphite, which was used as a reference material, are displayed in Figure 5.5. The spectra show a single feature which reflects zero order desorption kinetics for increasing coverage (0.4–19.8 ML$_{gra}$) [167]. The existence of only one desorption feature can be explained by a stronger bond between the adsorbate molecules than between the adsorbate and the substrate, leading to a non-complete wetting of graphite by ammonia, known as island growth mode (Volmer-Weber). Applying an Arrhenius plot method (inset of Figure 5.5) a binding energy of 27 kJ/mol (280 meV) can be derived. This value is in good agreement with literature

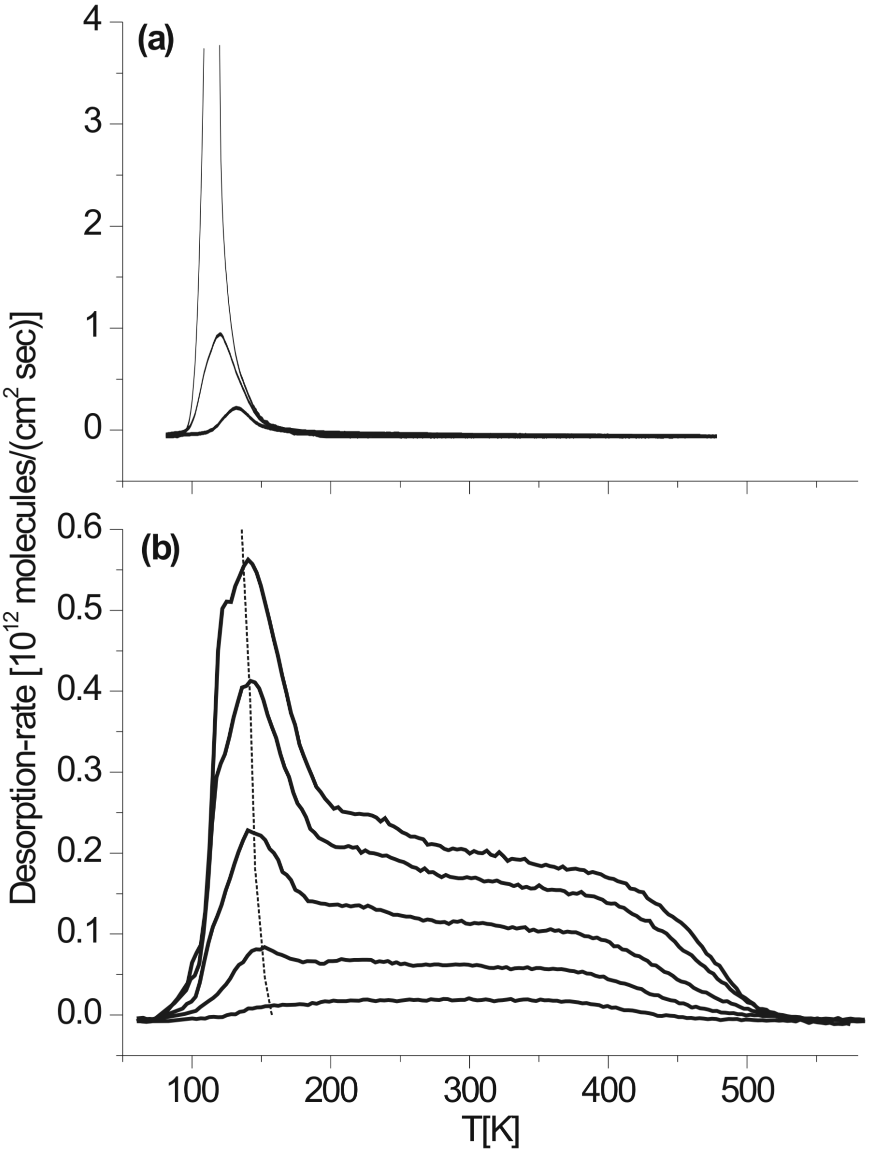

Figure 5.6: Thermal desorption spectra of ammonia on SWNT. (a) high coverage of SWNT (0.14–1 ML_{SWNT}) and (b) low coverage of SWNT (0.001–0.04 ML_{SWNT}) [85].

values [168] for carbon black samples, and corresponds to the binding interactions between ammonia molecules within the adsorbate crystal. The tiny feature observed at about 95 K in Figure 5.5 is due to an amorphous phase of the crystalized NH_3 for low surface concentrations (like observed for adsorbed water [169]).

Purified and degassed bucky-paper has been used for the TDS experiments. The high coverage spectra of SWNT (0.14–1 ML_{SWNT}) in Figure 5.6(a) show a desorption feature at nearly the same temperature (110–120 K) as observed for graphite, which can be ascribed to the sublimation of the crystalized ammonia. In the low coverage TD spectra of SWNT (0.001–0.04 ML_{SWNT}), depicted in Figure 5.6(b), a peak-like feature is present, with a maximum at 145 K. With increasing coverage, the 145 K feature evolves towards the 110 K peak for high coverage (dashed line in Figure 5.6(b)). Most strikingly, however, is the wide desorption band within the range of 180–500 K, corresponding to binding energies from 36 to 132 kJ/mol (370–1370 meV), as calculated with the Redhead formula [170] with a frequency factor of $5 \cdot 10^{13}$ s^{-1}. This factor has been derived from vapor pressure curves, as described elsewhere [85, 171]. Simple broadening of the desorption feature, as described by local effects like diffusion and coordination for inert gases [86,172], can not account for the high temperature band. Instead, the experimental findings more likely reflect the polar nature of the analyte ammonia. This polarity opens up the possibility to adsorb the ammonia molecules to nanotube defects, which themselves have a dipole moment. Within this assumption, the large binding energy can be understood to originate from strong dipole-dipole interactions. The presence of different types of defects, such as missing atoms in the nanotube lattice or residual chemical groups, can explain the large width of the desorption band.

Theoretical calculations on isolated ammonia molecules on individual nanotubes gave adsorption energies of 130–180 meV [162, 163]. Compared to the lowest adsorption energy of 370 meV measured for bucky-paper, these values are quite low. The difference can be attributed to the fact, that the value of 370 meV corresponds to the sublimation energy of ammonia on ammonia, rather than the adsorption energy of ammonia on nanotubes. Therefore the adsorption energy can not be determined, as the strong adhesion between the ammonia-molecules has to be overcome before the (low energy) desorption of ammonia from the nanotubes can occur.

As complete desorption of ammonia from nanotubes requires temperature above 300 K –the desired operation temperature of the sensor– a fraction of the adsorbed gas remains permanently attached to the nanotubes, when the nanotubes are kept at room temperature. These molecules are hence responsible for the observed irreversible sensor response visible in Figures 5.2, and 5.4.

Based on the integrated desorption spectra below and above 300 K, a fraction of approximately 1/5 of the gas molecules adsorb irreversibly. The accurate fraction depends on the actual, but unknown coverage during sensor operation at room temperature. As only a small fraction of the adsorption sites was assigned to be irreversible, it is rather striking, that the maximum responses of the reversible and irreversible contribution to the sensor signal are almost identical (15.7 % and 11.0 %, respectively). This observation can be explained with an increased charge transfer of ammonia to nanotubes for the case of strong coupling to nanotubes, compared to the weak coupling in the case of reversible adsorption. As the binding energy of ammonia at defects (up to 1370 meV, see Figure 5.6) is three times stronger than on the defect-free surface (370 meV), the assumption of increased charge transfer appears reasonable.

For completeness, it should be noted, that different nanotube samples have been used for the gas sensing measurements and thermal desorption spectroscopy. The samples differ in bundle size and purity. The nanotubes used for the thermal desorption spectroscopy have been degassed at 1200 K, therefore the number of chemical groups attached to the nanotubes is significantly reduced compared to a non-degassed sample. As the sensor devices have not been degassed, the strong irreversible contribution to the sensor signal might also be attributed to the presence of chemical defects.

Gas sensing measurements at room temperature bear the drawback of irreversible adsorption of ammonia onto the nanotubes. For technical gas sensing applications utilizing nanotubes as sensor material, two procedures may proof useful to overcome this problem: Firstly, the operation at elevated temperature would minimize the number of irreversible adsorption sites. As a secondly possibility, a specific modification of the nanotubes could reduce the number of polar groups and/or make them sensitive to certain analytes [39, 49].

5.2 Electrochemical modification for hydrogen detection

So far, the modifications of V_2O_5-nanofibers and carbon nanotubes were realized via metal evaporation onto the devices. While this is a straightforward technique, it has two shortcomings: (i) the evaporation is not specific to the nanowires, but particles are formed on the whole substrate, (ii) the thickness of the evaporated layer can not precisely be controlled. The thickness of the evaporated metals is essentially important, since a very thin layer will not improve the sensing properties, while a thick layer will short-circuit the device.

To overcome these disadvantages, chemical metal deposition methods have been investigated. With the aid of wet chemistry, it is possible to selectively modify carbon nanotubes with gold clusters. For this purpose, 10 mg chloro(dimethylsulfide)gold ($Au^+S(CH_3)_2Cl^-$, Aldrich) have been dissolved in 10 ml N-methylformamide. Carbon nanotube networks, deposited on Si/SiO_2 wafers, were dipped into the solution for 1 min. The solution changed its color from pink via violet to brown within ~20 min, indicating the formation of gold clusters within the solution.

Figure 5.7 shows AFM images of two carbon nanotube networks that have been modified with the gold complex. Two distinct morphologies have been obtained in dependence on whether the nanotubes are contacted or not. The sample of Figure 5.7(a) is a non-contacted carbon nanotube network, which is decorated by Au-clusters with a height of ~25 nm. The network used to obtain Figure 5.7(b) has been previously

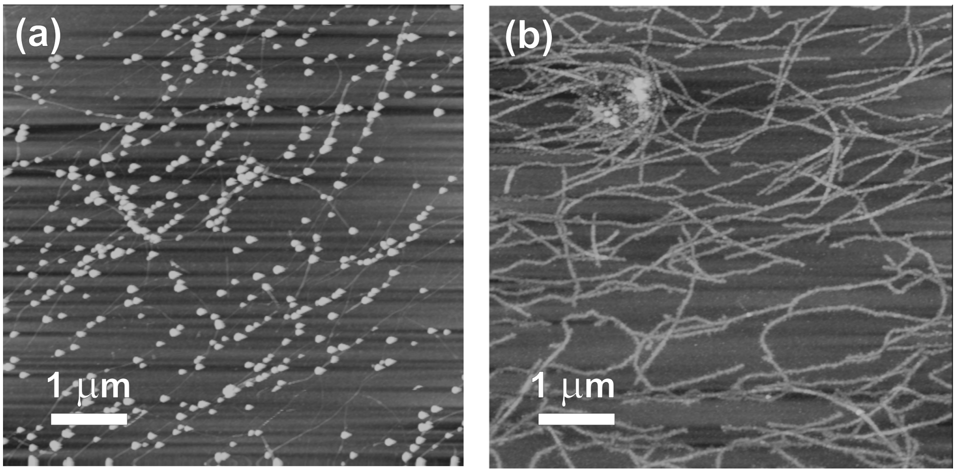

Figure 5.7: AFM image of carbon nanotubes modified with a gold complex. (a) displays the result in absence of electrodes, while (b) reflects the sample, where the nanotubes are contacted with gold-electrodes.

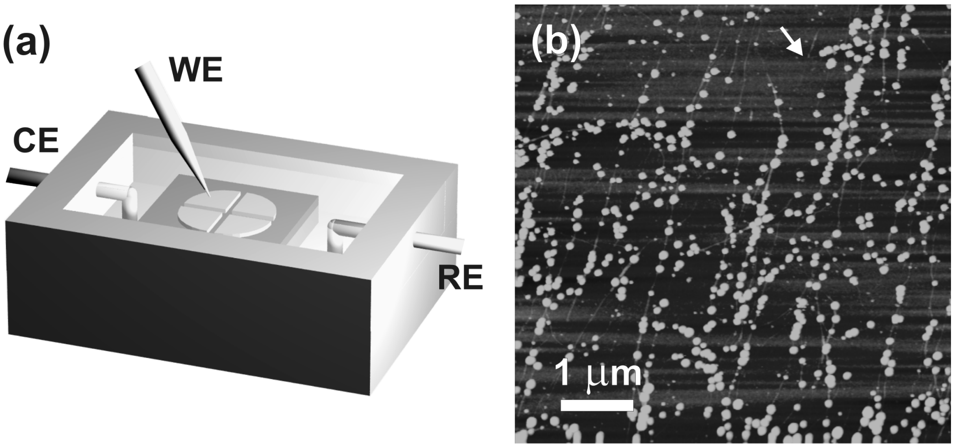

Figure 5.8: (a) Schematic depiction of an electrochemical cell: Teflon cell equipped with counter- (CE) and reference-electrode (RE). Contact to the electrode line on the substrate, used as working electrode (WE), was made with a needle. (b) AFM image of an electrochemically modified carbon nanotube network.

supplied with gold electrodes, giving rise to a more homogeneous coverage with Au-particles. The height of the coating has been estimated to be 5–15 nm.

The modified networks have been tested as gas sensors for both V_2O_5-nanofibers and carbon nanotubes. In the detection of 100 ppm ammonia, responses spanning from -16 % to +10 % were observed for different devices. For carbon nanotubes, values between 0.9 % and 20 % were obtained. The wide variation of responses have been attributed to the different morphologies, making this modification not to be useful for technical applications.

To achieve a better control over the degree of modification, metal electrodeposition onto nanotubes has been carried out. Electrochemistry is a valuable tool to precisely control the extend of chemical modification of the contacted nanotubes through the potential applied in solution [173–176]. By varying the duration of the applied potential and the concentration of the reactive species, the thickness and size of the deposited clusters can be controlled.

To this end, nanotubes have been deposited on a Si/SiO_2 wafer and covered with four electrodes, as described previously (chapter 2.2.2). The same electrodes that are used for electrical transport measurements, have been utilized as working-electrode in a home-built electrochemical cell (Figure 5.8(a)). Contact between nanotubes/electrodes and the potentiostat (Solartron 1285) is achieved via a probe needle. Platinum wires are used as counter and pseudo-reference electrodes. The electrolyte consisted of a 1mM Na_2PdCl_4 (Aldrich) solution in ethanol with 0.1M $LiClO_4$ (Aldrich) as background

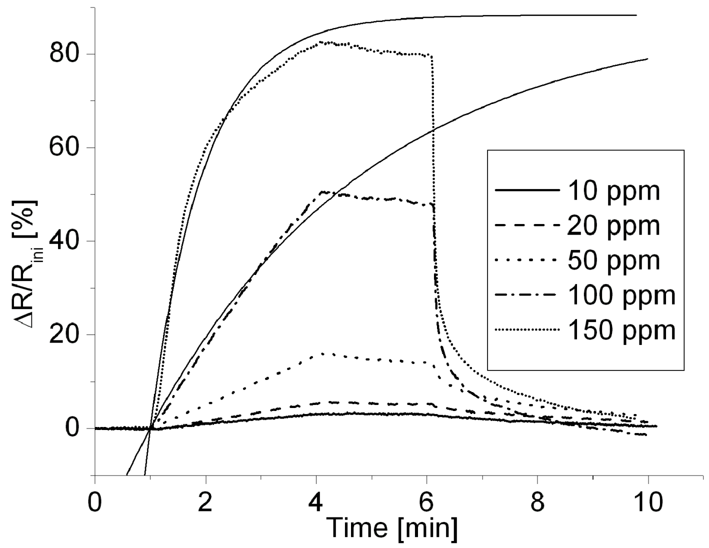

Figure 5.9: Response of a carbon nanotube network, modified by electrodeposition of palladium. The hydrogen concentrations for the various traces are shown in the legend. The thin lines correspond to fitting curves according to equation (4.5).

electrolyte. Application of -1.1 V for 15 sec on the nanotube network, results in the reduction of the palladium salt. Palladium clusters are formed (Figure 5.8(b)) with a height of 25–35 nm, which are exclusively attached to the nanotubes. In contrast, electrically isolated nanotubes are not modified (see arrow in Figure 5.8(b)).

Gas sensing experiments have been performed on these modified networks using the sampe conditions as for the Pd-modified V_2O_5-nanofibers (chapter 4.3): (i) equilibration with nitrogen (0–1 min), (ii) exposure to hydrogen, diluted in nitrogen (1–4 min), (iii) flushing in nitrogen (4–6 min), and (iv) recovery in dry air (6–10 min). Figure 5.9 shows the sensor response to various concentrations of hydrogen (10–150 ppm). Identical to the observations on Pd-modified V_2O_5-nanofibers (chapter 4.3), no signal recovery could be observed in nitrogen atmosphere. The same observation has previously been made for palladium evaporated on nanotubes [39]. The effect can be attributed to the formation of atomic hydrogen within the palladium clusters, and desorption requires the presence of oxygen to form water.

Based on the modified Langmuir model, presented in chapter 5.1, a detailed evaluation of the sensor responses can be made. Compared to the results of ammonia on unmodified nanotubes, the sensor response of hydrogen on Pd-modified nanotubes shows two important differences: (i) the signal reaches saturation at higher concentrations, (ii) the sensor fully recovers to the initial resistance in dry air.

As no desorption occurs in nitrogen ($k_{des} = 0$), equation (4.3) immediately gives rise to θ_c=1. Fitting the sensor response at high concentration with the time evolution of coverage (equation (4.5), thin line added to Figure 5.9), the maximum change of resistance is obtained to be ΔR_∞=86.3 %. Due to the recovery in dry air, no pre-coverage θ_{n-1} has to be taken into account for subsequent exposures, therefore equation (4.5) is valid for all concentrations.

For low hydrogen concentrations, an almost linear increase of resistance was observed (Figure 5.9(a)). This can be attributed to a small change of resistance, where only the linear term of the exponential function becomes visible. Similar sensor behavior has been found for the detection of ammonia on nanotubes within the UHV-chamber (experiments not included in the thesis), which have shown a linear behavior for low pressures and the typical exponential behavior at higher pressures. Based on this interpretation, the saturation value of the exponential fitting function has been fixed to the value of the high concentration (86.3 %, as determined above). With this confinement, the sensor-responses can be fitted for the lower hydrogen concentrations and are exemplified at a concentration of 100 ppm. Deviations from experiment and theory can be attributed to the different sizes of the palladium particles attached to the nanotubes.

Chapter 6

Conclusion

V_2O_5-nanofibers decorated with silver nanoparticles have been obtained by including silver ions in the synthesis route, which furthermore increased the fiber growth rate by a factor of ten. Silver is also incorporated into the fibers, as revealed by EDX analysis. Despite the presence of V^{4+}-sites, the transport properties are not significantly affected (chapter 3.1).

The hydrothermal approach yielded VO_x-nanobelts, which appear in the shape of boomerangs. By varying the synthesis temperature, the length and width of the nanobelts can be tailored. Despite the different morphology of V_2O_5-nanofibers and VO_x-nanobelts, XRD and SAED analysis revealed the close relation of the two materials. The extraordinary morphology of the nanobelts was found to originate from twinning along the [130]-direction (chapter 3.2). Although twinning is well-documented in bulk crystals, it has been observed for the first time in nanoscale objects.

Five types of sensors composed of networks of V_2O_5-nanofibers or carbon nanotubes have been studied (see Table 6.1). Due to their high surface/volume-ratio, these materials showed a sensitive response to ammonia, butylamine, and hydrogen at room temperature. In a first approach, the networks were modified by metal evaporation on top. A more selective modification of the nanotubes has been established via electrochemistry. Both kinds of modification gave rise to an enhanced sensitivity and selectivity of the devices.

A first evaluation of the sensor performances can be made based upon the general requirements on gas sensors, which have been summarized in the introduction: sensitivity, selectivity, stability, and speed. While a good sensitivity has been achieved for most sensors, this achievement alone might not be sufficient for technological applications. The performance of the five types of sensors is summarized in Table 6.1. Although the sensors have not been fully tested yet, each requirement has been assigned a "grade" ranging from promising (+ +), to reasonable (◯) and poor (– –).

Based on the outstanding gas-sensing properties of V_2O_5-nanofibers, a world-patent [134] has been filed in cooperation with Sony International (Europe) GmbH. Future activities within their labs will aim to further improve the long-term stability and reproducibility of this type of sensors.

The interaction of ammonia with metal-oxides has been discussed in great detail in the literature (e.g. [36, 43, 177, 178]), however, the corresponding sensors have normally been operated at elevated temperature. For a thin V_2O_5-film, Wöllenstein and co-workers [179] reported resistance changes on the order of -55 % upon exposure to 100 ppm ammonia at 330°C and 50 % relative humidity. By comparison, values of only -1 % were obtained for the unmodified V_2O_5-nanofibers detecting ammonia (chapter 4.1). This difference is due to the fact that the experiments of this thesis have been performed at room temperature.

The decrease in resistance is a result of n-type doping of the fibers with ammonia. Modification with gold gave rise to an increased response (-8 %), which is attributed to a stronger interaction of ammonia with gold, as compared to V_2O_5. This conclusion has been fostered by an analysis of the time evolution of the sensor signal. Although a fast response (∼1 min) and recovery (∼3 min) could be observed for the V_2O_5-nanofibers, their weak responses are still limiting their sensor application.

To date, only few sensors have been reported which are capable to detect butylamine. The sensing mechanism is in most cases based on changes in a mechanical property of the sensing material, like for example in quartz balance and surface acoustic waves devices. Sotzing and coworkers [180] presented a butylamine sensor based on a polyaniline/carbon black composite. At room temperature, this sensor showed a response of 220,000 % to

Table 6.1: Comparison of the five type of sensors introduced in this thesis with respect to their technical performance. BA denotes butylamine, and Pd-EC the electrochemical modification with palladium. “Grades” are given ranging from (+ +) to (– –). Untested parameters are indicated as (?).

sensor	gas	sensitivity	selectivity	stability	speed
V_2O_5+1nm Au	NH_3	–	◯	?	+ +
V_2O_5	BA	+ +	+ +	+	–
V_2O_5+Pd	H_2	+ +	+ +	+ +	◯
CNT	NH_3	+	◯	– –	+
CNT+Pd-EC	H_2	+	+ +	?	+

58 ppm butylamine. For the unmodified V_2O_5-sensor, values of 500 % were obtained at 9.5 ppm butylamine (chapter 4.2). No information is available for the carbon black sensor on the capability to detect lower concentrations of butylamine, which is the major advantage of the V_2O_5-sensor, as concentrations as low as 30 ppb can be detected.

The interaction mechanism between butylamine and V_2O_5-nanofibers (chapter 4.2) could be elucidated by varying the device geometry. The weak decrease of resistance for the individual fibers has been attributed to charge transfer, similar to the detection of ammonia by V_2O_5-fibers. However, the strongest contribution to the sensor response results from intercalation of the analyte between the gold electrodes and the nanofibers, giving rise to an increased contact resistance. As intercalation is generally much slower compared to surface adsorption, no saturation behavior could be obtained within exposure times on the scale of minutes.

Shimoda et al. [125] observed changes in resistance between 1,000–10,000 % for Pd-modified V_2O_5-crystals upon dosing of hydrogen. Pd-modified V_2O_5-nanofibers have been investigated towards their hydrogen detection capability (chapter 4.3). Reversible responses of 160,000 % have been measured upon exposure to 400 ppm hydrogen. Furthermore, it could be shown that this sensor can be operated in dry air (1,800 % at 2,500 ppm).

The sensing mechanism underlying the tremendous responses observed for the Pd-modified V_2O_5-nanofibers (chapter 4.3) has been evaluated with a combined study, involving direct exposure to atomic hydrogen and temperature dependent electrical transport measurements in an UHV-chamber, as well as Raman spectroscopy under various gas atmospheres. It has been concluded that atomic hydrogen generated inside the palladium desorbs oxygen from the V_2O_5-lattice in accordance to the Mars-van Krevelen mechanism. As a consequence of the introduced oxygen deficiencies, the valency of the vanadium atoms is lowered to V^{4+}, which is accompanied by the formation of bipolarons. The relative high activation energy for hopping makes the bipolarons less mobile as polarons, giving rise to a significantly reduced conductivity. In bulk V_2O_5 [125], bipolarons have been observed as well, however, the chemical reduction of the V^{5+} centers was attributed to an intercalation of atomic hydrogen into the lattice.

The detection of ammonia was one of the first reported sensor applications of carbon nanotubes [47]. For an individual semiconducting nanotube, responses of 1,700 % were reported upon exposure to 1 % (10,000 ppm) of ammonia. For a network sample, the change of resistance was found to be 42 % at the same concentration. This value is in good agreement to 25 % obtained for the unmodified carbon nanotube sensor (chapter 5.1), for which a concentration of only 100 ppm was required. The exposure times for the nanotube network used in Reference [47] and in this study are similar (200 sec). However, it is remarkable that in the literature, recovery of such sensors has been reported only under photoirradiation [33].

Only partial desorption of ammonia has been observed after the test gas was switched off. An adapted Langmuir theory, which accounts for both reversible and irreversible adsorption, has proven capable to describe the sensor response. Thermal desorption spectroscopy has been used to understand the origin of the irreversible component. The spectra revealed a broad desorption feature, which was attributed to the presence of (polar) defects on the nanotubes, to which the polar ammonia molecules bind irreversibly.

H. Dai and co-workers presented the hydrogen detection with the aid of carbon nanotubes, modified by evaporation of palladium [39]. For an individual nanotube, responses of 140 % are reported for the exposure to 400 ppm hydrogen in argon. For network samples a value of 38 % was obtained upon exposure to the same concentration in air. These values are in good agreement with 85 % obtained for exposures to 150 ppm hydrogen in nitrogen with network samples, which were Pd-modified via electrodeposition (chapter 5.2). However, as either the reference gas or the sample geometry differs, a direct comparison is difficult. The exposure and recovery times obtained in the present study (60 sec and 300 sec, respectively) are identical to the literature values.

Electrochemical modification offers the intriguing possibility of a controlled decoration of carbon nanotubes with palladium clusters. While evaporation of the noble metal modifies the entire surface, the electrochemical approach allows for selective modification of the nanotubes, leaving the substrate and isolated nanotubes unaltered.

For all five types of sensor a fundamental understanding of the sensor mechanisms involved in the detection of gases with 1D-materials could be gained. Table 6.2 summarizes the interactions between the gases and the two types of nanowires, which are

Table 6.2: Comparison of the five types of sensor studied in this thesis with respect to their sensing mechanism. BA indicates butylamine, while Pd-EC denotes the electrochemical modification with palladium.

sensor	gas	electrical effects	gas-nanowire interactions
V_2O_5+1nm Au	NH_3	charge transfer	adsorption on Au-cluster
V_2O_5	BA	contact resistance	diffusion in fiber-electrode interface
V_2O_5+Pd	H_2	bipolaron formation	atomic hydrogen desorbs lattice-oxygen
CNT	NH_3	charge transfer	partially irreversible adsorption
CNT+Pd-EC	H_2	charge transfer	atomic hydrogen stored in palladium

most relevant to the respective operation mechanism of each sensor. The knowledge of these interactions and the associated electrical effects will be important for future experiments aiming at further improvements of sensors based on nanowires.

Appendix A

Alternative sensor modifications

Besides the three types of V_2O_5-nanofiber sensors (chapter 4) and the two forms of sensors based on carbon nanotubes (chapter 5) many other modifications have been investigated. The Tables of this appendix give an overview on these material combinations and their respective responses. They are sorted by sensor material and divided by modifications via evaporation and via chemical modifications.

Table A.1: Responses of V_2O_5-nanofibers modified via evaporation of metal on top. The values indicate the response to 100 ppm of the indicated gas.

metal	thickness	NH_3	CO	H_2
unmodified	–	-5 … -2.4	-0.6	-0.3
Ag	1–2 nm	-8 … 7	-0.8 … 0.15	0
Au	1 nm	-8.5	-1 … -2	-0.7
Pt	1 nm	2	-2	-1
Pd	1 nm	–	–	50 … 120

Table A.2: Responses of V_2O_5-nanofibers modified via wet chemical means. The values indicate the response to 100 ppm of the indicated gas. NMF=N-methylformamide

salt	solvent	concentration	NH_3	CO	H_2
$Ag^+(CH_3COO)^-$	H_2O	1mg/mℓ	8 … 24	1 … 2.8	0
$Au^+S(CH_3)_2Cl^-$	NMF	1mg/mℓ	-16 … 10	-6 … 2	-2 … -0.5
$(Pt(NH_3)_4)^{2+}(Cl^-)_2$	H_2O	1mg/mℓ	-1	-0.5	0
$Pd^{2+}(CH_3OO^-)_2$	toluene	1mg/mℓ	-1	-0.4	0

Table A.3: Responses of carbon nanotubes modified via evaporation of metal on top. The values indicate the response to 100 ppm of the indicated gas.

metal	thickness	NH_3	H_2
unmodified	–	$7 \dots 65$	0
Pd	1 nm	$35 \dots 180$	$90 \dots 330$
Au	0.5 nm	$12 \dots 60$	$13 \dots 170$

Table A.4: Responses of carbon nanotubes modified via wet chemical means. The values indicate the response to 100 ppm of the indicated gas. Pd-EC denotes the electrochemical modification, as described in chapter 5.2.

salt	solvent	concentration	NH_3	H_2
$Ag^+(CH_3COO)^-$	NMF	$1 mg/m\ell$	1.8	0.4
$Au^+S(CH_3)_2Cl^-$	H_2O	$1 mg/m\ell$	$0.9 \dots 20$	–
Pd-EC	–	–	$19 \dots 22$	$50 \dots 110$

Bibliography

[1] W. Göpel, J. Hesse, and J. Zemel, *Sensors: A Comprehensive Survey* (VCH, New York, 1995).

[2] *Solid-State Gas Sensors*, edited by P. Moseley and B. Tofield (Hilger, Bristol, 1987).

[3] *Gas Sensors: Principles, Operation and Developments*, edited by G. Sberveglieri (Kluver, Boston, 1992).

[4] A. Mandelis and C. Christofides, *Physics, Chemistry and Technology of Solid State Gas Sensor Devices* (John Wiley & Sons, Inc, New York, 1993).

[5] T. Seiyama, *Chemical Sensor Technology, Vol. 1* (Elsevier Scientific Publisher, Amsterdam, 1988).

[6] W. Göpel, Sens. & Actuat. B **4**, 7 (1991).

[7] W. Göpel, Sen. & Actuat. A **56**, 83 (1996).

[8] C. Hagleitner *et al.*, Nature **414**, 293 (2001).

[9] S. Semancik *et al.*, Sens. & Actuat. B **77**, 579 (2002).

[10] W. Göpel, Microelect. Eng. **32**, 75 (1996).

[11] K. Albert *et al.*, Chem. Rev. **100**, 2595 (2000).

[12] *Handbook of Machine Olfaction: Electronic Nose Technology*, edited by T. Pearce, S. Schiffman, H. Nagle, and J. Gardner (Wiley-VCH, Weinheim, 2003).

[13] M. Fleischer and H. Meixner, J. Vac. Sci. Technol. **A 17**, 1866 (1999).

[14] M. Daughtery *et al.*, Preprints of Symposia - ACS, Division of Fuel Chemistry **44**, 937 (1999).

[15] B. Hoffheins, R. Lauf, and J. Felten, Intl. J. Microcircuits and Electronic Packaging **18**, 297 (1995).

[16] S. Basu and A. Dutta, Mater. Chem. Phys. **47**, 93 (1997).

[17] L. Birkefeld, A. Azad, and S. Akbar, J. Am. Ceram. Soc. **75**, 2964 (1992).

[18] C. Imawan, H. Steffes, F. Solzbacher, and E. Obermeier, Sens. & Actuat. B **77**, 346 (2001).

[19] V. Chaudhary, I. Mulla, and K. Vijayamohanan, Sens. & Actuat. B **55**, 154 (1999).

[20] K. Schierbaum, U. Kirner, J. Geiger, and W. Göpel, Sens. & Actuat. B **4**, 87 (1991).

[21] I. Lundström, A. Spetz, U. Ackelid, and H. Sundgren, Sens. & Actuat. B **1**, 15 (1990).

[22] I. Lundström, M. Armgarth, and L.-G. Petersson, CRC Critical Reviews in Solid State and Materials Sciences **15**, 201 (1989).

[23] L.-G. Ekedahl, M. eriksson, and I. Lundström, Acc. Chem. Res. **31**, 249 (1998).

[24] J. McMonagle, V. Casey, and B.O'Beirn, Analyst **118**, 389 (1993).

[25] H. Sundgren, I. Lundström, and F. Winquist, Sens. & Actuat. B **B 2**, 115 (1990).

[26] D. Baselt *et al.*, Sens. & Actuat. B **88**, 120 (2003).

[27] M. Butler, J. Electrochem. Soc. **138**, L46 (1991).

[28] P. Liu *et al.*, J. Electrochem. Soc. **149**, H76 (2002).

[29] P. Liu *et al.*, World-Patent WO 01/86266 A2 (2001).

[30] C. Christofides and A. Mandelis, J. Appl. Phys. **68**, R1 (1990).

[31] S. Santucci *et al.*, J. Chem. Phys. **119**, 10904 (2003).

[32] L. Valentini *et al.*, Appl. Phys. Lett. **82**, 961 (2003).

[33] R. Chen *et al.*, Appl. Phys. Lett. **79**, 2258 (2001).

[34] M. Penza, C. Martucci, and G. Cassano, Sens. & Actuat. B **50**, 52 (1998).

[35] S. Capone, R. Rella, P. Siciliano, and L. Vasanelli, Thin Solid Films **350**, 264l (1999).

[36] J. Wöllenstein *et al.*, Sens. & Actuat. B **93**, 350 (2003).

[37] M. Law *et al.*, Angew. Chem. **114**, 2511 (2002).

[38] O. Varghese *et al.*, Sens. & Actuat. B **93**, 338 (2003).

[39] J. Kong, M. Chapline, and H. Dai, Adv. Mater. **13**, 1384 (2001).

[40] F. Favier *et al.*, Science **293**, 2227 (2001).

[41] E. Walter, F. Favier, and R. Penner, Anal. Chem. **74**, 1546 (2002).

[42] B. Murray, E. Walter, and R. Penner, Nanoletters **4**, 665 (2004).

[43] D. Zhang *et al.*, Appl. Phys. Lett. **83**, 1845 (2003).

[44] C. Li *et al.*, Appl. Phys. Lett. **82**, 1613 (2003).

[45] E. Comini *et al.*, Appl. Phys. Lett. **81**, 1869 (2002).

[46] Y. Cui, Q. Wei, H. Park, and C. Lieber, Science **293**, 1289 (2001).

[47] J. Kong *et al.*, Science **287**, 622 (2000).

[48] P. Collins, K. Bradley, M. Ishigami, and A. Zettl, Science **287**, 1801 (2000).

[49] P. Qi *et al.*, Nano Lett. **3**, 347 (2003).

[50] S. Chopra *et al.*, Appl. Phys. Lett. **80**, 4632 (2002).

[51] O. Varghese *et al.*, Sens. & Actuat. B **81**, 32 (2001).

[52] C. Adu *et al.*, Chem. Phys. Lett. **337**, 31 (2001).

[53] A. Modi *et al.*, Nature **424**, 171 (2003).

[54] S. Heinze *et al.*, Phys. Rev. Lett. **89**, 106801 (2002).

[55] J. Kong and H. Dai, J. Phys. Chem. B **105**, 2890 (2001).

[56] J. Li *et al.*, Nano Letters **3**, 597 (2003).

[57] Y. Joseph, B. Guse, A. Yasuda, and T. Vossmeyer, Sens. & Actuat. B **98**, 188 (2004).

[58] H. Wohltjen and A. Snow, Anal. Chem. **70**, 2856 (1998).

[59] I. Raible *et al.*, *in preparation*, (2004).

[60] C. Snachez, R. Morineau, and J. Livage, Phys. Stat. Sol. (a) **76**, 661 (1983).

[61] C. Guestaux, J. Leaute, C. Virey, and J. Vial, U.S. Patent 3/658573 (1972).

[62] M. Lira-Cantu and P. Gomez-Romero, J. Electrochem. Soc. **146**, 2029 (1999).

[63] A. Thess *et al.*, Science **273**, 483 (1996).

[64] A. Rinzler *et al.*, Appl. Phys. A **75**, 449 (1998).

[65] J. Livage, Chem. Mater. **3**, 578 (1991).

[66] J. Livage, Coord. Chem. Rev. **178-180**, 999 (1998).

[67] G. Kim *et al.*, Appl. Phys. Lett. **76**, 1875 (2000).

[68] A. Silva, R. Hudgins, and P. Silveston, Can. J. Chem. Eng. **57**, 176 (1979).

[69] K. Mori, A. Miyamoto, T. Ui, and Y. Murakami, J. Chem. Soc. Chem. Comm. **4**, 260 (1982).

[70] G. Mul, I. Wachs, and A. Hirschon, Cat. Today **78**, 327 (2003).

[71] A. Miyamoto *et al.*, J. Catal. **74**, 144 (1982).

[72] B. Weckhuysen and D. Keller, Cat. Today **78**, 25 (2003).

[73] J. Muster *et al.*, Adv. Mater. **12**, 420 (2000).

[74] M. Dresselhaus, G. Dresselhaus, and P. Eklund, *Science of Fullerenes and Carbon Nanotubes : Their Properties and Applications* (Academic Press, London, 1996).

[75] *Carbon Nanotubes*, edited by M. Endo, S. Iijima, and M. Dresselhaus (Elsevier Science, Amsterdam, 1996).

[76] *Physical Properties of Carbon Nanotubes*, edited by R. Saito, M. Dresselhaus, and G. Dresselhaus (Imperial College Press, London, 1998).

[77] *Science and application of nanotubes*, edited by D. Tomanek and R. Enbody (Kluver Academic, Dordrecht, 2000).

[78] *Carbon Nanotubes: Synthesis, Structure, Properties and Applications*, edited by M. Dresselhaus, G. Dresselhaus, and P. Avouris (Springer-Verlag, Berlin, 2001).

[79] *Procedures in Scanning Probe Microscopy*, edited by R. Colton *et al.* (John Wiley & Sonc, Inc, New York, 1998).

[80] R. Allmann, *Röntgenpulverdiffraktometrie* (Springer-Verlag, Berlin, 2003).

[81] D. Williams, *Transmission electron microscopy: a textbook for materials science* (Plenum Press, New York, 1996).

[82] M. Otten, J. Electr. Microscopy Technique **17**, 221 (1991).

[83] M. Tobin, *Laser Raman Spectroscopy* (John Wiley & Sons, Inc, New York, 1971).

[84] K. Christmann, *Introduction to Surface Physical Chemistry* (Dr. D. Steinkopff Verlag GmbH & Co. KG, Darmstadt, 1991).

[85] H. Ulbricht, Ph.D. thesis, Freie Universität Berlin, 2003.

[86] H. Ulbricht, J. Kriebel, G. Moos, and T. Hertel, Chem. Phys. Lett. **363**, 252 (2002).

[87] J. Livage, Coord. Chem. Rev. **190-192**, 391 (1999).

[88] O. Kern, Master's thesis, Ecole Polytechnique Federale de Lausanne, 1995.

[89] T. Yao, Y. Oka, and N. Yamamoto, J. Mater. Chem. **2**, 337 (1992).

[90] V. Petkov *et al.*, J. Am. Chem. Soc. **124**, 10157 (2002).

[91] P. Davidson *et al.*, Prog. Polym. Sci. **22**, 913 (1997).

[92] T. Yao, Y. Oka, and N. Yamamoto, Mat. Res. Bull **27**, 669 (1992).

[93] Y. Xia *et al.*, Adv. Mater. **15**, 353 (2003).

[94] R. Andrews *et al.*, Chem. Phys. Lett. **303**, 467 (1999).

[95] X. Duan and C. Lieber, Adv. Mater. **12**, 298 (2000).

[96] D. Pan, Z. Shuyuan, Y. Chen, and J. Hou, J. Mater. Res. **17**, 1981 (2002).

[97] X. Li, J. Liu, and Y. Li, Appl. Phys. Lett. **81**, 4832 (2002).

[98] K. Tang, Y. Qian, J. Zeng, and X. Yang, Adv. Mater. **15**, 448 (2003).

[99] Y. Gao, H. Niu, C. Zeng, and Q. Chen, Chem. Phys. Lett. **367**, 141 (2003).

[100] D. Zhua, H. Zhua, and Y. Zhanga, J. Cryst. Growth **249**, 172 (2003).

[101] M. Spahr *et al.*, Ang. Chem. Int. Ed. **37**, 1263 (1998).

[102] U. Schlecht *et al.*, Appl. Phys. A **78**, 527 (2004).

[103] Y. Ningyi, L. Jinhua, and L. Chenglu, Adv. Surf. Sci. **191**, 176 (2002).

[104] P. Ramdohr and H. Strunz, *Klockmann's Lehrbuch der Mineralogie* (Ferdinand Enke Verlag, Stuttgart, 1967).

[105] *International Tables for Crystallography*, edited by A. Wilson and E. Prince (Kluwer Academic Publishers, Dordrecht, 1999).

[106] K. Kirschbaum, A. Martin, D. Parrish, and A. Pinkerton, J. Phys.: Condens. Mater. **11**, 4483 (1999).

[107] B. Hyde and R. Tilley, Phys. Stat. Sol. (a) **2**, 749 (1970).

[108] R. Baddour-Hadjean *et al.*, J. Raman Spectrosc. **33**, 631 (2002).

[109] L. Abello, E. Husson, Y. Repelin, and G. Lucazeau, J. Sol. Stat. Chem. **56**, 379 (1985).

[110] Y. Repelin, E. Husson, L. Abello, and G. Lucazeau, Spectrochimica Acta **41A**, 993 (1985).

[111] S.-H. Lee *et al.*, J. Appl. Phys. **92**, 1893 (2002).

[112] C. Snachez, J. Livage, and G. Lucazeau, J. Raman Spectr. **12**, 68 (1982).

[113] S.-H. Lee *et al.*, Sol. Stat. Ionics **165**, 111 (2003).

[114] S. Xie, E. Iglesia, and A. Bell, Langmuir **16**, 7162 (2000).

[115] M. Banares and I. Wachs, J. Raman Spectr. **33**, 359 (2002).

[116] Z. Popovic *et al.*, Phys. Rev. B **61**, 11454 (2000).

[117] E. Cazzanelli, g. Mariotto, S. Passerini, and W. Smyrl, Non-Cryst. Solids **208**, 89 (1996).

[118] C. Gomez-Navarro *et al.*, Nanotechnology **13**, 1 (2002).

[119] P. Kounavis *et al.*, J. Phys. C: Solid State Phys. **21**, 967 (1988).

[120] G. Kim, Ph.D. thesis, Seoul National University, 1999.

[121] H. Böttger and V. Bryksin, *Hopping Conduction in Solids* (VCH, Weinheim, 1985).

[122] N. Mott, J. Non-Cryst. Solids **1**, 1 (1968).

[123] J. Bullot, O. Gallais, M. Gauthier, and J. Livage, Appl. Phys. Lett. **36**, 986 (1980).

[124] J. Haemers, E. Baetens, and J. Vennik, Phys. Stat. Sol. (a) **20**, 381 (1973).

[125] M. Shimoda, A. Yoshikawa, and K. Yagisawa, J. Mater. Sci. **29**, 478 (1994).

[126] U. Schlecht *et al.*, Molecular Nanostructures: XVII International Winterschool/Euroconference on Electronic Properties of Novel Materials **AIP 685**, 491 (2003).

[127] I. Langmuir, J. Am. Chem. Soc. **30**, 1361 (1918).

[128] P. Atkins, *Physical Chemistry* (Oxford University Press, Oxford, 1999).

[129] V. Venugopal, Biosens. bioelectron. **17**, 147 (2002).

[130] E. Ohashi *et al.*, J. Food Sci. **56**, 1275 (1991).

[131] G. Preti *et al.*, J. Chromatogr. **432**, 1 (1988).

[132] A. Robinson and L. Pauling, Clin. Chem **20**, 961 (1974).

[133] D. Laing, H. Panhuber, and R. Baxter, Chem. Senses and Flavour **3**, 149 (1978).

[134] I. Besnard *et al.*, World-Patent WO-03/046536 (2003).

[135] M. Gomes, M. Verissimo, and J. Oliveira, Sens. & Actuat. B **57**, 261 (1999).

[136] A. Bouhaouss and P. Aldebert, Mater. Res. Bull. **18**, 1247 (1983).

[137] P. Gomez-Romero, Adv. Mater. **13**, 163 (2001).

[138] L. Kiss, K. Bali, T. Szorenyi, and I. Hevesi, Solid State Commun. **58**, 609 (1986).

[139] F. Lewis, *The Palladium-Hydrogen System* (Academic Press, London, 1967).

[140] P. Anderson, Phys. Rev. Lett. **34**, 953 (1975).

[141] A. Alexandrov and J. Ranninger, Phys. Rev. B **23**, 1796 (1981).

[142] A. Alexandrov and N. Mott, *Polarons & Bipolarons* (World Scientific, Singapore, 1995).

[143] M. Onoda, T. Takahashi, and H. Nagasawa, J. Phys. Soc. Japan **51**, 3868 (1982).

[144] R. Wallis, N. Sol, and A.Zylbersztejn, Sol. Stat. Comm. **23**, 539 (1977).

[145] M. Onoda and H. Nagasawa, Phys. Stat. Sol. (b) **141**, 507 (1987).

[146] H. Nagasawa and M. Onoda, Syn. Metals **19**, 971 (1987).

[147] M. Reghu, S. Subramanyam, and S.Chatterjee, Phys. Rev. B **43**, 4236 (1991).

[148] V. Bryksin and V. Voloshin, Sov. Phys. Solid State **26**, 1429 (1984).

[149] V. Bryksin and A. Gol'tsev, Sov. Phys. Solid State **30**, 851 (1988).

[150] A. Yoshikawa, K. Yagisawa, and M. Shimoda, J. Mater. Sci. **29**, 1319 (1994).

[151] P. Dickens, A. Chippindale, S. Hibble, and P. Lancaster, Mat. Res. Bull. **19**, 319 (1984).

[152] S. Ayyappan and C. Rao, Mat. Res. Bull. **30**, 947 (1995).

[153] P. Mars and D. van Krevelen, Chem. Eng. Sci. **3**, 41 (1954).

[154] V. Belousov *et al.*, Chem. Eng. J. **91**, 143 (2003).

[155] A. D. Costa *et al.*, Surf. Sci. **370**, 339 (1997).

[156] X. Yin *et al.*, J. Phys. Chem. B **103**, 1263 (1999).

[157] B. Tepper *et al.*, Surf. Sci. **496**, 64 (2002).

[158] K. Hermann, M. Witko, and R. Druzinic, Faraday Discuss. **114**, 53 (1999).

[159] S. Surnev, M. Ramsey, and F. Netzer, Prog. Surf. Sci. **73**, 117 (2003).

[160] K. Bradley *et al.*, Phys. Rev. Lett. **91**, 218301 (2003).

[161] V. Derycke, R. Martel, J. Appenzeller, and P. Avouris, Appl. Phys. Lett. **80**, 2773 (2002).

[162] H. Chang, J. Lee, S. Lee, and Y. Lee, Appl. Phys. Lett. **79**, 3863 (2001).

[163] J. Zhao, A. Buldum, J. Han, and J. Lu, Nanotechnology **13**, 195 (2002).

[164] A. Kuznetsova *et al.*, J. Chem. Phys. **115**, 6691 (2001).

[165] Y. Fan, M. Burghard, and K. Kern, Adv. Mater. **14**, 130 (2002).

[166] A. Kuznetsova *et al.*, Chem. Phys. Lett. **321**, 292 (2000).

[167] P. Rowntree, G. Scoles, and J. Xu, J. Chem. Phys. **92**, 3853 (1990).

[168] G. Bomchil *et al.*, J. Chem. Soc. Faraday Trans. 1 **75**, 1535 (1979).

[169] D. Chakarov, L. Sterlund, and B. Kasemo, Vacuum **46**, 1109 (1995).

[170] P. Redhead, Vacuum **12**, 203 (1962).

[171] R. Zacharia, H. Ulbricht, and T. Hertel, Phys. Rev. B **69**, 155406 (2004).

[172] H. Ulbricht, G. Moos, and T. Hertel, Phys. Rev. B **66**, 075404 (2002).

[173] J. Bahr *et al.*, J. Am. Chem. Soc. **123**, 6536 (2001).

[174] S. Kooi, U. Schlecht, M. Burghard, and K. Kern, Ang. Chem. Intl. Ed. **41**, 1353 (2002).

[175] K. Balasubramanian *et al.*, Adv. Mater. **15**, 1515 (2003).

[176] K. Balasubramanian, R. Sordan, M. Burghard, and K. Kern, Nano Lett. **4**, 827 (2004).

[177] G. Chandrappa *et al.*, Catalysis Today **78**, 85 (2003).

[178] I. Jimenez *et al.*, J. Electrochem. Soc. **150**, H72 (2003).

[179] J. Wöllenstein *et al.*, Sens. Mater. **15**, 239 (2003).

[180] G. Sotzing, J. Phend, R. Grubbs, and N. Lewis, Chem. Mater. **12**, 593 (2000).

List of Publications

- I. Raible, M. Burghard, U. Schlecht, A. Yasuda, and T. Vossmeyer:
  V_2O_5 nanofibres: Novel gas sensors with extremely high sensitivity and selectivity to amines
  (accepted)

- U. Schlecht, B. Guse, I. Raible, T. Vossmeyer, and M. Burghard:
  A direct synthetic approach to vanadium pentoxide nanofibres modified with silver nanoparticles
  Chem. Comm. 2004, 2184 (2004)

- U. Schlecht, L. Kienle, V. Duppel, M. Burghard, and K. Kern:
  Boomerang-shaped VO_x nanocrystallites
  Kirchberg Proceeding "Electronic Properties of Synthetic Nanostructures", CP 723, 415, Eds. H. Kuzmany et al. (American Institute of Physics, New York, 2004)

- A.B. Kaiser, B. Chapman, U. Schlecht, and M. Burghard:
  Comparison of Current-Voltage Characteristics of Nanofibres and Nanotubes
  Kirchberg Proceeding "Electronic Properties of Synthetic Nanostructures", CP 723, 99, Eds. H. Kuzmany et al. (American Institute of Physics, New York, 2004)

- U. Schlecht, M. Knez, V. Duppel, L. Kienle, and M. Burghard:
  Boomerang-shaped VO_x belts: Twinning within isolated nanocrystals
  Appl. Phys. A 78, 527 (2004)

- U. Schlecht, I. Besnard, A. Yasuda, T. Vossmeyer, and M. Burghard:
  V_2O_5 nanofiber-based chemiresistors for ammonia detection
  Kirchberg Proceeding "Molecular nanostructures", CP 685, 491, Eds. H. Kuzmany et al. (American Institute of Physics, New York, 2003)

- I. Besnard, T. Vossmeyer, A. Yasuda, M. Burghard, and U. Schlecht:
  The use of 1D semiconductor materials as chemical sensing materials, produced

and operated close to room-temperature
World-Patent, WO-03/046536 (2003)

- J. Maultzsch, S. Reich, U. Schlecht, and C. Thomsen:
  High-Energy Phonon Branches of an Individual Metallic Carbon Nanotube
  Phys. Rev. Lett. 91, 087402 (2003)

- U. Schlecht, U.D. Venkateswaran, E. Richter, J. Chen, R.C. Haddon, P.C. Eklund, and A.M. Rao:
  High-Pressure Raman Study of Debundled Single-Walled Carbon Nanotubes
  J. Nanosci. Nanotech. 3, 139 (2003)

- M. Burghard, S. Kooi, U. Schlecht, K. Balasubramanian, and K. Kern:
  Electrochemical functionalization of individual single-walled carbon nanotubes
  Kirchberg Proceeding “Electronic properties of molecular nanotubes”, CP 633, 77, Eds. H. Kuzmany et al. (American Institute of Physics, New York, 2002)

- C. Jiang, K. Kempa, J. Zhao, U. Schlecht, U. Kolb, T. Basche, M. Burghard, and A. Mews:
  Strong enhancement of the Breit-Wigner-Fano Raman line in carbon nanotube bundles caused by plasmon band formation
  Phys. Rev. B 66, 161404 (2002)

- S.E. Kooi, U. Schlecht, M. Burghard, and K. Kern:
  Electrochemical Modification of Single Carbon Nanotubes
  Angw. Chem. Int. Edit. 41 (8), 1353 (2002)
  Elektrochemische Modifizierung einzelner Kohlenstoff-Nanoröhren
  Angw. Chem. 114 (8), 1409 (2002)

- A.M. Rao, J. Chen, E. Richter, U. Schlecht, P.C. Eklund, R.C. Haddon, U.D. Venkateswaran, Y.-K. Kwon, and D. Tomanek:
  Effect of van der Waals Interactions on the Raman Modes in Single Walled Carbon Nanotubes
  Phys. Rev. Lett. 86, 3895 (2001)

- U.D. Venkateswaran, E.A. Brandsen, U. Schlecht, A.M. Rao, E. Richter, I. Loa, K. Syassen, and P.C. Eklund:
  High Pressure Studies of the Raman-Active Phonons in Carbon Nanotubes
  Phys. Stat. Sol. (b) 223, 225 (2001)

Curriculum vitae

Name:	Ulrich Schlecht
Date of Birth:	January 30, 1976
Nationality	German

1995	Abitur at the Ernst-Barlach-Gesamtschule in Dinslaken, Germany
1995–1996	Military service
1996–1999	Studies of Physics and Mathematics at the Gerhard-Mercator-Universität Duisburg, Germany
1998	Vordiplom (Bachelor) in Physics
1998	Vordiplom (Bachelor) in Mathematics
1999	Fulbright-grant
1999–2000	Graduate studies of Physics at the University of Kentucky, Lexington, KY. Research in the lab of Prof. A.M. Rao.
2000	Masters of Science in Physics. Thesis: ”High-Pressure Raman-Studies of Solubilized Nanotubes”
2000–2004	Research in the group of Prof. K. Kern at the Max-Planck-Institute for Solid State Research, Stuttgart, Germany
2004	PhD thesis: “Gas-Sensing Properties of V_2O_5-Nanofibers and Carbon Nanotubes”

Acknowledgements

Despite the fact that a PhD-thesis has to reflect an independent achievement within the scientific-community, the thesis would not have been realized without the aid of many people. Due to their diverse backgrounds, I learned to address problems from many different points-of-view.

I am thankful to Prof. Klaus Kern, who was not only my boss and PhD-supervisor, but also a mentor. The informal working environment made it possible to discuss any kind of problems without reservation.

Gratitude goes to my advisor Dr. Marko Burghard. Our discussions were always fruitful and his advise allowed me finally work independently, tackling problems on my own.

Thanks to Prof. Benoit Deveaud-Pledran, Prof. László Forro, Prof. Louis Schlapbach, and Prof. Falko Netzer for finding time to participate on the examination.

I acknowledge the support of Sony for the supply of sensor-chips and the possibility to perform all experiments on the dilution unit in their lab. Thanks to the "crew" at Sony: Dr. A. Yasuda, Dr. Tobias Vossmeyer, Dr. Isabelle Raible, and Berit Guse, who gave me an insight on the industrial point-of-view. I appreciate the TEM-work on Ag-V_2O_5 of Berit Guse and the experiments with butylamine performed by Isabelle Raible.

Thanks to the "crystallographic" guys: Dr. Lorenz Kienle and Viola Duppel for the TEM-work on the boomerang-shaped VO_x-nanobelts. Could you imagine, that this work would never have been done, if Dr. Martin Panthöfer had not introduced us?! A conference in Kirchberg was necessary to meet next door neighbors.

At the same conference, I met Prof. Alan Kaiser: I very much liked our theoretical discussions on the transport-properties of V_2O_5.

During this conference I was introduced to the aspects of thermal desorption spectroscopy and I thank Dr. Hendrik Ulbricht and Prof. Tobias Hertel for the joint project combining our techniques to get a deeper insight into gas-nanotube interactions.

Without the help of various service-groups and technicians within the Max-Planck-

Insitute, some of the experiments would not have been realized: The technology group for the evaporation of metals, especially Frank Schartner for bonding the samples. Hans Vogt and Armin Schulz of the spectroscopy group, who showed me how to handle their Raman-spectrometer. Wolfgang Stiepany and Wolfgang Heinz for assistance with the UHV-chamber.

Thanks to the nanotube-group: Steve, Yuwei, Roman, Jingbiao, Tang, Nacho, Tilman, and Alicia for our rare but intense discussions. Special thanks to Kannan Balasubramanian for the electrochemical modification of carbon nanotubes.

Finally, I'm happy to know the "coffee-corner-crew" (Ralf, Alex S., Alex B., Dominik, Gero, Michael, Peter, Lars, Mato, Klaus), as we always have had a lot of fun during our coffee-breaks. In addition, their diverse backgrounds were always a pool of knowledge to me.